

**MANAGEMENT OF FIBER PHYSICAL EFFECTS IN  
HIGH-SPEED OPTICAL COMMUNICATION AND SENSOR  
SYSTEMS**

**YANG JING**

**NATIONAL UNIVERSITY OF SINGAPORE**

**2011**

**MANAGEMENT OF FIBER PHYSICAL EFFECTS IN  
HIGH-SPEED OPTICAL COMMUNICATION AND SENSOR  
SYSTEMS**

**YANG JING**

*(B. Eng., Xi'an Jiaotong University, China)*

A THESIS SUBMITTED  
FOR THE DEGREE OF DOCTOR OF PHILOSOPHY  
DEPARTMENT OF ELECTRICAL AND COMPUTER ENGINEERING  
NATIONAL UNIVERSITY OF SINGAPORE

2011

# Acknowledgement

I am heartily thankful to my supervisor, Dr. Changyuan Yu, who has supported me throughout my thesis with his profound knowledge and patience. He provided excellent research environment and valuable advises for me. Without his effort this thesis would not have been completed. I also want to thank my thesis committee for their time and dedication.

I am grateful to the research scientists in Institute for Infocom Research (I2R) for helping me start in the lab and giving me valuable advises and constant encouragement during my postgraduate years. I would like to thank Prof. Chao Lu and other researchers in Photonics Research Centre, the Hong Kong Polytechnic University for their supports and kindly helps during my visit in winter 2009. I would also like to thank my office mates and friends. I benefit from the discussions with them on research as well as life.

Finally, I thank my parents for their constant support throughout my life and study. I am also grateful to my husband for his endless patience and encouragement.

# Contents

<b>Acknowledgement</b>	<b>ii</b>
<b>Contents</b>	<b>iii</b>
<b>Summary</b>	<b>vii</b>
<b>List of Figures</b>	<b>ix</b>
<b>List of Tables</b>	<b>xvi</b>
<b>List of Abbreviations</b>	<b>xvii</b>
<b>1 Introduction</b>	<b>1</b>
1.1 The Physical Effects in Optical Fibers . . . . .	2
1.2 High-Speed Optical Transmission Systems . . . . .	8
1.2.1 Limitations of Fiber Physical Effects . . . . .	8
1.2.2 Applications of Fiber Physical Effects . . . . .	12
1.3 Optical Sensor Systems . . . . .	14
1.3.1 Optical Sensor Based on Fiber Bragg Grating . . . . .	15
1.3.2 Distributed Fiber Sensor Based on Brillouin Optical Time Do- main Analysis . . . . .	16

## CONTENTS

---

1.3.3	Distributed Fiber Sensor Based on Brillouin Optical Coherent Domain Analysis . . . . .	18
1.4	Focus and Structure of the Thesis . . . . .	19
<b>2</b>	<b>Multi-Channel Optical Pulse Train Generation Based on Parametric Process in Highly-Nonlinear Fiber</b>	<b>21</b>
2.1	Principle of Multi-Channel Optical Pulse Train Generation Through Parametric Process . . . . .	22
2.2	Experimental Results . . . . .	24
2.2.1	Performance of the Optical Parametric Amplification . . . . .	24
2.2.2	6-Channel 80 GHz Optical Pulse Generation . . . . .	30
2.3	Simulation Results of BER Performance . . . . .	34
2.4	Conclusions . . . . .	40
<b>3</b>	<b>Broadband Multi-Wavelength Light Source Generation Using a Single Phase Modulator in a Loop</b>	<b>42</b>
3.1	Principle of Multi-Wavelength Light Source Generation Using a Single Phase Modulator in a Loop . . . . .	43
3.2	Simulation Results . . . . .	46
3.2.1	Single PM in a Loop Structure without EDFA . . . . .	46
3.2.2	Single PM in an Amplified Loop . . . . .	47
3.3	Experimental Results . . . . .	47
3.3.1	Single PM in a Loop Structure without EDFA . . . . .	48
3.3.2	Single PM in an Amplified Loop . . . . .	49
3.4	Conclusions . . . . .	52
<b>4</b>	<b>CD-Insensitive PMD Monitoring Based on RF Power Measurement</b>	<b>53</b>
4.1	Principle of PMD Monitoring Based on RF Power Measurement . . .	55

## CONTENTS

---

4.2	Simulation Results . . . . .	57
4.2.1	Effect of PMD on RF power . . . . .	58
4.2.2	CD-Insensitive PMD Monitoring Based on RF Power . . . . .	66
4.2.3	Effects of FBG Filter Bandwidth and Frequency Detuning . . . . .	68
4.3	Experimental Results . . . . .	71
4.3.1	PMD Monitoring in 38-Gbit/s DQPSK System . . . . .	72
4.3.2	PMD Monitoring in 57-Gbit/s D8PSK System . . . . .	74
4.4	Conclusions . . . . .	76
<b>5</b>	<b>CD Monitoring in High-speed Optical Transmission Systems</b>	<b>78</b>
5.1	CD Monitoring Based on RF Tone Power Ratio Measurement . . . . .	81
5.1.1	Operation Principle . . . . .	81
5.1.2	System Setup . . . . .	83
5.1.3	FBG Filter Centered at Optical Carrier Wavelength . . . . .	84
5.1.4	FBG Filter Centered at 10-GHz Away From Carrier . . . . .	92
5.2	CD Monitoring Based on Amplitude Ratio in Delay-tap Sampling Plot . . . . .	94
5.2.1	Principle of Delay-tap Sampling Plot . . . . .	95
5.2.2	Results and Discussions . . . . .	97
5.3	Conclusions . . . . .	104
<b>6</b>	<b>Suppression of Signal Fluctuation in BOTDA Sensing System</b>	<b>107</b>
6.1	Distributed Sensing System Based on SBS . . . . .	108
6.1.1	BOTDA Sensing System . . . . .	109
6.1.2	Polarization Induced Signal Fluctuation in BOTDA Sensing System . . . . .	111
6.2	Polarization Diversity Scheme in Distributed Sensing System . . . . .	112
6.3	Experimental Setup . . . . .	116

## CONTENTS

---

6.4	Experimental Results . . . . .	117
6.4.1	Distributed Temperature Measurement . . . . .	118
6.4.2	Distributed Strain Measurement . . . . .	120
6.5	Conclusions . . . . .	122
<b>7</b>	<b>Conclusions and Future Work</b>	<b>124</b>
7.1	Conclusions . . . . .	124
7.2	Future Work . . . . .	126
	<b>Bibliography</b>	<b>127</b>
	<b>List of Publications</b>	<b>146</b>

# Summary

Optical fiber plays a key role in both high-speed optical communication and sensor systems. High-speed optical fiber transmission systems have been studied for several decades and still attract a lot of attention. Optical fiber has been used in distributed sensing systems on measuring the temperature and strain along the fiber. However, the performance of both high-speed optical transmission networks and fiber sensing systems are affected by the physical effects of optical fiber. In this thesis, several topics on application of fiber nonlinear effects and management of degradations induced by fiber physical effects are studied.

Firstly, a high-speed multi-channel optical pulse train generation based on parametric process through highly-nonlinear fiber (HNLF) is demonstrated. The wavelength of pump pulse is optimized to satisfy phase-matching condition and to obtain large gain and wide bandwidth. 6-channel 80-GHz optical pulse trains with high extinction ratio are generated using one pulsed pump and three continuous wave channels. The qualities of the amplified signal and generated idler channels are analyzed numerically by calculating the bit-error rate of each channel.

Secondly, chromatic dispersion (CD) and polarization-mode dispersion (PMD) monitoring method in high-speed transmission systems is proposed. The methods are based on radio frequency (RF) power measurement and optical filtering. In the absence of filter, RF power is affected by both CD and PMD. By filtering the optical compo-



nents in one of sidebands, the CD effect can be eliminated and PMD measurement can be achieved. The power ratio of filtered and non-filtered signal is only affected by CD; therefore, PMD-insensitive CD monitoring can be achieved. The center wavelength of optical filter can be optimized to achieve wide measurement range and high measurement resolution. Both simulation and experimental results show that the proposed method is efficient and cost effective.

Lastly, the polarization induced signal fluctuation in Brillouin distributed sensing system is studied. A polarization diversity scheme containing two polarization beam splitters (PBSs) and a piece of single-mode fiber (SMF) is proposed. Both theoretical analysis and experimental results show that the proposed scheme is efficient on eliminating polarization induced fluctuation in Brillouin optical time domain analysis (BOTDA) fiber optic distributed sensing system. This scheme does not need any feedback control and the measurement time is only 3 second. Stable distributed temperature and strain measurements are demonstrated along a 1.2 km SMF.

# List of Figures

1.1	SPM-induced frequency chirp for 1-st and 3-rd order Gaussian pulses [1].	9
1.2	Output signal power and reflected SBS power as a function of input power. . . . .	11
1.3	Optical spectra of pump and signals in a multicasting system [67]. . .	14
1.4	System setup for distributed Brillouin gain spectrum measurements, which uses EOM to generate the interacting optical signals [86]. . . .	17
2.1	Experimental setup for measurement of optical parametric amplification system. PM: phase modulator. HNLF: highly nonlinear fiber. . .	25
2.2	Optical spectrum when the pump and probe wavelengthes are 1559.35 nm and 1540 nm, respectively. The pump power is 27-dBm. . . . .	26
2.3	Gain spectra of the parametric amplifier. Pump wavelength is 1560 nm, 1559.35 nm and 1559 nm respectively. Pump power is 27-dBm and signal power coupled into the HNLF is -25-dBm. . . . .	27
2.4	Gain spectra of parametric amplifier for pump power of 25 dBm, 26 dBm and 27 dBm. The pump wavelength is 1559.35 nm. Signal power coupled into the HNLF is -25 dBm. . . . .	28
2.5	Gain of the input signal and conversion efficiency of the idler. Pump wavelength is 1559.35 nm. . . . .	29

## LIST OF FIGURES

---

2.6	Experimental setup for multi-channel pulse generation. PM: phase modulator. HNLF: highly nonlinear fiber. . . . .	30
2.7	The (a) dispersion and (b) group delay of highly-nonlinear fiber as a function of wavelength. . . . .	32
2.8	Optical spectra (a) after the HNLF with three input signals (b) filtered out and amplified signal at 1547.8 nm. The pump is multiplexed to 80 GHz and amplified to 20 dBm. . . . .	32
2.9	Measured 80-GHz waveforms at signal and idler wavelengths by an auto-correlator. . . . .	33
2.10	FWHM of the signal channels, idler channels and pump pulse. . . . .	35
2.11	Simulated optical spectra at the output of HNLF. The pump is 80 GHz pulse with an average power of 20 dBm. . . . .	36
2.12	BER measurement as a function of received power for signal and idler channels (a) back-to-back (b) after 200 m transmission. The BER of 3.8 ps pulse is shown for comparison. . . . .	37
2.13	BER measurement as a function of received power for (a) 1547.8 nm and (b) 1570.9 nm. In back-to-back case. . . . .	38
2.14	BER measurement as a function of received power for (a) 1547.8 nm and (b) 1570.9 nm. After 200 m transmission. . . . .	39
3.1	Experimental setup for multi-wavelength light source generation in a Loop. . . . .	44
3.2	Simulated optical spectrum generated by single PM in a loop structure. No EDFA in the loop. . . . .	46
3.3	Simulated optical spectrum generated by single PM in an amplified loop. With EDFA in the loop. . . . .	47
3.4	Detailed optical spectrum at 1562 nm. . . . .	48

## LIST OF FIGURES

---

3.5	Measured optical spectrum generated by single PM in a loop structure. No EDFA in the loop. . . . .	49
3.6	Measured optical spectrum generated by single PM in an amplified loop. With EDFA in the loop. . . . .	50
3.7	Measured detailed optical spectrum at 1562 nm. . . . .	50
3.8	Measured optical spectra when the PM driven by clocks with different repetition rates. . . . .	51
4.1	Principle of PMD monitoring for NRZ data. . . . .	56
4.2	System setup of CD-insensitive PMD monitoring based on RF power measurement. . . . .	57
4.3	40-Gbit/s DQPSK signal (a) optical spectrum; (b) Relative RF power as a function of DGD at different CD values. . . . .	59
4.4	40-Gbit/s DPSK signal (a) Optical spectrum of filtered signal; elec- trical spectra for (b) DGD=0ps, (c) DGD=25ps, and (d) DGD=50ps. CD=0ps/nm. . . . .	60
4.5	Electrical spectra of filtered 40-Gbit/s DPSK signal for (a) CD=100ps/nm, (b) CD=200ps/nm, (c) CD=300ps/nm, and (d) CD=400ps/nm. DGD=25ps. . . . .	61
4.6	(a) Optical spectrum of filtered 40-Gbit/s duobinary signal and elec- trical spectra for (b) DGD=0ps, (c) DGD=25ps, and (d) DGD=50ps. CD=0ps/nm. . . . .	62
4.7	Electrical spectra of filtered 40-Gbit/s duobinary signal for (a) CD=100ps/nm, (b) CD=200ps/nm, (c) CD=300ps/nm, and (d) CD=400ps/nm. DGD=25ps. . . . .	63
4.8	(a) Optical spectrum of filtered 40-Gbit/s DQPSK signal and elec- trical spectra for (b) DGD=0ps, (c) DGD=25ps, and (d) DGD=50ps. CD=0ps/nm. . . . .	64

## LIST OF FIGURES

---

4.9	Electrical spectra of filtered 40-Gbit/s DQPSK signal for (a) CD=100ps/nm, (b) CD=200ps/nm, (c) CD=300ps/nm, and (d) CD=400ps/nm. DGD=25ps	65
4.10	Relative RF power as a function of DGD at different CD for 40-Gbit/s DPSK signal when FBG filter is centered at 10-GHz and 40-GHz away from the carrier. . . . .	66
4.11	Relative RF power at 10 GHz as a function of DGD for different CD in 40-Gbit/s system: (a) CSRZ; (b) DPSK; (c) DQPSK; (d) Duobinary.	67
4.12	Dynamic range of RF tone power at 10 GHz as a function of FBG bandwidth in 40-Gbit/s system. . . . .	68
4.13	Relative 10GHz RF power as a function of DGD under FBG filter frequency detuning in 40-Gbit/s (a) DQPSK and (b) duobinary systems. .	69
4.14	Dynamic range of 10 GHz RF power as a function of electrical filter bandwidth (a) in duobinary, DQPSK and DPSK systems; (b) for different filter orders. . . . .	70
4.15	Experimental setup of PMD monitoring utilizing FBG notch filter in an 8-PSK system. LD: laser diode; PM: phase modulator. . . . .	71
4.16	Optical spectrum of 38-Gbit/s DQPSK signal filtered by a narrow band FBG notch filter. . . . .	72
4.17	RF power at 10-GHz as a function of DGD for different CD values in 38-Gbit/s DQPSK system. . . . .	73
4.18	Optical spectrum of 57-Gbit/s D8PSK signal filtered by a narrow band FBG notch filter. . . . .	74
4.19	RF power at 10-GHz as a function of DGD for different CD values in 57-Gbit/s D8PSK system. . . . .	75
4.20	RF spectra of 38-Gb/s DQPSK signal for different DGD values. . . .	75

## LIST OF FIGURES

---

5.1	Principle of RF clock power changing under CD and PMD for NRZ and filtered NRZ signals. . . . .	82
5.2	System setup of PMD-insensitive CD monitoring based on RF power measurement. . . . .	83
5.3	Simulation results of 38-Gbit/s NRZ-DQPSK (a) optical spectrum of signal filtered by FBG filter; (b) RF clock power versus CD of nonfiltered signal; (c) RF clock power versus CD of filtered signal; (d) RF clock power ratio versus CD. . . . .	85
5.4	Simulation results of 57-Gbit/s NRZ-D8PSK (a) optical spectrum of signal filtered by FBG filter; (b) RF clock power versus CD of nonfiltered signal; (c) RF clock power versus CD of filtered signal; (d) RF clock power ratio versus CD. . . . .	87
5.5	Simulated RF clock power ratio change as a function of FBG frequency detuning in (a)38-Gbit/s NRZ-DQPSK and (b)57-Gbit/s NRZ-D8PSK systems. . . . .	87
5.6	Transmission spectrum of fiber Bragg grating. . . . .	88
5.7	Experimental results of 38-Gbit/s NRZ-DQPSK (a) optical spectrum of signal filtered by FBG filter; (b) RF clock power versus CD of nonfiltered signal; (c) RF clock power versus CD of filtered signal; (d) RF clock power ratio versus CD. . . . .	89
5.8	Experimental results of 57-Gbit/s NRZ-D8PSK (a) optical spectrum of signal filtered by FBG filter; (b) RF clock power versus CD of nonfiltered signal; (c) RF clock power versus CD of filtered signal; (d) RF clock power ratio versus CD. . . . .	91

## LIST OF FIGURES

---

5.9	38-Gbit/s DQPSK (a) optical spectrum of signal filtered by FBG; (b) Relative 10-GHz RF power versus CD. (lines for simulation; stars for experiment) . . . . .	93
5.10	57-Gbit/s D8PSK (a) optical spectrum of 57-Gb/s NRZ-D8PSK signal filtered by FBG; (b) Relative 10-GHz RF power versus CD. (lines for simulation; stars for experiment) . . . . .	94
5.11	Principle of delay-tap asynchronous sampling for RZ DQPSK signal. (a) waveforms in time domain; (b) eye diagram; (c) delay-tap plot ( $\Delta t = \text{symbol period}/2$ ). $T_s$ : sampling period; $\Delta t$ : time offset. . . . .	96
5.12	System setup for dispersion monitoring based on delay-tap sampling. $T_X$ : transmitter; EDFA: Erbium doped fiber amplifier. . . . .	98
5.13	40-Gbit/s 67% CSRZ DQPSK signal (a)-(c) eye diagrams and (d)-(f) delay-tap plots with different residual CD. . . . .	99
5.14	Simulated amplitude ratio in delay-tap sampling plot as a function of chromatic dispersion. 40-Gbit/s 67% CSRZ DQPSK signal. . . . .	100
5.15	40-Gbit/s 50% RZ DQPSK signal(a)-(c) eye diagrams and (d)-(f) delay-tap plots with different residual CD. . . . .	101
5.16	Simulated amplitude ratio in delay-tap sampling plot as a function of chromatic dispersion. 40-Gbit/s 50% RZ DQPSK signal. . . . .	102
5.17	60-Gbit/s 50% RZ D8PSK signal(a) eye diagrams and (b)-(e) delay-tap plots with different residual CD. . . . .	103
5.18	Simulated amplitude ratio in delay-tap sampling plot as a function of chromatic dispersion. 60-Gbit/s 55% RZ D8PSK signal. . . . .	105
6.1	EOM transmitted optical intensity as a function of the applied voltage and a function of time. . . . .	110

## LIST OF FIGURES

---

6.2	Maximum and minimum gain achievable in the measurement of the BGS of a highly birefringent dispersion shifted fiber [92]. . . . .	111
6.3	The fluctuations of Brillouin gain due to the relative polarization state between pump and probe waves. (a) The probe wave is parallel to the pump wave, without polarization diversity. (b) The probe wave is orthogonal to the pump wave, without polarization diversity. (c) The probe wave is orthogonal to the original pump wave, with polarization diversity. (d) The probe wave is aligned at to the original pump wave, with polarization diversity. . . . .	113
6.4	Experimental set-up of BOCDA fiber optic distributed sensing system with a polarization diversity scheme on the pulsed pump wave. . . . .	115
6.5	Measured temperature distribution along 1.2 km SMF in the environment of room temperature (a) without polarization diversity and (b) with polarization diversity by the proposed scheme. . . . .	118
6.6	Measured temperature distribution along 1.2 km SMF when putting a section of fiber at the location of 1.1 km into hot water (a) without polarization diversity and (b) with polarization diversity by the proposed scheme. . . . .	119
6.7	Measured distributed strain along 1.2 km SMF under normal (a) without polarization diversity and (b) with polarization diversity by the proposed scheme. . . . .	120
6.8	Measured distributed strain along 1.2 km SMF with a strain-applied section at the location of 1.1 km (a) without polarization diversity and (b) with polarization diversity by the proposed scheme. . . . .	121



# List of Tables

2.1 Parameters of the HNLFF used in the experiment. . . . . 25

# List of Abbreviations

BER	Bit Error Rate
BOTDA	Brillouin Optical Time Domain Analysis
BGS	Brillouin Gain Spectrum
CS-RZ	Carrier Suppressed Return-to-Zero
CW	Continuous Wave
D8PSK	Differential 8-level Phase-Shift Keying
DCF	Dispersion Shifted Fiber
DGD	Differential Group Delay
DOP	Degree-of-Polarization
DPSK	Differential Phase-Shift Keying
DQPSK	Differential Quadrature Phase-Shift Keying
DWDM	Dense Wavelength Division Multiplexing
EA	Electro-absorption
EDFA	Erbium Doped Fiber Amplifier
ER	Extinction Ratio
FBG	Fiber Bragg Grating
FWM	Four-Wave-Mixing
FUT	Fiber Under Test

## Abbreviations

---

HNLF	Highly-Nonlinear Fiber
NOLM	Nonlinear Optical Loop Mirror
OPA	Optical Parametric Amplifier
OSA	Optical Spectrum Analyzer
OTDM	Optical Time-Division Multiplexing
PBS	Polarization Beam Splitter
PC	Polarization Controller
PD	Photodetector
PM	Polarization-Maintaining
PRBS	Pseudorandom Binary Sequence
PSP	Principal-States-of-Polarization
RF	Radio-Frequency
RZ	Return-to-Zero
SBS	Stimulated Brillouin Scattering
SMF	Single Mode Fiber
SNR	Signal-to-Noise Ratio
SOP	State-of-Polarization
XPM	Cross Phase Modulation

# Chapter 1

## Introduction

Optical fiber transmission systems have been studied for several decades and still attract a lot of attentions. Thanks to the property of high bandwidth and low loss in optical fibers, multi-channel long-haul transmission between continents has been achieved. Recently, the high-speed internet as well as high-definition television have been realized as a benefit of large bandwidth in optical transmission systems. Besides transmission systems, optical fiber can also be utilized as a detector in fiber sensor systems. Various parameters, such as temperature, strain along the fiber, can be measured owing to the physical effects of optical fibers. Compared with conventional sensors which contains electronic components, optical fiber sensors have many advantages, such as immunity to electromagnetic interference, flexibility, light weight and stable chemical characteristic. Therefore, optical fiber sensors are applicable to various environments.

The performances of both high-speed optical transmission systems and optical sensor systems are affected by the physical effects of optical fibers. In order to obtain high performance in optical systems, fiber physical effects should be studied and managed. On the other hand, fiber physical effects have a lot of applications such as wavelength conversion, optical signal processing and optical sensor. Therefore, the

## 1.1 The Physical Effects in Optical Fibers

---

management of fiber physical effects is important in both optical transmission and sensor systems. In this chapter, the physical effects of optical fibers are introduced in section 1.1. The limitation and applications of the nonlinearities in high-speed optical transmission systems are discussed in section 1.2. The applications of nonlinear effects in optical sensing systems are analyzed in section 1.3. The objectives of the work are presented in section 1.4.

### 1.1 The Physical Effects in Optical Fibers

Optical fiber transmission is based on the phenomenon of total internal reflection which is achieved by the difference of refractive index between the core and cladding of fibers. Beside the basic property, many other characteristics of optical fiber have been studied and managed to achieve better performance in optical transmission and sensor systems. Chromatic dispersion (CD) and polarization-mode dispersion (PMD) limit the performance of optical transmission systems, especially the high bit-rate systems. The nonlinear effects, such as self-phase modulation (SPM), cross-phase modulation (XPM), parametric processes, stimulated Raman scattering (SRS), and stimulated Brillouin scattering (SBS), have been studied extensively in optical systems. The fiber physical effects as well as their characteristics are discussed in this section.

#### Chromatic Dispersion

Chromatic dispersion is one of major effects limiting the transmission length in high-speed optical transmission systems. As higher bit-rate ( $>100\text{-Gbit/s}$ ) transmissions are required in the future networks, the pulse trains are much narrower, the CD and PMD tolerances become much smaller. The chromatic dispersion is induced because the response to a electromagnetic wave in optical fibers depends on the optical frequency  $\omega$

## 1.1 The Physical Effects in Optical Fibers

---

[1]. The effects of fiber dispersion can be explained by the mode-propagation constant  $\beta$  in a Taylor series relative to the frequency  $\omega$ :

$$\beta(\omega) = \beta_0 + \beta_1(\omega - \omega_0) + \frac{1}{2}\beta_2(\omega - \omega_0)^2 + \dots, \quad (1.1)$$

where

$$\beta_m = \left( \frac{d^m \beta}{d\omega^m} \right)_{\omega=\omega_0}, \quad (1.2)$$

$\beta_1$  and dispersion  $D$  are related to the refractive index  $n$ :

$$\beta_1 = \frac{1}{v_g} = \frac{n_g}{c} = \frac{1}{c} \left( n + \omega \frac{dn}{d\omega} \right), \quad (1.3)$$

$$D = \frac{d\beta_1}{d\lambda} = -\frac{2\pi c}{\lambda^2} \beta_2 \approx \frac{\lambda}{c} \frac{d^2 n}{d\lambda^2} \quad (1.4)$$

As a result of chromatic dispersion, the signal at different wavelengths has different transmission speeds. The signal spectra is broadened by CD, which limits the transmission bit rate. CD compensation has long been studied and many methods have been proposed, such as dispersion-compensating fiber (DCF). The dispersion can be changed by varying the core diameter and the core-cladding index difference of the fiber.

## Polarization-mode Dispersion

The polarization mode dispersion (PMD) is induced by the birefringence in the optical fiber. The light in single mode fiber actually contains two orthogonal modes which propagate at slightly different speeds along the two axes (fast axis and slow axis) of the fiber. The mode-propagation constant  $\beta$  is different for the two modes. The strength of modal birefringence is

$$B_m = \frac{|\beta_x - \beta_y|}{k_0} = |n_x - n_y|, \quad (1.5)$$

## 1.1 The Physical Effects in Optical Fibers

---

where  $\beta_x$  and  $\beta_y$  are the mode propagation constant at the two orthogonal polarization states,  $n_x$  and  $n_y$  are the modal refractive indices for the two orthogonal polarization states. After transmission through a fiber link with birefringence, the two states will have a time spread, which induces the broadening of the optical pulse. If the time spread and the symbol duration are comparable, the pulse is distorted and the system performance is degraded. PMD is a time varying effect, and it is affected by the environment changes. PMD changes randomly in the fiber and optical components. It has been studied extensively as it limits the performance of the high-speed optical transmission and sensor systems [2,3].

### Self-Phase Modulation and Cross-Phase Modulation

Self-phase modulation (SPM) and cross-phase modulation (XPM) occur in nonlinear optical media. They result in intensity dependent refractive index changing, which leads to spectral broadening of optical pulses. SPM was first observed in 1967 in the transient self-focusing of optical pulses propagating in a  $CS_2$ -filled cell [4]. A study of SPM in a silica-core fiber was reported in [5].

The SPM-induced spectral broadening is a result of the time dependence of nonlinear phase shift  $\Phi_{NL}$ . A temporally varying phase implies that the instantaneous optical frequency differs from its central value  $\omega_0$ , which is referred to as frequency chirping. The chirp induced by SPM increases in magnitude with the propagated distance [1]. Therefore, new frequency components are generated continuously as the pulse propagates in the fiber link. These SPM-generated frequency components broaden the spectrum over its initial width. The temporal variation of the induced chirp  $\delta\omega$  has several features. First,  $\delta\omega$  is negative near the leading edge and becomes positive near the trailing edge of the pulse. Second, the chirp is linear and positive over a large central region of the Gaussian pulse. Third, the chirp is considerably larger for

## 1.1 The Physical Effects in Optical Fibers

---

pulses with steeper leading and trailing edges. Fourth, super-Gaussian pulses behave differently than Gaussian pulses because the chirp occurs only near pulse edges and does not vary in a linear fashion.

If the optical pulse is very short and the dispersion length is comparable to the fiber length, it is necessary to consider the combined effects of group-velocity dispersion (GVD) and SPM [6]. In the normal-dispersion regime ( $\beta_2 > 0$ ), the pulse broadening rate is increased by the effect of SPM. This is because red-shifted and blue-shifted frequencies are generated in the leading and trailing edge, respectively. In other words, more frequency components are generated through SPM. Therefore, the pulse broadening rate is faster under the effect of SPM. In the anomalous-dispersion regime ( $\beta_2 < 0$ ) of optical fiber, the SPM-induced positive chirp and GVD-induced negative chirp nearly cancels each other, and the optical soliton can be achieved.

If more than one optical pulses with different wavelengths propagate in fiber link, they will interact with each other through optical nonlinear effects. One of the effects, with no energy transfer, is XPM [7]. Similar to SPM, the combined effects of GVD and XPM may support soliton pairs transmit in the anomalous-dispersion regime of the optical fiber. Both SPM and XPM are elastic nonlinear effects, where no energy transition occurs between the input light and nonlinear medium.

### **Stimulated Raman Scattering and Stimulated Brillouin Scattering**

Stimulated Raman scattering (SRS) is an inelastic scattering which can transfer energy from one wavelength to another. It was first observed in 1962 [8]. In the SRS process, an intense incident light, serving as a pump, transfers most of its energy to a frequency-shifted light, called the Stokes wave, as long as the frequency difference of the two light equals to the Raman shift (about 13.2 THz in pure silica). Optical phonon is involved in the process. The scattering can be described quantum-mechanically as if annihilation



## 1.1 The Physical Effects in Optical Fibers

---

of a pump photon creates a Stocks photon and a optical phonon simultaneously. The frequencies and wave vectors of the waves can be expressed by

$$\omega_V = \omega_p - \omega_s, k_V = k_p - k_s, \quad (1.6)$$

where  $\omega_V$  is the vibration frequency of the optical phonon;  $\omega_p$  and  $\omega_s$  are the frequencies of pump light and stocks wave, respectively.  $k_V$ ,  $k_p$ , and  $k_s$  are the wave vectors. SRS effect has been studied extensively on Raman amplifiers [9–11] and tunable Raman lasers [12–15].

Stimulated Brillouin scattering (SBS), first observed and studied in 1964 [16, 17], is a nonlinear effect which is similar to SRS. Acoustical phonon is involved in the process. Frequency downshifted Stocks wave is generated through SBS. The scattering can be viewed quantum-mechanically as if a pump photon disappeared and gives its energy to Stocks wave and an acoustic phonon. Both energy and momentum should be conserved during the process. The frequencies and wave vectors of the waves can be expressed by

$$\Omega_A = \omega_p - \omega_s, k_A = k_p - k_s, \quad (1.7)$$

where  $\Omega_A$  is the frequency of the acoustic wave, also known as Brillouin shift;  $\omega_p$  and  $\omega_s$  are the frequencies of pump light and stocks wave, respectively.  $k_A$ ,  $k_p$ , and  $k_s$  are the wave vectors. The Brillouin shift is determined by the refractive index of nonlinear medium. SBS has been used to achieve fiber based Brillouin amplifiers [18, 19] and lasers [20–22]. However, SBS is different from SRS in several aspects. Firstly, only backward propagating Stokes wave is generated through SBS; whereas, SRS occurs in both forward and backward direction. Secondly, the Stocks shift (about 11 GHz in the 1550 nm region) is much smaller than that of SRS. Thirdly, SBS has lower threshold than SRS. As a result, SBS is harmful to the optical communication systems [23, 24].

## 1.1 The Physical Effects in Optical Fibers

---

### Parametric Processes

Parametric process is a nonlinear phenomena, where the optical fibers play a passive role in the process. The frequency of generated wave does not depend on the property of nonlinear medium, but the applied optical field. Parametric process includes four-wave mixing (FWM) and harmonic generation, both of which generate waves with new frequencies. It can be classified as second- or third-order process depending on whether the second-order susceptibility  $\chi^{(2)}$  or third-order susceptibility  $\chi^{(3)}$  is responsible for the parametric process [1]. As the silica is an isotropic medium, second-order susceptibility  $\chi^{(2)}$  vanished and no second-order harmonic occurs in optical fibers.

The third-order parametric processes include third harmonic generation, four-wave mixing and parametric amplification [25,26]. Four-wave mixing is one of important parametric processes as it is an efficient phenomenon on new frequencies generation. In general, if three optical waves with frequencies  $\omega_1$ ,  $\omega_2$ , and  $\omega_3$  are transmitting in the fiber simultaneously, a new wave  $\omega_4$  will be generated through FWM. The generated frequency could be

$$\omega_4 = \omega_1 \pm \omega_2 \pm \omega_3, \quad (1.8)$$

It seems that  $\omega_4$  can be anyone of them. However, in order to achieve efficient FWM, phase-matching condition should be satisfied:

$$k_1 + k_2 = k_3 + k_4, \quad (1.9)$$

where  $k_1$ ,  $k_2$ ,  $k_3$ ,  $k_4$  are wave vectors. The phase-matching condition is easy to be satisfied when  $\omega_4 = \omega_1 + \omega_2 - \omega_3$ . Therefore, this frequency will be generated through FWM. If  $\omega_1 = \omega_2$ , only three waves with different frequencies are involved in the nonlinear process. It is called three-wave mixing, also known as degenerate FWM.

### 1.2 High-Speed Optical Transmission Systems

It is well known that optical fiber transmission is based on the phenomenon of total internal reflection which is realized by the refractive index difference between the core and cladding of optical fiber. Beside the basic property, many other characteristics of optical fiber have been studied to achieve higher bit-rate, longer distance, and better performance in optical transmission systems. As the pulse trains in the high bit-rate transmission systems are narrower, the CD and PMD tolerances become much smaller. Therefore, accurate and dynamic CD and/or PMD monitoring and compensation methods have attracted a lot of interests. In WDM systems, the nonlinear effects of optical fiber may lead to interchannel and intrachannel crosstalk which degrades the performance of system. Besides, the channel spacing of dense wavelength-division multiplexing (DWDM) systems becomes smaller ( $\sim 50$ -GHz) in order to improve the spectral efficiency. The FWM induced crosstalk between different channels is increased. On the other hand, nonlinear effects can also be used in many applications, such as optical wavelength conversion, optical pulse generation and signal processing. In this section, the limitations as well as applications of fiber physical effects in optical transmission systems are introduced.

#### 1.2.1 Limitations of Fiber Physical Effects

Chromatic dispersion (CD) is a linear effect in optical fiber. As EDFA eliminates the problem of fiber loss in long-haul transmission systems, CD becomes a key effect which limits the transmission length in high-speed transmission systems. The bit rate-distance product of a transmission system is limited by the dispersion. The effect of dispersion on the bit rate  $B$  can be estimated by using criterion [27]

$$BL|D|\Delta\lambda < 1, \quad (1.10)$$

## 1.2 High-Speed Optical Transmission Systems

---

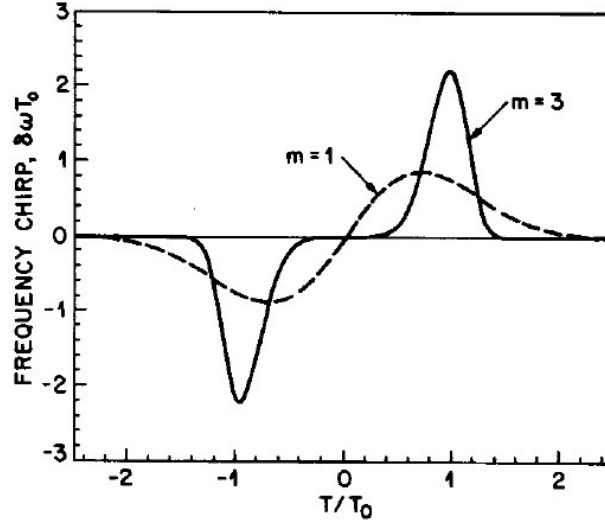


Figure 1.1: SPM-induced frequency chirp for 1-st and 3-rd order Gaussian pulses [1].

where  $D$  is dispersion parameter,  $L$  is transmission length and  $\Delta\lambda$  is the spectral width of laser source.

On the other hand, CD accumulates in the fiber links and various optical components. It may change with network reconfigurations and many environmental conditions. Therefore, dispersion management is a key issue in high bit-rate, long-haul transmission systems. CD management can be implemented at the transmitter, at the receiver, or along the fiber link [28–32].

Nonlinear effects play an important role in the optical fiber. This is due to the fact that response of any dielectric to light becomes nonlinear for intense electromagnetic fields [27]. Although silica is not a highly nonlinear material, nonlinear effects are quite important in the optical transmission systems as the light is confined in a small area in the fiber. Nonlinear effect is one of key issues which limit the transmission power. The nonlinear effects degrade the performance of lightwave systems in following aspects.

Self-phase modulation leads to frequency chirping of optical pulses. The fre-

## 1.2 High-Speed Optical Transmission Systems

---

frequency chirp is proportional to the derivative  $dP/dt$  and also depends on the shape of optical pulse.  $P$  is optical power. Fig.1.1 shows the frequency chirp varies as a function of time for 1-st and 3-rd order Gaussian pulses [1]. The SPM induced frequency chirp changes pulse shape through the effect of dispersion. SPM-induced phase shift accumulates over multiple amplifiers. In order to reduce the effect of SPM in the transmission system, the input peak power should satisfy [27]

$$P_{in} < 0.1\alpha/(\gamma N_A), \quad (1.11)$$

where  $\alpha$  is the fiber loss,  $\gamma$  is nonlinear coefficient of fiber and  $N_A$  is the number of amplifiers in the transmission link. Therefore, SPM limits the optical power and transmission length of lightwave systems.

In the DWDM systems, the interference between different channels should be taken into consideration. XPM is one of phenomena which leads to crosstalk between different channels. The phase shift of a channel does not depend only on the power of the channel but also other channels through XPM. Besides, the dispersion of each channel is different, the XPM induces pulse shape change.

The nonlinear phenomena of SPM and XPM change the phase of one or other channels, and no energy is transferred in the processes. The inelastic scattering, SRS and SBS, may transfer energy from one field to another. In WDM systems, the optical power is converted from longer wavelength to lower wavelength as long as their spacing is within the Raman spectrum through SRS. As the power change is bit pattern dependent, the performance is degraded and power penalty is introduced in the transmission system [27]. Therefore, SRS affects the performance of WDM systems considerably if the optical power exceeds the threshold. Methods on reducing of Raman crosstalk have been proposed in [34, 35].

SBS does not lead to interchannel crosstalk in WDM systems, which is due to the fact that the Brillouin shift ( $\sim 10$  GHz) is smaller than the channel spacing of WDM

## 1.2 High-Speed Optical Transmission Systems

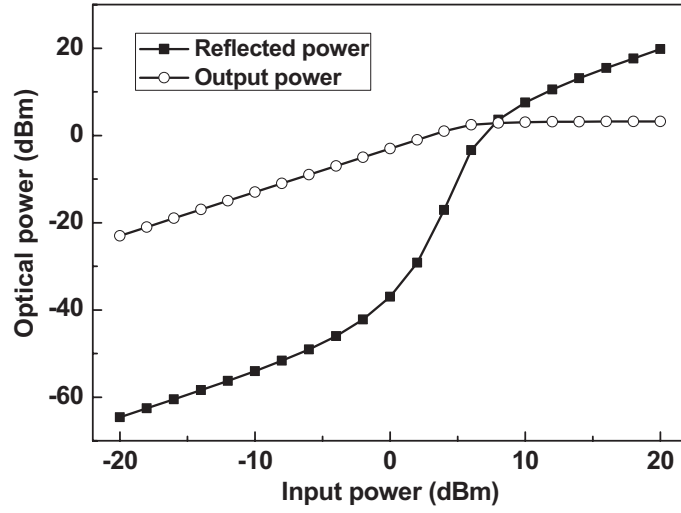


Figure 1.2: Output signal power and reflected SBS power as a function of input power.

systems and the Brillouin gain bandwidth ( $\sim 20$  MHz) is extremely narrow. However, as Stokes wave propagates in the backward direction in SBS, the reflection signal power increases dramatically if the threshold value is achieved. Fig.1.2 shows the output optical power and reflected SBS power as a function of input power in a 15 km single-mode fiber. It is observed that once the input power achieves a critical value, most of optical power is reflected back through SBS effect. Therefore, the channel power is limited to a few milliwatts by the SBS process. Fig.1.2 was obtained when the input light was a continuous wave. If short pulses were transmitting in the fiber link, the SBS threshold increases [36]. For a short pulse whose width is much smaller than the phonon lifetime, Brillouin gain is reduced below the Raman gain [1]. Besides, the SBS threshold depends on the polarization state of input power. It increases by 50% when the pump field is completely polarization scrambled [37]. Several methods have been proposed to increase SBS threshold [38–40] and thus to increase the signal launch power. Phase modulation is one of efficient methods on SBS suppression.

The FWM induced power transfer results in power loss and interchannel crosstalk, both of which degrade the performance of optical transmission systems [41,42]. In the

## 1.2 High-Speed Optical Transmission Systems

---

system, where the channels are not equally spaced, most of generated frequencies will fall in between the channels. Therefore, the interchannel crosstalk is not as severe as that in the equally spaced system [41, 43]. However, the unequal channel spacing is not practical. As the efficiency of FWM depends on the phase-matching condition of the involved waves, it can be suppressed by breaking the phase-matching condition. WDM systems eliminate FWM by using the technique of dispersion management in which GVD is locally high while it is quite low in average [44, 45].

### 1.2.2 Applications of Fiber Physical Effects

Although nonlinear effects of optical fiber induce performance degradation in transmission systems, they are also useful in optical systems. Various applications, such as fiber amplifier, fiber laser, soliton transmission, and wavelength conversion, have been extensively studied [46–69].

Soliton transmission in optical fiber is based on the balance of group-velocity dispersion (GVD) and SPM/XPM. In a soliton transmission system, the optical pulse can maintain their width over long distance. The use of soliton was proposed in 1973 [46] and it has been studied extensively in the following decades [47–49].

Fiber amplifier can be realized by nonlinear effects, such as SRS, SBS and parametric process. Optical phonons, which have relatively larger energy compared with acoustical phonons, are involved in SRS, and the Raman gain bandwidth is quite wide ( $\sim 5$  THz); while acoustic phonons, which have relatively small energy, are involved in SBS, and the Brillouin gain bandwidth is very narrow ( $\sim 20$  MHz). The large bandwidth of Raman amplifiers makes them attractive in the optical transmission systems [50, 51]. Three channels semiconductor laser were amplified simultaneously in a Raman amplifier with a pump of 1470 nm [50]. Raman amplifiers can cooperate with erbium-doped fiber amplifier (EDFA) to achieve large gain bandwidth for WDM

## 1.2 High-Speed Optical Transmission Systems

---

systems. A fiber amplifier with a bandwidth of 80 nm and gain of 30 dB was realized by combining an EDFA and two Raman amplifiers [51]. Nearly uniform gain was achieved in the region of 1530 to 1610 nm. The optical fibers were designed to have broad band and flat Raman gain [52, 53]. A simulation result showed that a 3 dB Raman gain bandwidth of 90 nm can be achieved by choosing the parameters of a dual core fiber [52]. A tellurite-based fiber was reported and a Raman amplifier with a bandwidth of 160 nm and gain of 10 dB was achieved [53]. For the fiber amplifiers based on parametric process, phase-matching is a key issue. Dispersion shifted fiber [56, 57] and dispersion flattened fiber [58] have been studied to achieve the phase-matching condition in the parametric processes. A parametric amplifier with a bandwidth of 47 nm using DSF was reported [57]. In [54], a parametric amplifier with a gain of 70 dB was proposed. In [55], a combination of Raman and parametric amplifier with gain bandwidth of 200 nm was achieved.

The use of FWM for wavelength conversion [59–63] has attracted a lot of interests owing to the ultra-fast nonlinear effect. Conversion efficiency is one of key parameters in the all-optical wavelength conversion system. In order to achieve high conversion efficiency through FWM, optical fibers with high nonlinear coefficient  $\gamma$  has been employed [62, 63]. In [62], the fiber nonlinear coefficient and dispersion slope are  $25 \text{ W}^{-1} \text{ Km}^{-1}$  and  $+0.010 \text{ ps/nm}^2/\text{km}$ , respectively. Conversion efficiency is improved by 8 dB compared to conventional highly nonlinear fiber (HNLF). In [63], Bismuth highly nonlinear fiber (Bi-HNLF) with a nonlinear coefficient of  $1100 \text{ W}^{-1} \text{ Km}^{-1}$  was reported. As the FWM process is affected by the phase-matching condition, which depends on the dispersion and dispersion slope of nonlinear medium. Optical fibers with flat dispersion [64, 65] was developed to achieve larger conversion bandwidth. In [65], a dispersion of  $-3 \text{ ps}/(\text{km} \cdot \text{nm})$  over 1500-1600 nm was applied and a conversion bandwidth of 40 nm was achieved.



### 1.3 Optical Sensor Systems

---

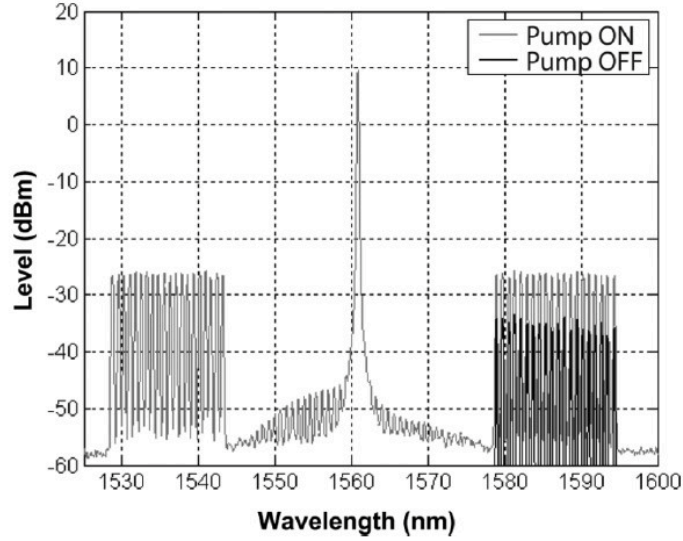


Figure 1.3: Optical spectra of pump and signals in a multicasting system [67].

FWM is a ultra-fast process, and it can be used to make all-optical multicasting [63,66,67]. A 1-to-40 multicasting with 100 GHz channel spacing was reported in [67]. A 100 m HNLF with nonlinear coefficient  $\gamma$  of  $16W^{-1}Km^{-1}$  was utilized. Fig.1.3 shows the optical spectra of the pump and generated signals [67]. Another application of FWM is optical demultiplexing for the optical time domain multiplexing (OTDM) signal [68], which is also because it is an ultra-fast process. All-optical delay line was proposed by combining dispersion and wavelength conversion through FWM in [69].

### 1.3 Optical Sensor Systems

Optical fiber sensors based on fiber physical effects have been extensively studied and widely used as they are flexible, light weighted, immune to electromagnetic interference, and have stable chemical characteristic. Therefore, fiber sensors are applicable to various environments. FBG based fiber sensors have been used in instrumentation applications, such as oil leak detection, flow measurement and displacement moni-

### 1.3 Optical Sensor Systems

---

toring [71–83]. By using optical fiber as a detector, distributed fiber sensing systems can be achieved through SBS process. Various parameters, such as temperature, strain along optical fiber, can be measured by SBS based optical sensing systems [84–89]. Besides, In this section, optical sensor using fiber Bragg grating as well as the distributed fiber sensor based on nonlinear effect (stimulated Brillouin scattering) are introduced.

#### 1.3.1 Optical Sensor Based on Fiber Bragg Grating

Fiber Bragg grating (FBG) is an optical filter, whose center frequency is determined by Bragg wavelength  $\lambda_B = 2\bar{n}\Lambda$ , where  $\Lambda$  is the grating period and  $\bar{n}$  is the average mode index. The refractive index of FBG changes periodically along the grating, and the frequencies close to Bragg wavelength  $\lambda_B$  are reflected back [27]. Bragg wavelength  $\lambda_B$  is affected by many environment factors, such as temperature, strain and refractive index of surrounding material [70]. It was also widely used in bridge, petroleum tube, river surveillance monitoring, and civil structural monitoring.

Depending on the change of refractive index in FBG, it can be divided to uniform fiber Bragg gratings, chirped fiber Bragg gratings, tilted fiber Bragg gratings, and long-period fiber gratings. In a uniform FBG, the period grating is a constant, which is around  $500nm$ . Various applications of uniform FBG have been reported [71–73].

Chirped FBGs have a relative wide stop band and were proposed to compensate dispersion in telecommunication systems [27]. The chirped FBG with linear variation of the grating period reflects a spectral band of light with roughly equal intensity. Perturbations of the uniformly increasing grating period caused by local strain produce changes in the reflected spectrum [74]. Chirped FBGs have been applied on damage monitoring in composite materials, bonded joints and sandwich structures [74–76]. The sensors not only detect strain but also locate the position of damage in composite

### 1.3 Optical Sensor Systems

---

materials.

In standard FBGs, the gratings are vertical to the fiber axis. In the tilted FBGs, the gratings are aligned at a certain angle to the fiber axis. The angle of tilt has an effect on the reflected wavelength and bandwidth. In tilted FBGs, a core mode resonance and several cladding-mode resonances appear simultaneously. The cladding modes are sensitive to external perturbations (e.g., temperature, strain, refractive index, bending), while the core mode is only sensitive to temperature and strain. In practice, the temperature sensitivity of the cladding modes is similar to that of the core mode. The temperature influence can thus be removed from a comparison between the shifts of the core mode and the selected cladding modes [77]. Temperature-independent sensors can therefore be realized without requiring any additional device for compensation [78,79]

Long-period fiber grating (LPG), whose period is in the range of  $100\mu m$  to  $1mm$ , was reported in 1996 [80]. The high attenuation of the cladding modes results in multiple attenuation bands centered at discrete wavelengths. Each attenuation band corresponding to the coupling to a different cladding mode. LPGs have potential applications in sensing strain, temperature, bend radius and external index of refraction [81]. Besides, multi-parameter sensors, which can measure several environment parameters simultaneously, have been developed [82,83].

#### 1.3.2 Distributed Fiber Sensor Based on Brillouin Optical Time Domain Analysis

Stimulated Brillouin scattering has relatively low threshold compared with other non-linear effects. It can be used to make distributed fiber sensors over long distances [84–89]. The Brillouin gain spectrum (BGS) is affected by temperature and strain along the fiber under test (FUT), and can be used to monitoring these parameters. Bril-

### 1.3 Optical Sensor Systems

---

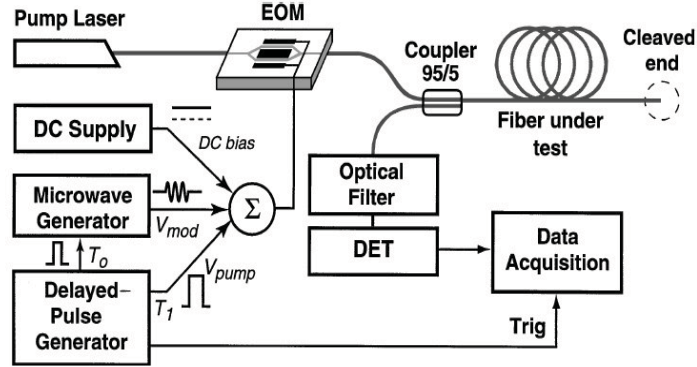


Figure 1.4: System setup for distributed Brillouin gain spectrum measurements, which uses EOM to generate the interacting optical signals [86].

Brillouin optical time domain analysis (BOTDA) is based on the interaction between a pulsed pump and a continuous probe wave counter propagating in an optical fiber [84]. When their optical frequency difference is in the BGS at some point in the fiber, the continuous light wave is amplified by the pulsed pump wave. The amplified probe wave is detected at the fiber end. If the attenuation fiber is uniform along its length, the BOTDA signal decays exponentially, corresponding to the pulsed pump suffering fiber attenuation. However, when the Brillouin frequency shift at some point in the fiber is changed, owing to a temperature or strain variation, the amplification of probe signal at that point will be changed. Thus spatially distributed temperature sensing is made possible by measuring the Brillouin frequency shift distribution with BOTDA. The sensitivity of Brillouin shift to temperature and strain applied to the fiber makes SBS highly suitable for sensing applications [85]. There is a trade-off between the spatial resolution and measurement accuracy in an BOTDA sensing system [90]. The spatial resolution depends on the pulse width. However, a short pulse will give a broadened Brillouin gain spectrum and worse measurement accuracy.

### 1.3 Optical Sensor Systems

---

A distributed temperature sensor utilizing a single laser source was proposed in [86]. The schematic diagram for distributed Brillouin gain shift measurements is shown in Fig.1.4. The pump and the probe are pulsed signals that both propagate back and forth through the sensing fiber. A spatial resolution of 45 *m* and temperature measurement resolution of 0.25 °C was achieved in a 1.2 *km* single-mode fiber. In another work, a temperature resolution of 1 °C and a spatial resolution of 5 *m* was realized for a 22 *km* fiber sensor [87]. In [88], a sensor accuracy of  $\pm 1$  °C for temperature and  $\pm 20$   $\mu\epsilon$  for deformation was proposed. The spatial resolution is 1 *m* and the sensor range is more than 20 *km*. A differential pulse pair was proposed to improve the measurement accuracy and spatial resolution in a long distance distributed temperature sensing system [89]. A temperature uncertainty of 0.25 °C and a spatial resolution of 10 *cm* was achieved over 12 *km* single-mode fiber.

SBS is a polarization sensitive process, the polarization sensitivity remains a key problem for SBS based distributed fiber sensing system. The variation of polarization state of pump and probe waves along the fiber under test will induce the polarization noise and reduce the signal to noise ratio of the fiber sensor. Several schemes have been proposed to overcome the polarization induced fluctuation in BOTDA sensing systems [91–94].

#### 1.3.3 Distributed Fiber Sensor Based on Brillouin Optical Coherent Domain Analysis

Due to the pulse-based nature of the BOTDA sensing system, the spatial resolutions are limited to several tens of centimeters. A continuous-wave-based Brillouin system, Brillouin optical correlation domain analysis (BOCDA), has been proposed and studied [96–99]. Correlation between pump and probe lightwaves are synthesized so

## 1.4 Focus and Structure of the Thesis

---

that the stimulated Brillouin scattering is generated only at a narrow section along an optical fiber. By sweeping the section, distribution of the Brillouin frequency shift is measured along the fiber. BOCDA sensing system has advantage on high spatial resolution and short measurement time 10 ( $\sim$ ms). However, the measurement range is not as long as that in BOTDA systems.

The spatial resolution of the BOCDA system is determined by the modulation parameters (amplitude and frequency) of a light source [96]. The measurement range  $d_m$  and spatial resolution  $\Delta_z$  are given by [96]

$$d_m = V_g/2f_m, \quad (1.12)$$

$$\Delta_z = V_g\Delta\nu_B/2\pi f_m\Delta f, \quad (1.13)$$

where  $V_g$  is the group velocity of light;  $f_m$  and  $\Delta f$  are the modulation frequency and the modulation amplitude of the light source;  $\Delta\nu_B$  is the Brillouin gain bandwidth in optical fibers. It is obvious that there is a trade-off between measurement range and spatial resolution.

A spatial resolution of 1 *cm* was achieved in a BOCDA strain sensor with a 2.4 *m* measurement range [97]. By using a lock-in detection scheme, a spatial resolution of 1.6 *mm* in a 5 *m* fiber was obtained in [98]. A BOCDA based structural health monitoring strain sensor was reported in [99]. The distribution of fiber Brillouin gain spectrum over 500 *m* measurement range with 50 *mm* spatial resolution and  $\pm 13 \mu\epsilon$  strain accuracy was achieved.

## 1.4 Focus and Structure of the Thesis

The organization of this thesis is as follows. Chapter 2 introduces a multi-channel high-speed optical pulse trains generation based on parametric process. The genera-

## 1.4 Focus and Structure of the Thesis

---

tion of 6-channel 80 GHz short pulse train is experimentally demonstrated through 1 km highly-nonlinear fiber. The performance of the optical parametric amplification system is demonstrated. The BER measurements of generated short pulses are analyzed in VPItransmissionMaker 7.0. Chapter 3 demonstrates multi-wavelength source generation using a single phase modulator in an amplified loop. Generation of 125-channel light source with more than 30 dB optical signal-to-noise ratio is demonstrated experimentally. In Chapter 4, a CD-insensitive PMD monitoring technique based on radio frequency (RF) power measurement is investigated. By using a FBG notch filter centered at 10-GHz away from the optical carrier, the CD effects on 10-GHz RF power can be eliminated. It is experimentally shown that the proposed scheme is efficient on CD-insensitive PMD monitoring in high-speed transmission systems. The effect of FBG filter bandwidth and frequency detuning are analyzed numerically. Chapter 5 evaluates two methods on chromatic dispersion monitoring. One is based on FBG filtering and RF power ratio measurement, the other one is based on amplitude ratio of asynchronous delay-tap sampling plot. Chapter 6 is devoted to suppression of the polarization induced signal fluctuation in BOTDA fiber distributed sensor system. A polarization diversity scheme was proposed to reduce the degree of polarization of pump pulse. Stable distributed temperature and strain measurement were achieved experimentally. Finally, Chapter 7 concludes this thesis and proposes several topics of future work.

## **Chapter 2**

### **Multi-Channel Optical Pulse Train**

### **Generation Based on Parametric**

### **Process in Highly-Nonlinear Fiber**

A high-speed optical pulse train has wide applications. It can be used as an optical clock, for optical sampling, or to imprint optical data bits. Multi-channel optical pulse train generation has attracted great attention as it is essential for wavelength-division-multiplexing (WDM) transmission systems and optical sensor systems. The traditional method to generate high-speed pulse train is using a mode-locked laser, which is for a single channel and the tuning range of the wavelength is very limited. For WDM applications, it will require several expensive mode-locked lasers, which is not cost-effective. Fiber optical parametric process has been used in many applications in high-speed optical communication systems, since it can provide high gain over a wide bandwidth. Optical parametric process was used to realize optical amplifiers [55, 100, 101], wavelength converters [102], demultiplexers [103], and pulse source generation [64, 104–106]. Three WDM channel at 10-Gbit/s are amplified



## **2.1 Principle of Multi-Channel Optical Pulse Train Generation Through Parametric Process**

---

based on parametric gain in [100] and a 10-GHz pulse source with a pulse width of 6 ps was generated via higher order FWM in a saturated optical parametric amplifier (OPA) in [104]. In addition, wavelength tunable RZ pulse source with a full width at half maximum (FWHM) of 7 ps and repetition rate of 10-GHz was generated based on optical parametric process [105] and 14 channels 10-GHz short-pulses with pulsewidth of 4 ps were obtained through XPM and FWM in a nonlinear optical loop mirror [64]. Recently, a single channel 40-Gbit/s RZ pulse was generated in an OPA [106] and a 40-Gbit/s 1-to-40 multicasting was obtained in a wideband parametric amplifier [67].

In this chapter, multi-channel high-speed optical pulse train generation based on optical parametric process in HNLF over a wide bandwidth is demonstrated. Six-channel 80 GHz pulse train generation in an all-optical system was achieved experimentally. The extinction ratio (ER) of the amplified signal channels is more than 19 dB and it is larger than 30 dB for the generated idler channels. The waveforms of the generated pulse trains are monitored by an auto-correlator. The bit error rate (BER) measurements of the each channel was analyzed numerically in VPItransmissionMaker 7.0. In the back-to-back case, the power penalties of the generated pulse trains are less than 0.5 dB. This scheme can be applied to higher repetition rate beyond 100 GHz.

## **2.1 Principle of Multi-Channel Optical Pulse Train Generation Through Parametric Process**

For a single pump is used for parametric amplification, an intense pump light and a weak signal light are coupled into a piece of nonlinear fiber, the pump light loses photons as some are converted to signal wavelength and some are given to the idler wavelength. At the end of the nonlinear fiber, the signal light is amplified and an idler light is generated at a new wavelength through optical parametric process. The signal

## 2.1 Principle of Multi-Channel Optical Pulse Train Generation Through Parametric Process

---

and idler have nearly the same power when the pump power is large enough such that the converted photons are much more than the weak input signal. In the non-phase matching condition ( $\kappa \gg \gamma P_0$ ), amplification factor  $G_p$  (gain of input signal) is given by [1]

$$G_p \approx 1 + (2\gamma P_0 L)^2 \frac{\sin(\kappa L/2)^2}{(\kappa L/2)^2}, \quad (2.1)$$

where  $\gamma$  is nonlinear parameter of fiber,  $P_0$  is the pump power,  $\kappa = \Delta k_W + \Delta k_{NL} + \Delta k_M$  and  $L$  is the length of fiber. The amplification factor  $G_p$  is proportional to  $P_0^2$ . In the phase matching condition ( $\kappa=0$ ),  $G_p$  increases exponentially with  $P_0$  and can be written as [1]

$$G_p \approx \exp(2\gamma P_0 L)/4 \quad (2.2)$$

From above equations, it can be observed that efficient parametric process can be achieved if phase matching condition is satisfied. In other words, high parametric gain can be achieved in the phase matching condition ( $\kappa=0$ ), when  $\Delta k_M$  cancels  $\Delta k_W + \Delta k_{NL}$ . The 3 dB gain bandwidth  $\Delta\Omega_A$  of an OPA is given by [1]

$$\Delta\Omega_A = \frac{[(\pi/L)^2 + (\gamma P_0)^2]^{1/2}}{|\beta_2| \Omega_S}, \quad (2.3)$$

where  $\beta_2$  is the group velocity dispersion (GVD) coefficient and  $\Delta\Omega_S$  is the frequency shift between the pump and signal waves. If the pump wavelength is placed at  $\lambda_0$  of the fiber,  $\beta_2$  is close to zero and wide gain bandwidth can be achieved. Therefore, an OPA has maximum gain bandwidth  $\Delta\Omega_A$  when the pump is placed at dispersion zero wavelength  $\lambda_0$ . However,  $\Delta k_M$  is very small at  $\lambda_0$  and cannot cancel  $\Delta k_W + \Delta k_{NL}$ . Thus, the phase matching condition is not satisfied and the amplification factor  $G_p$  is not the maximum value. It can be seen that there is a tradeoff between  $G_p$  and

## 2.2 Experimental Results

---

$\Delta\Omega_A$ . In order to obtain large gain and wide bandwidth, the pump wavelength should be optimized.

As parametric process in optical fiber is an ultra-fast process, continuous wave (CW) light can be modulated by the pulsed pump in an OPA system. By coupling an intense pulsed pump light and a weak CW signal light into HNLF, the CW light is amplified when the pump pulse is “on” and has no gain when the pump pulse is “off”. Due to the high gain of OPA system, the ER of the amplified signal and the generated idler are high. The gain of signals and conversion efficiency of idlers are also affected by the walk-off between pulsed pump and signals/idlers. Furthermore, due to the wide bandwidth of OPA system, more than one channel pulse train can be generated at the same time. If N-channel CW lights and an intense pulsed pump are coupled into a piece of HNLF, the N-channel CWs are amplified by the pulsed pump and become pulse trains. At the same time, another N-channel pulse trains are generated at the converted idler wavelengths. The extinction ratios of the idler channels are larger than that of signal channels as the power of “0” is much smaller in the idler channels.

## 2.2 Experimental Results

### 2.2.1 Performance of the Optical Parametric Amplification

The Experimental setup of optical parametric amplification system is shown in Fig.2.1. A CW light was modulated by a phase modulation (PM) by a 10-Gbit/s pseudorandom binary sequences (PRBS) data and served as the pump of OPA system. By using PM, SBS effect can be suppressed and the pump power can be increased. Then the pump light was amplified by an EDFA, whose maximum output power is 3 W, and filtered by an optical bandpass filter (OBPF) with a 3 dB bandwidth of 0.9 nm to eliminate the ASE noise. Another CW light whose wavelength can tuned from 1543 nm to 1580

## 2.2 Experimental Results

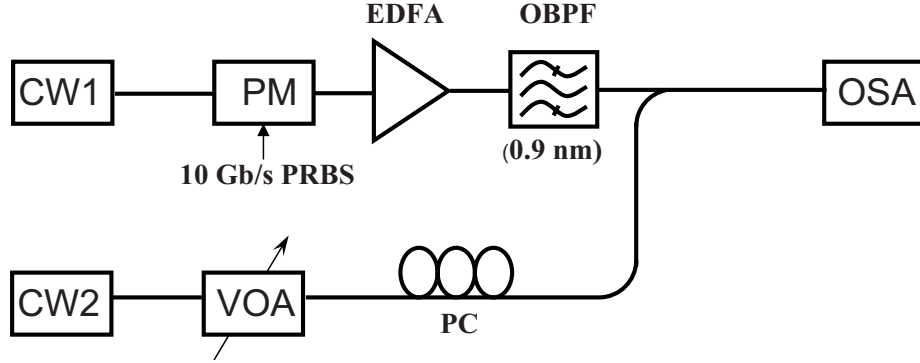


Figure 2.1: Experimental setup for measurement of optical parametric amplification system. PM: phase modulator. HNLF: highly nonlinear fiber.

TABLE 1  
HNLF PARAMETERS

Quantity	Value
Length	1 km
Zero dispersion wavelength $\lambda_0$	1560 nm
Dispersion slope $D_\lambda$	0.035 ps/km-nm <sup>2</sup>
Nonlinear Coefficient $\gamma$	11 W <sup>-1</sup> Km <sup>-1</sup>
Polarization Dependent Loss	0.1 dB

Table 2.1: Parameters of the HNLF used in the experiment.

## 2.2 Experimental Results

---

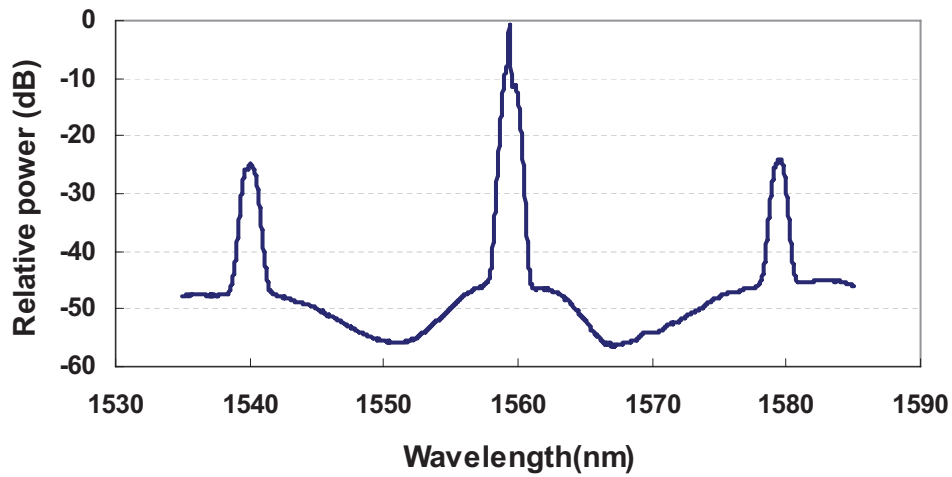


Figure 2.2: Optical spectrum when the pump and probe wavelengths are 1559.35 nm and 1540 nm, respectively. The pump power is 27-dBm.

nm was used as probe light. The maximum power of probe light is 10 dBm. Then the pump and probe waves were coupled into 1 km HNLF through a 99:1 coupler. Table 2.1 shows the parameters of the HNLF used in the experiment. The amplified signal and generated idler channels were monitored by an optical spectrum analyzer (OSA).

Fig.2.2 shows the optical spectrum when the pump and probe wavelengths are 1559.35 nm and 1540 nm, respectively. It is observed that the generated idler channel has almost the same power as the amplified probe channel. The noise at different wavelengths are amplified by various values, which indicates the gain bandwidth of the OPA system.

The performance of the optical parametric amplifier was obtained by utilizing an intense CW light (phase modulated by 10-Gbit/s PRBS data) as pump wave and a CW tunable laser as probe signal. The pump and probe waves were coupled into 1 km HNLF through a 99:1 coupler. Gain spectra at different pump wavelengths are shown in Fig.2.3. The optical power of the pump and signal coupled into the HNLF are 27 dBm and -25 dBm, respectively. The maximum gain is 32 dB for 1560 nm pump;

## 2.2 Experimental Results

---

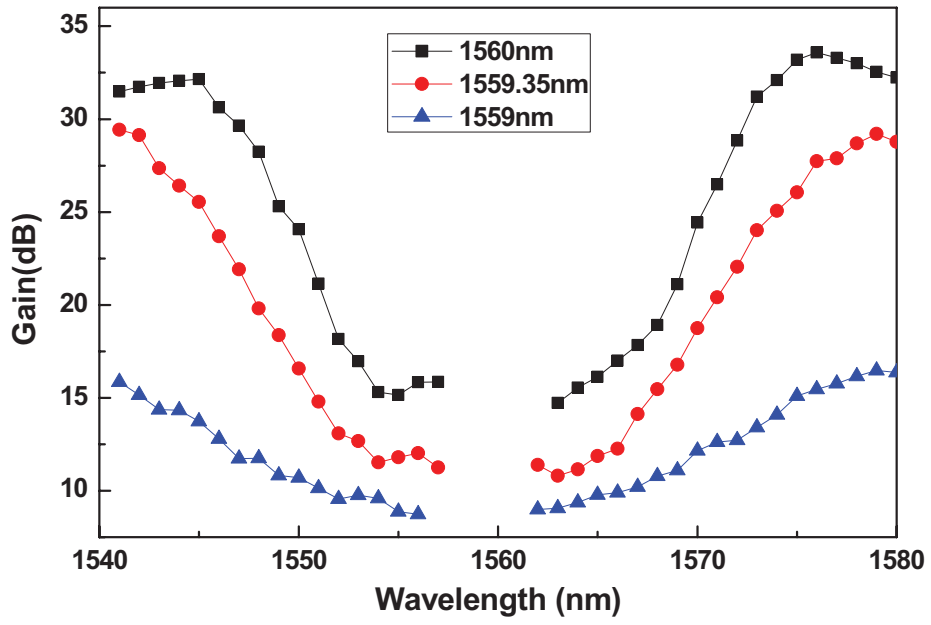


Figure 2.3: Gain spectra of the parametric amplifier. Pump wavelength is 1560 nm, 1559.35 nm and 1559 nm respectively. Pump power is 27-dBm and signal power coupled into the HNLF is -25-dBm.

## 2.2 Experimental Results

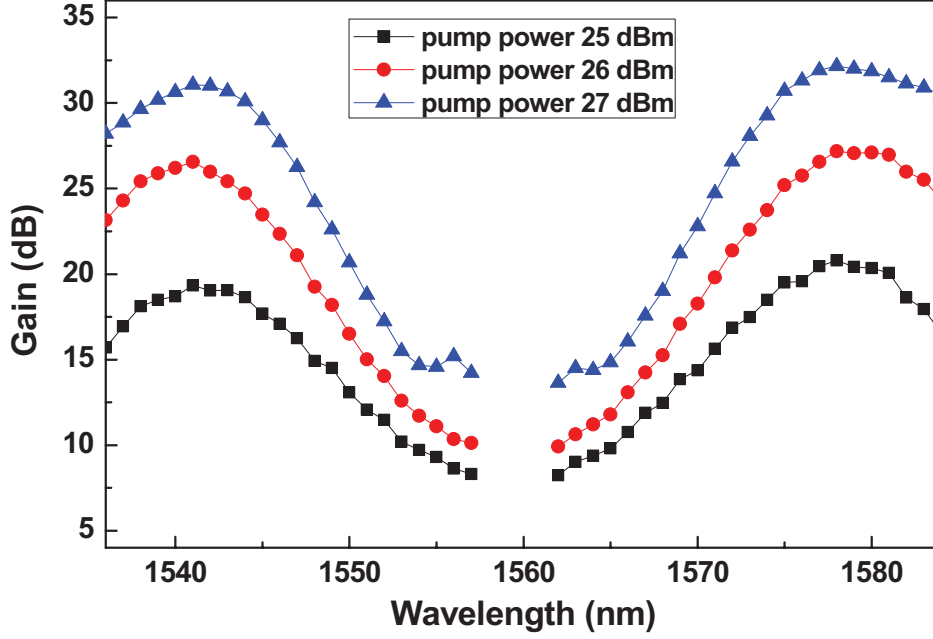


Figure 2.4: Gain spectra of parametric amplifier for pump power of 25 dBm, 26 dBm and 27 dBm. The pump wavelength is 1559.35 nm. Signal power coupled into the HNLF is -25 dBm.

however, the 3 dB gain bandwidth is only 7.5 nm. While the gain bandwidth is 13 nm when pump wavelength is 1559 nm, however, the maximum gain is only 12 dB. It is obvious that there is a tradeoff between  $G_p$  and  $\Delta\Omega_A$  in an OPA system. Considering both gain and gain bandwidth of OPA, 1559.35 nm is the optimal pump wavelength, at which 30 dB gain and 11 nm gain bandwidth can be achieved.

The gain spectra of the OPA with different pump powers are shown in Fig.2.4. An intense CW light at 1559.35 nm serves as the pump and a tunable laser with an input power of -25 dBm serves as probe signal. As the result of SRS effect, the gain at longer wavelength is larger than that at shorter wavelength by about 1 dB. Fig.2.4 shows that the OPA gain increases dramatically with pump power. The maximum gain is increased by 12 dB when the pump power increases from 25 dBm to 27 dBm.

## 2.2 Experimental Results

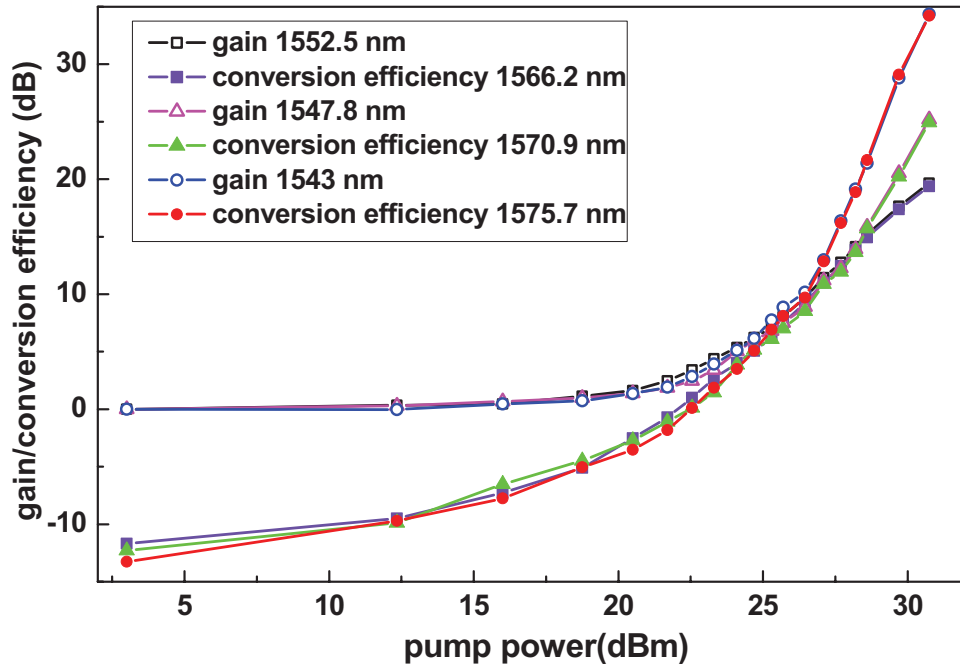


Figure 2.5: Gain of the input signal and conversion efficiency of the idler. Pump wavelength is 1559.35 nm.

However, if the pump power is too large, large noise will be introduced on the pump pulse and transferred to the signal and idler channels. Moreover, the signals with high gain will be degraded by the crosstalk between the channels.

Fig.2.5 shows the parametric gain of input signals and conversion efficiency of idlers as a function of pump power. Conversion efficiency is the power ratio between the output and input of OPA at the idler wavelengths. An intense CW pump placed at 1559.35 nm and three-channel signals, 1543 nm, 1547.8 nm and 1552.5 nm, were coupled into the HNLF. The input power of each signal channel is -25 dBm. From Fig.2.5, it can be observed that the power of the idler is almost the same as that of amplified signal as long as the pump power exceeds a critical value. The three-channel signals have different gains at high pump power; this is due to the bandwidth limitation of the OPA. At a 30 dBm pump power, the gain is more than 19 dB at 1552.5 nm and



## 2.2 Experimental Results

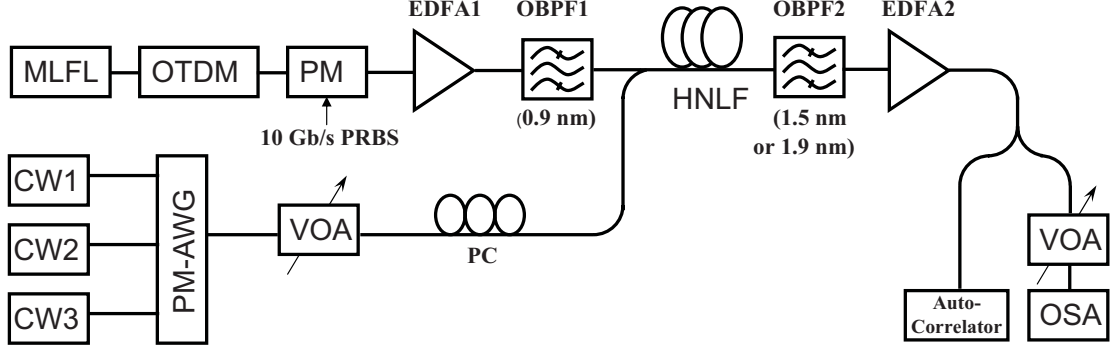


Figure 2.6: Experimental setup for multi-channel pulse generation. PM: phase modulator. HNLF: highly nonlinear fiber.

it is more than 32 dB when the signal is placed at 1543 nm, which is close to the center of gain spectrum.

### 2.2.2 6-Channel 80 GHz Optical Pulse Generation

The experimental setup of multi-channel pulse train generation is shown in Fig.2.6. A mode-locked fiber laser (MLFL), which was driven by a 10 GHz clock, provided a short pulse train with pulse width of 3.8 ps at a repetition rate of 10 GHz. After a 3-stage optical time-division-multiplexing (OTDM), the pump pulse with a repetition rate of 80 GHz was modulated by a phase modulation to suppress the stimulated Brillouin scattering (SBS). The phase modulator was synchronized to the pulses, so the phase changes did not happen within the pulse duration, thus it will not induce extra power penalty on the pump pulse. The 80 GHz pump pulse had an optical signal-to-noise ratio (OSNR) of 35 dB. Then the pump light was amplified by an EDFA, whose maximum output power is 3 W, and filtered by an optical bandpass filter (OBPF) with a 3 dB bandwidth of 0.9 nm to eliminate the ASE noise. Three-channel distributed feedback (DFB) lasers, with wavelength of 1543 nm, 1547.8 nm and 1552.5 nm respec-

## 2.2 Experimental Results

---

tively, were coupled into a polarization-maintaining arrayed waveguide grating (PM-AWG) and served as probe signals. Then the pump and probe waves were coupled into 1 km HNLF through a 99:1 coupler. A polarization controller (PC) aligned the polarization states of the probes matching with that of the pump. Fig.2.7(a) shows the dispersion of HNLF at different wavelengths. The dispersion slope is  $0.035 \text{ ps/km-nm}^2$ . The group delay of HNLF is shown in Fig.2.7(b). The walk-off can be obtained from the group delay. Group delays at pump (1559.35 nm) and signals (1543 nm, 1547.8 nm and 1552.5 nm) wavelengths are 0.78 ps, 1.48 ps, 0.3 ps and 0.01 ps, respectively. Thus the walk off between the pump (1559.35 nm) and the signals (1543 nm, 1547.8 nm and 1552.5 nm) are 0.7 ps, 0.48 ps and 0.77 ps, respectively. The walk-off between the pump and idlers are 2.22 ps, 4.54 ps and 7.55 ps, respectively. The powers of the CW probes were tuned by a variable optical attenuator to limit the crosstalk between the channels. C-band OBPF (1.5 nm) and L-band OBPF (1.95 nm) were used to filter out the signal and idler channels, respectively. The amplified signal and generated idler channels were monitored by an optical spectrum analyzer and an auto-correlator with a resolution of 5 fs.

An intense 80 GHz pulsed pump and the three-channel CW signals are coupled into the HNLF. The optical spectrum at output of the HNLF is shown in Fig.2.8(a). It can be observed that three optical channels at 1566.2 nm, 1570.9 nm and 1575.7 nm, which corresponding to the idler of the input signals, are generated. And the amplitudes of the probe and idler channels are nearly the same as the pump power exceeds the critical power of the OPA system. Fig.2.8(b) is the spectrum of the amplified signal which is filtered out by an OBPF and amplified by EDFA. It is shown that the signal is modulated by the pulsed pump at 80 GHz and the signals at lower frequencies are suppressed efficiently. As any noise of the pump pulse will transfer to the signal and idler channels, the quality of pump pulse is essential to the generated channels. At a high

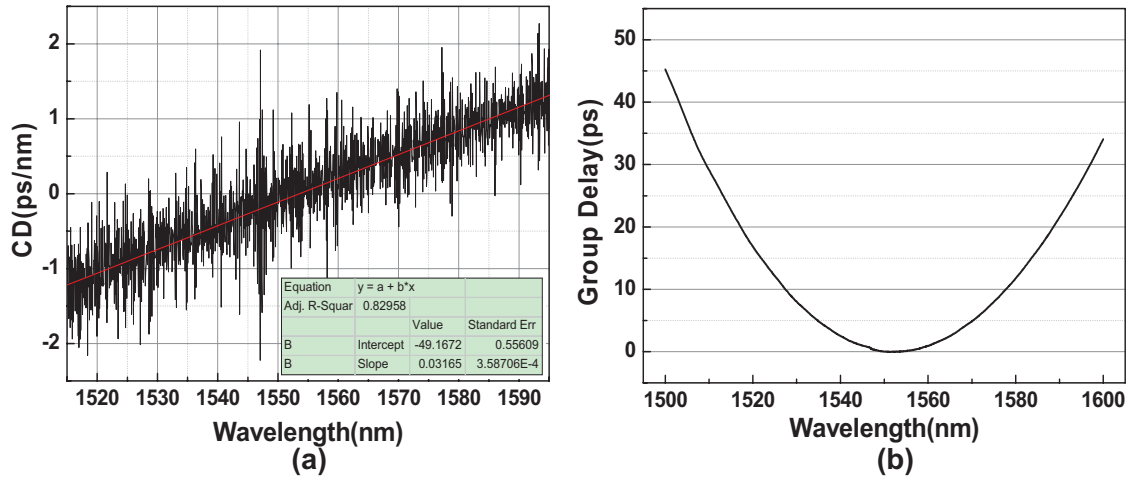


Figure 2.7: The (a) dispersion and (b) group delay of highly-nonlinear fiber as a function of wavelength.

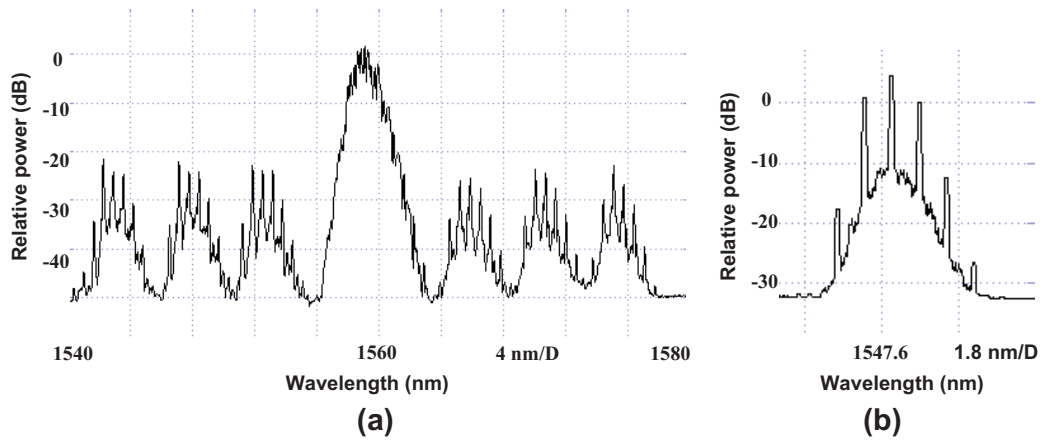


Figure 2.8: Optical spectra (a) after the HNLF with three input signals (b) filtered out and amplified signal at 1547.8 nm. The pump is multiplexed to 80 GHz and amplified to 20 dBm.

## 2.2 Experimental Results

---

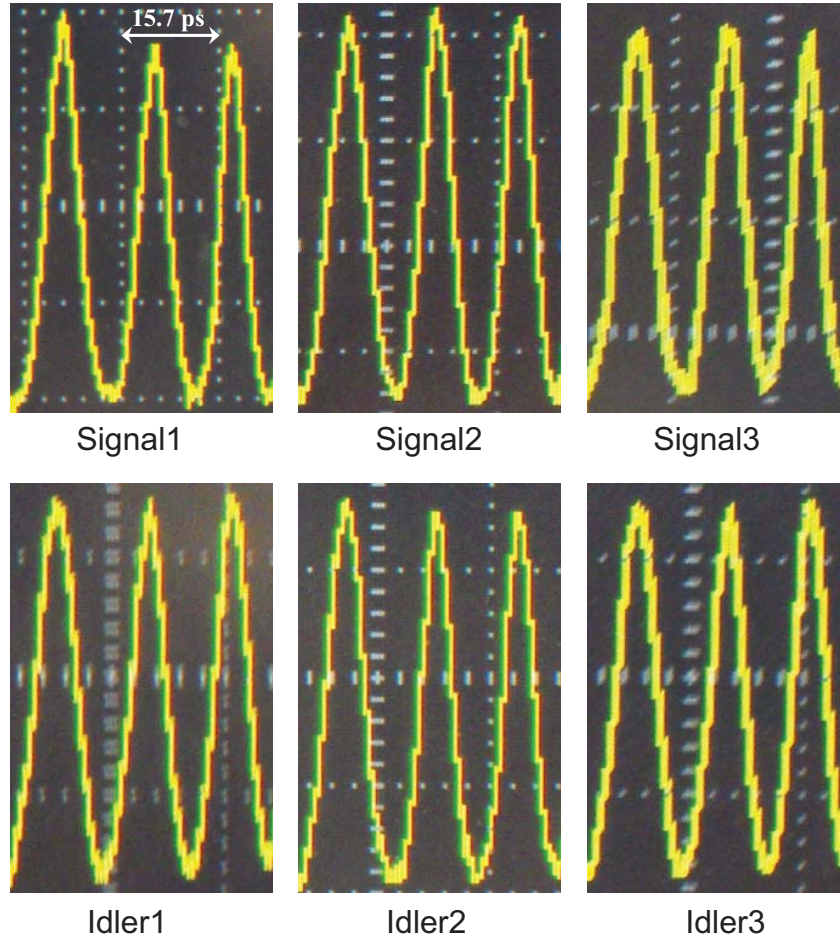


Figure 2.9: Measured 80-GHz waveforms at signal and idler wavelengths by an auto-correlator.

pump power, the pump pulse experience SPM, which broaden the optical spectrum of pump pulse and induces timing jitter to the generated channels. Besides, the number of generated channels is limited by the gain bandwidth of the OPA system, which is determined by the properties of the nonlinear medium.

The waveforms of the generated 80 GHz optical pulse trains are measured by an auto-correlator with a resolution of 5 fs. Fig.2.9 shows the measurement pulses at signal and idler wavelengths. The optical pulses were obtained at an average pump power of 26 dBm (the corresponding peak power is about 30 dBm). For pulsed pump,

## 2.3 Simulation Results of BER Performance

---

the ER of signals and idlers are affected by the walk-off effect. In our OPA system, the walk-off between pump and signals are less than 0.8 ps. Thus, the signal channels can be amplified efficiently through parametric process. According to Fig.2.5, ER of the signal channels is larger than 19 dB and it is more than 30 dB for idler channels. In Fig.2.9, by using a scale factor of 6.3 ps/ms, the measured repetition period of the pulses is 12.5 ps. The full width at half maximum (FWHM) of the pump pulse as well as the generated 6-channel 80 GHz pulse trains are shown in Fig. 2.10. By using a shape factor 0.71, the FWHM of the generated pulses is about 3.7 ps. The time-bandwidth product of the generated pulses is 0.65. As the peak power of the pump pulse is very large, XPM occurs accompany with the parametric process. And the signal and idler pulses are compressed by XPM induced chirp. The compression factor depends on the pulse width and peak power of the pump pulse as well as the walk-off value. The pulse width is wide at 1575.7 nm, where the walk-off value is large.

## 2.3 Simulation Results of BER Performance

In order to verify the qualities of the optical pulse trains generated in the OPA system, numerical analysis of BER at each generated channel was performed in the simulation tool VPItransmissionMaker 7.0. In the simulation, the pump wave was a 3.8 ps short pulse with a repetition rate of 10 GHz and then multiplexed to 80 GHz, which was the same as that in the experiment. It was amplified to 26 dBm by an EDFA and filtered by an OBPF with a 3 dB bandwidth of 0.9 nm. Three channels CWs at wavelength of 1543 nm, 1547.8 nm and 1552.5 nm with input power of -25 dBm served as probe signals. The parameters of the HNLF are the same as that shown in Table 2.1. At the output of the HNLF, the signal channels were amplified and three idler channels are

## 2.3 Simulation Results of BER Performance

---

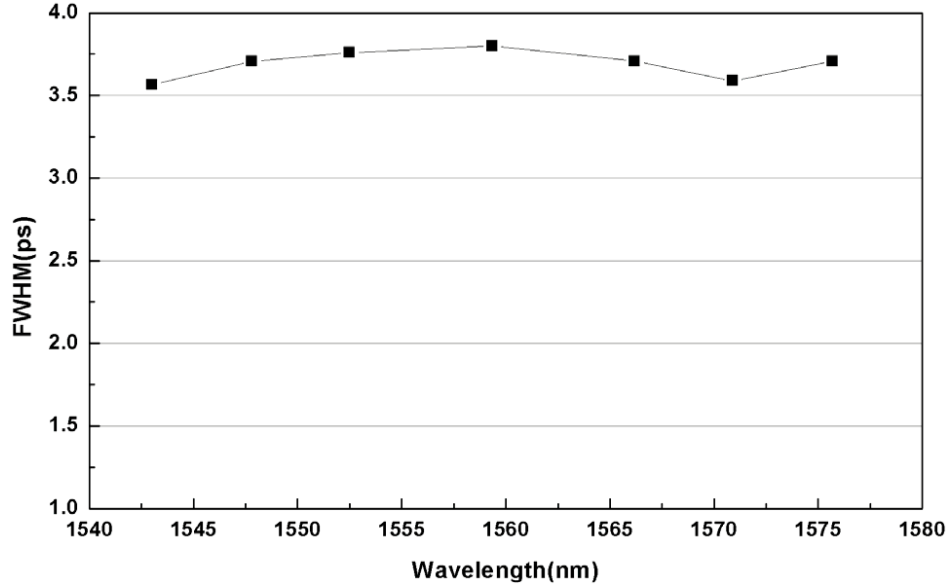


Figure 2.10: FWHM of the signal channels, idler channels and pump pulse.

generated at the same time, shown in Fig.2.11. Each generated channel was filtered out by an OBPF with a 3 dB bandwidth of 1.92 nm and modulated by 80-Gbit/s PRBS sequences.

Fig.2.12(a) shows the BER performance of the generated optical pulses in back-to-back case. The performance of 3.8 ps 80 GHz pulse is shown for comparison. It is observed that the idler channels (1566.2 nm, 1570.9 nm and 1575.7 nm) have negative power penalties. And the power penalties of the signal channels (1543 nm, 1547.8 nm and 1552.5 nm) are less than 0.5 dB (at  $10^{-9}$  BER). This is due to the fact that the idler channels have higher extinction ratios. Fig.2.12(b) shows the BER measurements after transmission through 200 m single mode fiber (SMF). We notice that the quality of signal channels are improved when they transmit through 200 m SMF.

The idler channels are generated and signal channels are amplified through parametric process. At the same time, the signal and idler pulses are compressed by XPM

### 2.3 Simulation Results of BER Performance

---

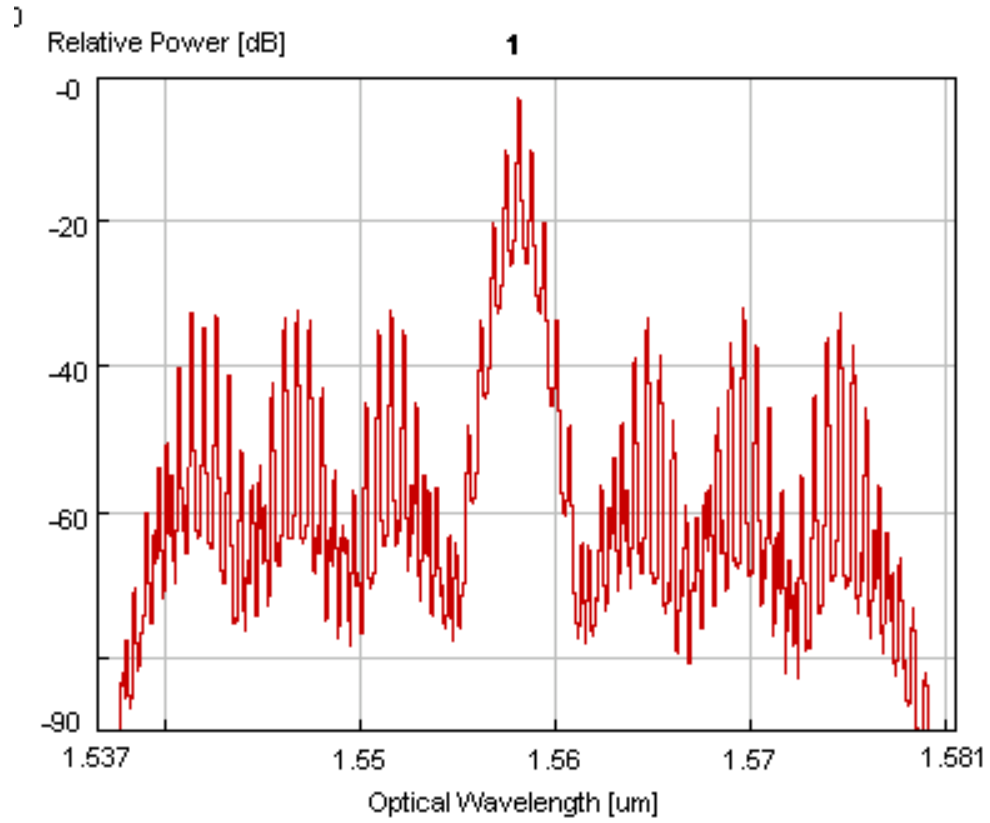


Figure 2.11: Simulated optical spectra at the output of HNLF. The pump is 80 GHz pulse with an average power of 20 dBm.

### 2.3 Simulation Results of BER Performance

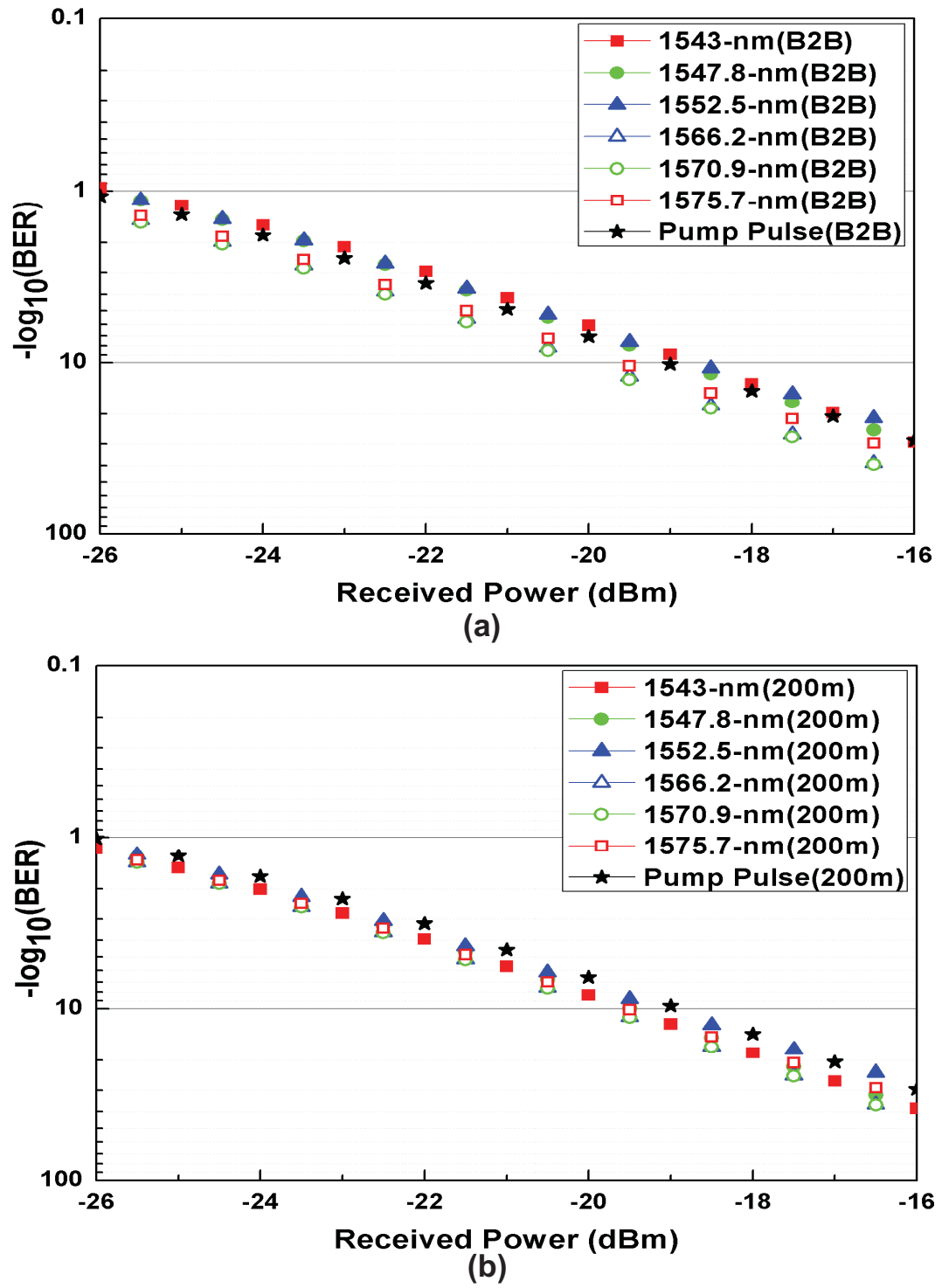


Figure 2.12: BER measurement as a function of received power for signal and idler channels (a) back-to-back (b) after 200 m transmission. The BER of 3.8 ps pulse is shown for comparison.



### 2.3 Simulation Results of BER Performance

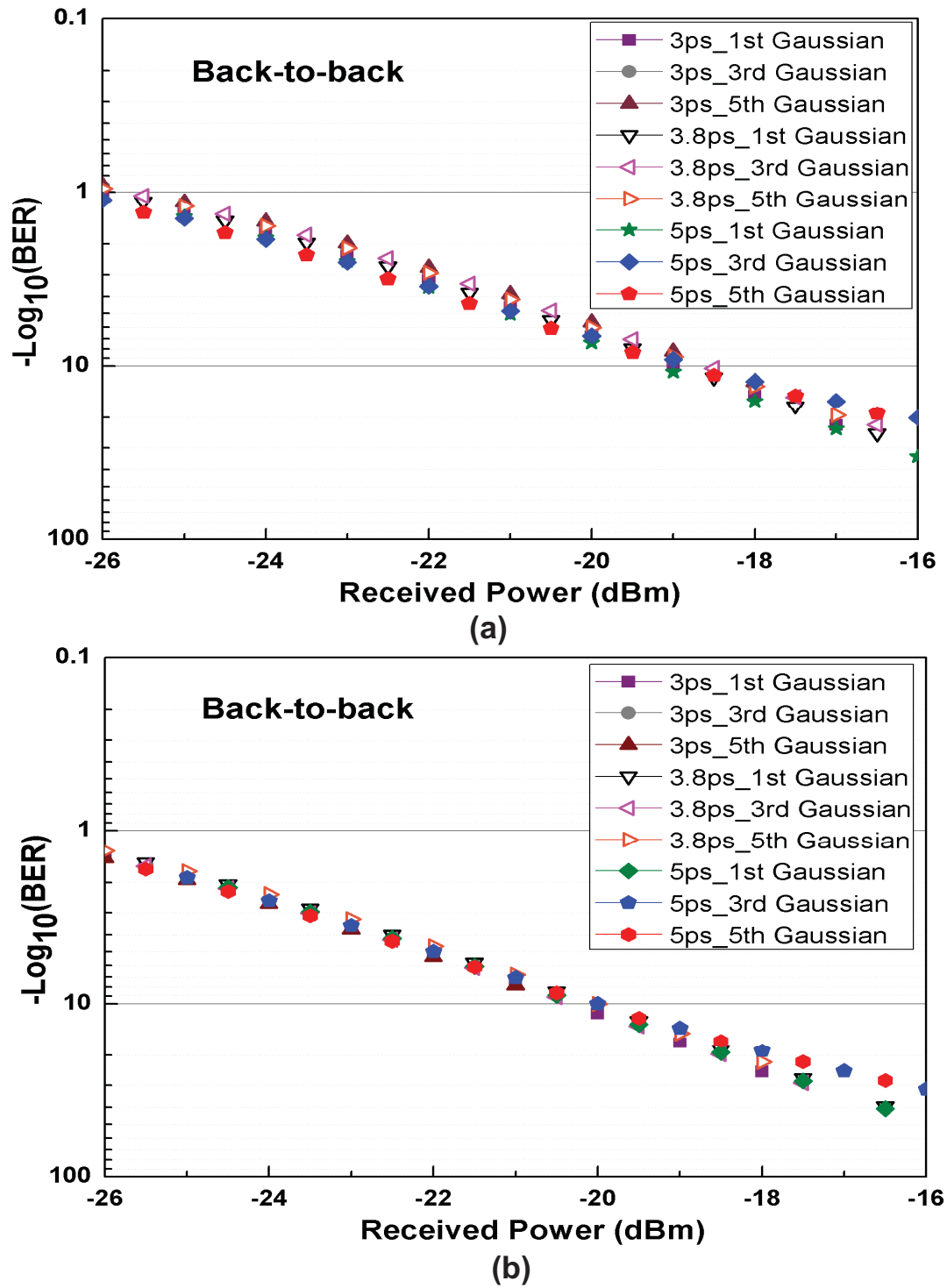


Figure 2.13: BER measurement as a function of received power for (a) 1547.8 nm and (b) 1570.9 nm. In back-to-back case.

### 2.3 Simulation Results of BER Performance

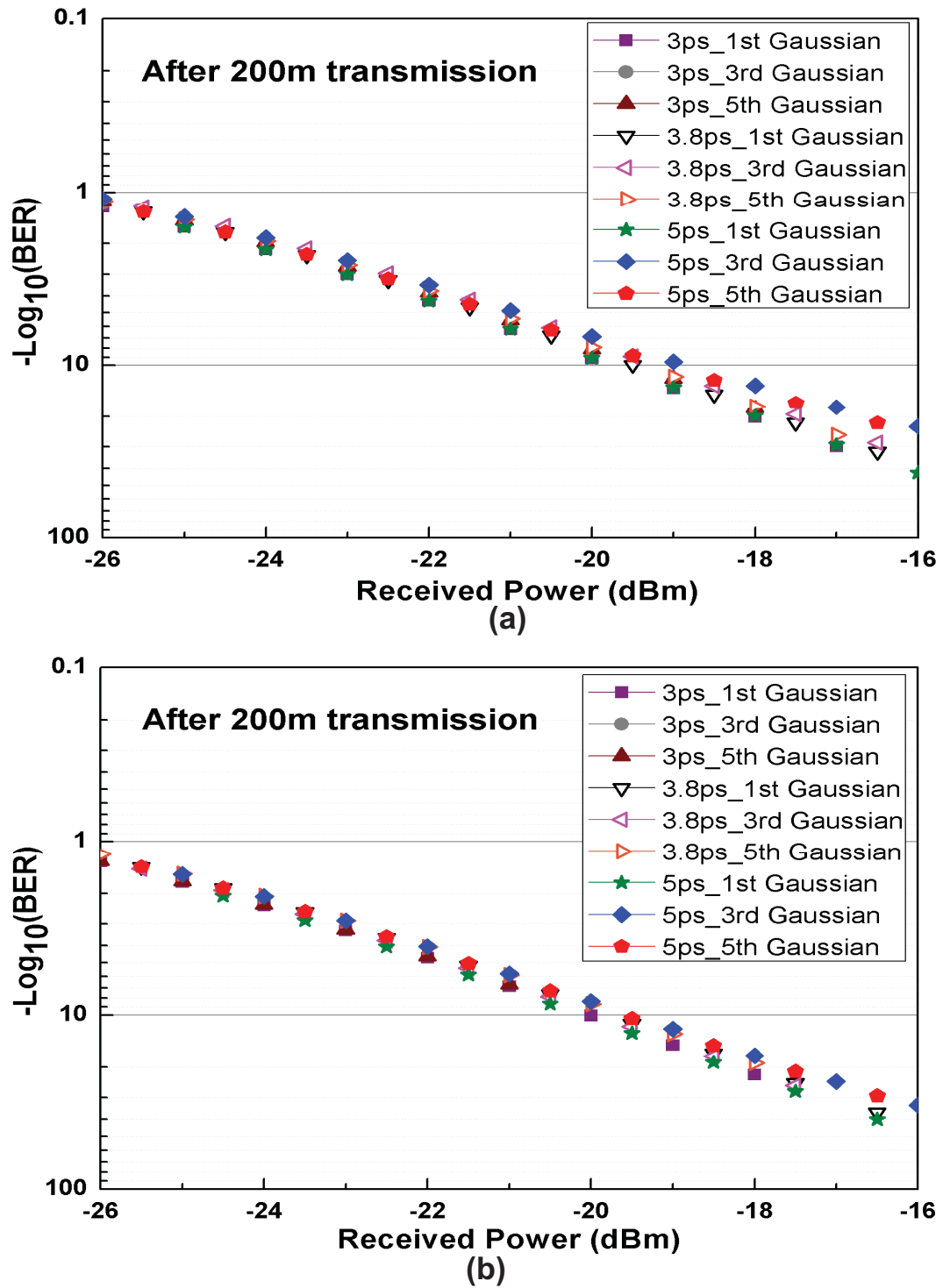


Figure 2.14: BER measurement as a function of received power for (a) 1547.8 nm and (b) 1570.9 nm. After 200 m transmission.

## 2.4 Conclusions

---

induced chirp. The compression factor and pulse quality depend on the pulse width and peak power of the pump pulse. Therefore, the quality of pump pulse is essential to the generated channels. Fig.2.13 shows back-to-back BER performances at 1547.8 nm (one of signal channels) and 1570.9 nm (one of idler channels) when pump pulses with different shapes and pulse widths are applied. First-, third-, and fifth-order Gaussian pulse with FWHM of 3 ps, 3.8 ps and 5 ps were utilized as the pump pulses. It is observed that the power penalties are less than 0.5 dB when different pump pulses are used.

Fig.2.14 shows BER after 200 m transmission at two of the generated channels (1547.8 nm and 1570.9 nm) when different pump pulses are applied. The power penalties are about 1 dB for different pulses. Therefore, it can be deduced that the generated optical short pulses have the similar performance as the pump pulse. Besides, they are not affected much by the slight changes of shape and pulse width of the pump pulses. It is noticed that the BER performance of the two channels are different. This is due to the walk-off effect and extinction ratio are different for the channels.

## 2.4 Conclusions

It is experimentally demonstrated that 80 GHz 6-channel pulse source can be generated based on fiber optical parametric process in HNLF using a pulsed pump and 3-channel CW probe signals. The wavelength of pump pulse is optimized to obtain large gain and wide gain bandwidth. Multi-channel optical pulse trains with high ER are generated. The BER of amplified signal and generated idler channels are analyzed numerically using VPItransmissionMaker 7.0. The power penalties of the generated optical pulses are less than 0.5 dB in back-to-back case. The simulation results also proved that the generated short pulses have the similar performance when pump pulses with slightly

## 2.4 Conclusions

---

different shapes and pulse width are utilized. In our experiment, the number of generated channels is limited by the wavelength of the tunable lasers. More channels of pulse source can be obtained if the lasers at the required wavelengths are available. Note that this scheme can be applied to higher repetition rate beyond 100 GHz, and it can be expanded to multicasting if the pump is modulated.

## **Chapter 3**

# **Broadband Multi-Wavelength Light Source Generation Using a Single Phase Modulator in a Loop**

Multi-wavelength optical sources are required for dense wavelength division multiplexing (DWDM) and coherent optical frequency-division multiplexing (CO-OFDM) systems [108]. Broadband multi-wavelength light source with high coherence, low noise and equal spacing attracts a lot of interests. Various methods have been reported on multi-channel light source generation. Phase modulator (PM), which can generate carriers with precise channel spacing, has been widely used to generate frequency comb [109–111]. However, it is difficult to achieve flat spectrum using a single PM. Therefore, intensity modulators were utilized to flatten the comb spectrum. Besides, the number of generated channels is limited by the drive voltage of PM. Several cascaded PMs were used in [112] to obtain higher modulation index and more optical channels. By optimizing the driving condition of a dual-drive Mach-Zehnder modulator (MZM), frequency comb with good spectral flatness was generated [113]. How-

### 3.1 Principle of Multi-Wavelength Light Source Generation Using a Single Phase Modulator in a Loop

---

ever, the number of generated channels is limited by the drive voltage of MZM. Optical frequency comb can also be generated through supercontinuum [114, 115]. Over 130 channels have been generated using a single PM followed by an intensity modulator and nonlinear medium [115]. However, high optical power is required in this method. Another method of generating multi-wavelength optical source is utilizing serrodyne modulation [116, 117]. However, the spectrum of the generated source is not flat and can not serve as source in WDM systems.

In this chapter, we propose a new scheme that yields broadband multi-wavelength source using a single PM in a loop. The loop structure was designed to broaden the spectrum and increase the number of light source. Neither high optical power nor large drive voltage is employed in this method. Generation of 125-channel light source with more than 30 dB optical signal-to-noise ratio (OSNR) is demonstrated experimentally.

### 3.1 Principle of Multi-Wavelength Light Source Generation Using a Single Phase Modulator in a Loop

The system setup is shown in Figure 3.1. The loop consists of two couplers (10:90 and 1:99), a phase modulator (PM), a polarization controller (PC) and a tunable optical delay line. The PC was inserted into the loop to maintain the polarization state of the loop. And the optical delay line in the loop was tuned to ensure that the phase modulator is in resonance with the loop. Suppose that the input continuous-wave (CW) is given by

$$E_{in}(t) = \exp(j\omega_c t), \quad (3.1)$$

the electrical field of the output of single PM can be expressed as

$$E_{out}(t) = e^{j\omega_c t} e^{j\frac{\pi}{2}\beta \sin(\omega_m t)}, \quad (3.2)$$

### 3.1 Principle of Multi-Wavelength Light Source Generation Using a Single Phase Modulator in a Loop

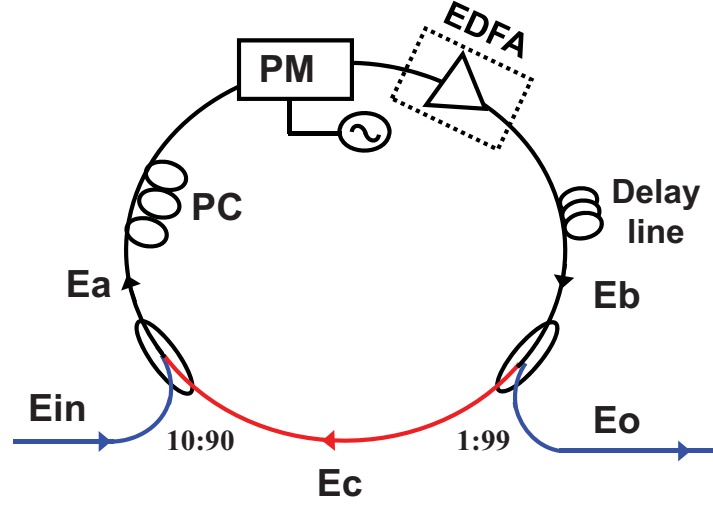


Figure 3.1: Experimental setup for multi-wavelength light source generation in a Loop.

where  $\omega_c$  and  $\omega_m$  are angular frequency of carrier and modulation frequency,  $\beta$  is electrical voltage normalized by the half-wavelength drive voltage,  $V_\pi$ , of PM. The Fourier transform of  $E_{out}$  consists of  $\omega_c \pm n\omega_m$ , and the amplitude of each component is governed by Bessel function  $J_n(\pi\beta/2)$ . Therefore, large drive voltage provides wider bandwidth and more comb channels [111]. However, the amplitude of each component is not the same.

In the proposed loop structure, the lights which go through PM different times are coupled together. At time  $t$ , the relation between various electric fields is

$$E_0(t) = \sqrt{1 - k_2} E_b(t) e^{-j\pi/2}, \quad (3.3)$$

$$E_a(t) = \sqrt{1 - k_1} E_{in}(t) e^{-j\pi/2} + \sqrt{k_1} E_c(t), \quad (3.4)$$

$$E_b(t) = \sqrt{\alpha} e^{-j\beta \sin(\omega_m t)} E_a(t - T_1), \quad (3.5)$$

$$E_c(t) = \sqrt{k_2} E_b(t - T_2), \quad (3.6)$$

### 3.1 Principle of Multi-Wavelength Light Source Generation Using a Single Phase Modulator in a Loop

---

where  $E_0(t)$ ,  $E_a(t)$ ,  $E_b(t)$  and  $E_c(t)$  are the electrical fields shown in Fig. ??;  $k_1$  and  $k_2$  are power coupling coefficient of the couplers;  $T_1$  and  $T_2$  are time delay of left and right half loop, respectively. After  $N$  circulations of the light through the loop, the output electric field is given by

$$E_0(t) = -\sqrt{1-k_1}\sqrt{1-k_2}\sqrt{\alpha} \sum_{n=0}^N (\sqrt{k_1}\sqrt{k_2}\sqrt{\alpha})^n e^{-j\beta F_n(\omega_m t)} E_{in}(t - T_1 - iT_1 - iT_2), \quad (3.7)$$

where  $F_n(\omega_m t) = \sum_{i=0}^n \sin \omega_m [t - i(T_1 + T_2)]$ . If the loop length is tuned such that  $\omega_m(T_1 + T_2) = 2\pi$ , the phase modulator is in resonance with the loop and phase shift for  $N$  circulations can be give by

$$\beta F_n(\omega_m t) = \beta n \sin(\omega_m t). \quad (3.8)$$

$\sqrt{k_1}\sqrt{k_2}\sqrt{\alpha}$  is the round-trip loop gain. If the loop gain equals to unity, the output electric field is given by

$$E_0(t) = -\sqrt{1-k_1}\sqrt{1-k_2}\sqrt{\alpha} E_{in}(t - T_1) \sum_{n=0}^N e^{-j\beta n \sin(\omega_m t)}. \quad (3.9)$$

In this condition, the Fourier transform of  $E_0(t)$  consists of  $\omega_c \pm n\omega_m$ , and the amplitude of each component is given by

$$A_k = \sum_{n=0}^{\infty} J_n(\pi\beta/2) \quad (3.10)$$

Therefore, the components at various frequencies have the same amplitude. The generated comb spectrum is much wide although only one PM with relative small drive voltage is applied. This method needs neither high optical power nor large drive voltage. The channel spacing can be tuned by changing the electrical driving signal of PM. The tunable optical delay line in the loop should be adjusted such that PM is in resonance with the loop.



## 3.2 Simulation Results

---

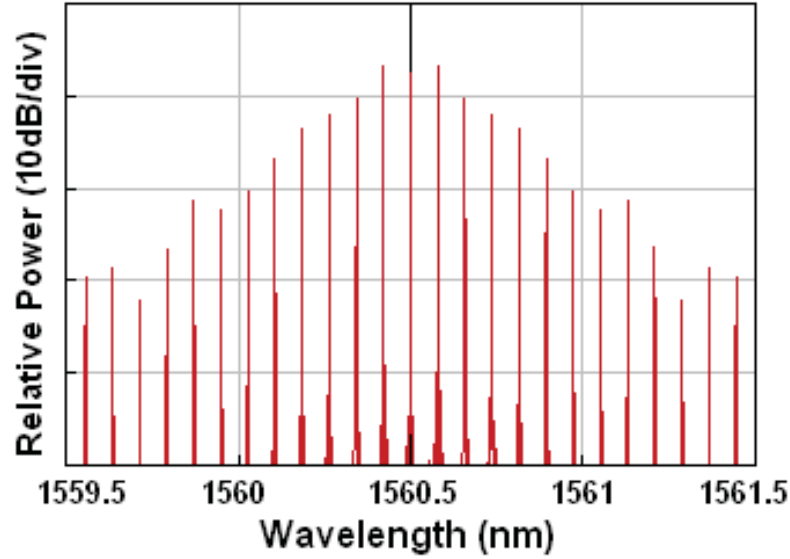


Figure 3.2: Simulated optical spectrum generated by single PM in a loop structure. No EDFA in the loop.

## 3.2 Simulation Results

The simulated results were obtained in VPItransmissionMaker 7.0. A continuous wave at 1560.5 nm was coupled into the loop through a coupler (10:90). A PM, whose  $V_\pi$  is 5 V, was driven by an electrical clock with a repetition frequency of 10 GHz. The generated frequency comb is coupled out through the 1% port of a 99:1 coupler.

### 3.2.1 Single PM in a Loop Structure without EDFA

Fig. 3.2 shows the simulated optical spectrum generated by a single PM in loop structure without EDFA. It can be observed that the amplitude of the high-order components decrease dramatically. This is due to the loss of phase modulator and fiber loop. However, compared with the optical spectrum generated by a single phase modulator, more channels of laser source were generated by utilizing the loop structure.

### 3.3 Experimental Results

---

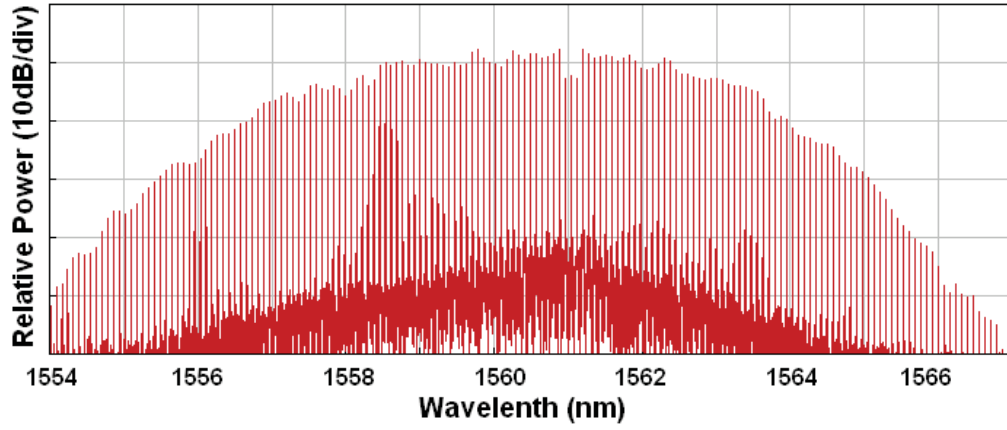


Figure 3.3: Simulated optical spectrum generated by single PM in an amplified loop. With EDFA in the loop.

#### 3.2.2 Single PM in an Amplified Loop

Fig. 3.3 shows the simulated optical spectrum of the generated optical source in an amplified loop with a single PM. More than 125 channels optical laser source were generated by utilizing a single PM in an amplified loop. Optical attenuator was tuned such that the losses of loop were compensated EDFA in the loop. Fig. 3.4 is the detailed optical spectrum around 1562 nm. It can be observed that the signal-to-noise ratio (SNR) of the optical source is more than 30 dB.

### 3.3 Experimental Results

A CW light at 1560.5 nm was coupled into the loop through a coupler (10:90). The optical power coupled into the loop is 0 dBm. A PM,  $V_\pi$  is 5 V, was driven by an electrical clock with a repetition frequency of 10 GHz and an amplitude of 8 V. A polarization controller (PC) is used to optimize the polarization state of the loop and it can be removed if polarization maintaining fiber is used in the loop. A tunable optical

### 3.3 Experimental Results

---

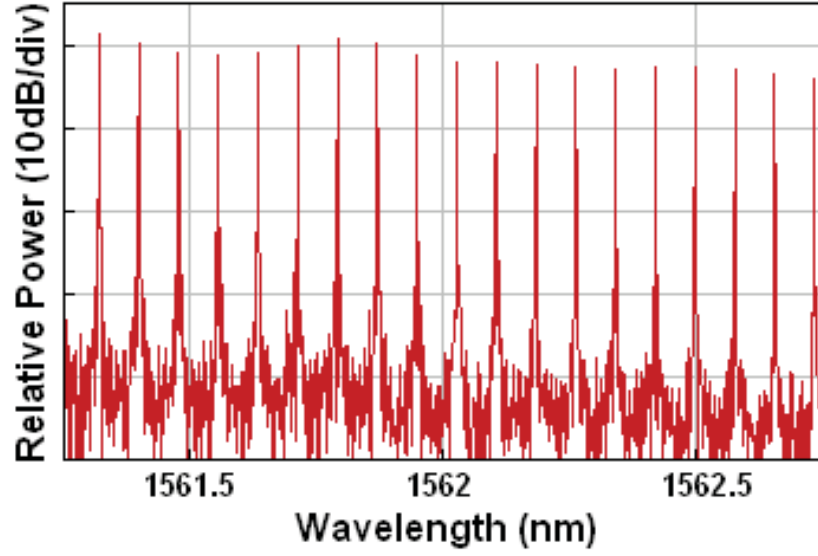


Figure 3.4: Detailed optical spectrum at 1562 nm.

delay line were tuned to adjust the round-trip length of the loop and ensure that the phase modulator is in resonance with the loop. More than 125 channels optical laser sources were generated in an amplified loop with a single PM.

#### 3.3.1 Single PM in a Loop Structure without EDFA

Fig. 3.5 shows the measured optical spectrum (0.01 nm resolution) generated by a single PM in loop structure without EDFA. The amplitude of the high-order components decrease dramatically, which coincides with the simulation results. Compared with the optical spectrum generated by a single PM, more laser channels were generated by utilizing the loop structure with a PM.

### 3.3 Experimental Results

---

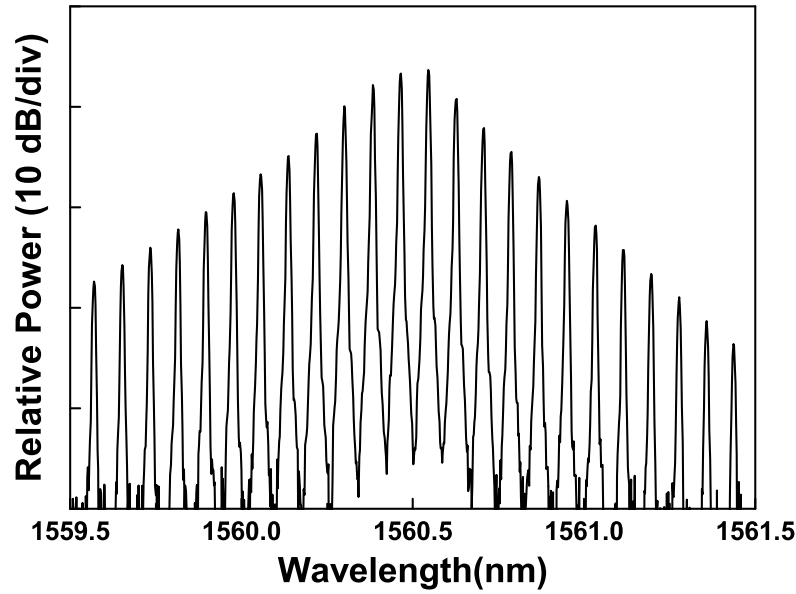


Figure 3.5: Measured optical spectrum generated by single PM in a loop structure. No EDFA in the loop.

#### 3.3.2 Single PM in an Amplified Loop

Fig. 3.6 shows the measured (0.01 nm resolution) optical spectrum of the generated optical source in the loop structure with EDFA. Optical attenuator was tuned such that the total round-trip gain is around 1. More than 125 channels optical laser sources were generated by utilizing a single PM in an amplified loop. The envelope of the generated spectrum is limited by the gain bandwidth of loop. Besides, the number of generated lasing wavelengths is also limited by the length of loop. The coherence of the lights decreases when propagating through the fiber. In our setup, the round-trip length is around 10 m. If the amplification medium can be improved, more channels of laser sources can be generated.

Fig. 3.7 is the detailed optical spectrum around 1562 nm. The signal-to-noise ratio of the generated laser source is more than 30 dB.

The channel spacing of generated frequency comb can be tuned by changing the

### 3.3 Experimental Results

---

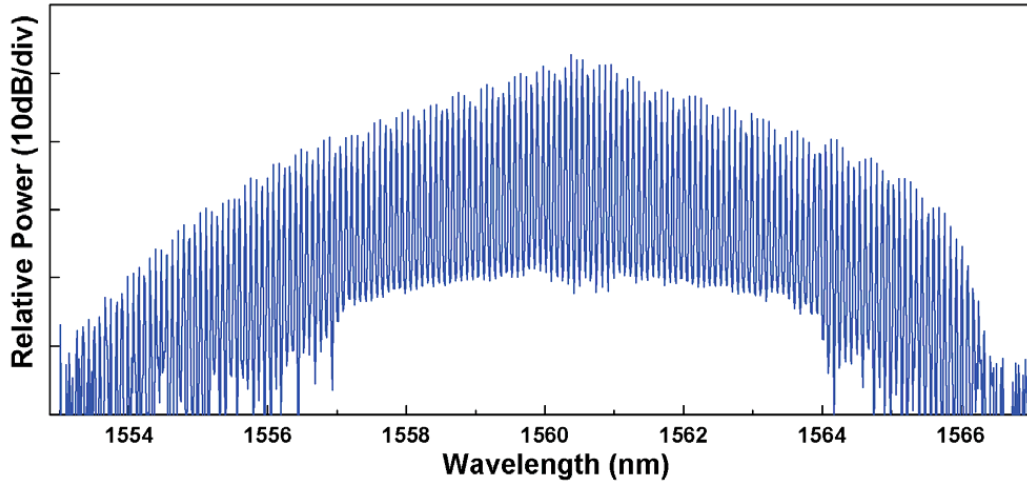


Figure 3.6: Measured optical spectrum generated by single PM in an amplified loop.  
With EDFA in the loop.

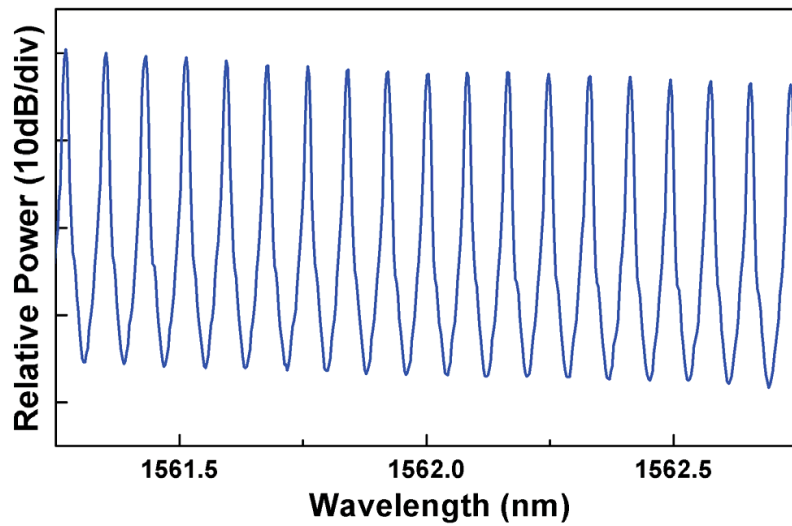


Figure 3.7: Measured detailed optical spectrum at 1562 nm.

### 3.3 Experimental Results

---

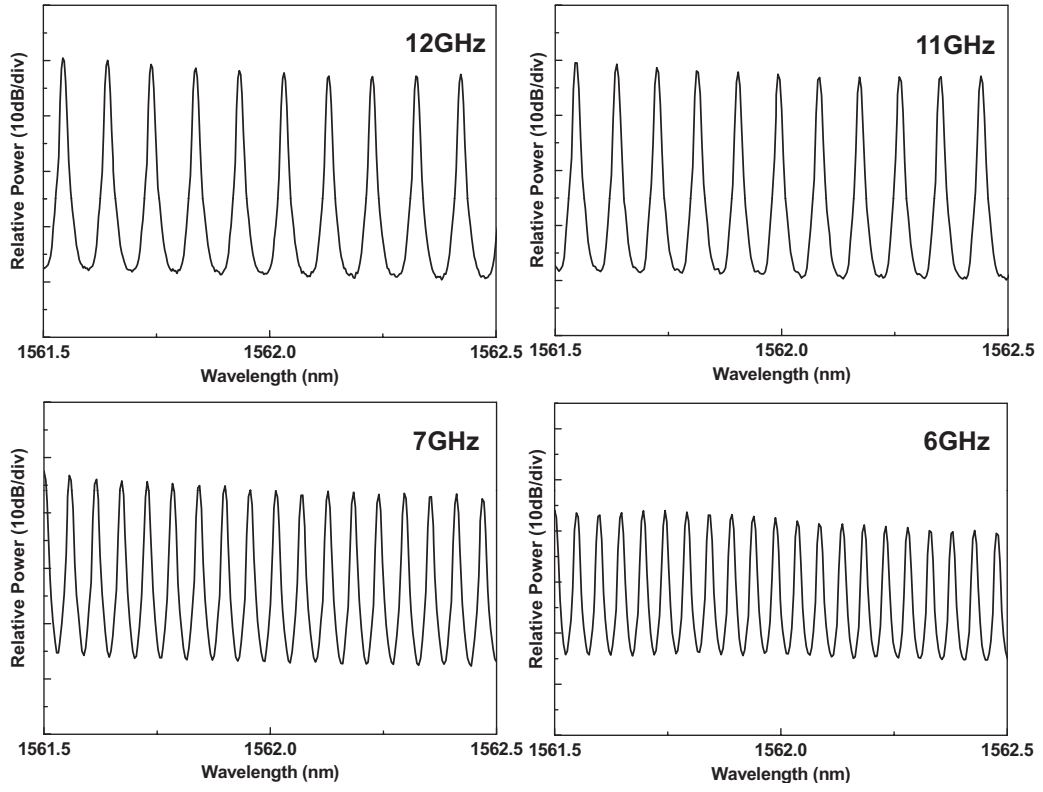


Figure 3.8: Measured optical spectra when the PM driven by clocks with different repetition rates.

### 3.4 Conclusions

---

repetition rate of electrical driving signal of phase modulator. Fig. 3.8 shows the optical spectra when the PM driven by clocks with different repetition rates (from 6 GHz to 12 GHz). The mode interval increases linearly with the repetition rate of clock signal. However, the envelopes of the optical spectra in high frequencies are not as flat as that in low frequencies. In other words, the 3 dB bandwidth of the generated frequency comb decreases as the repetition rate of driven clock decreases. This is due to the fact that the light driven by low RF frequency should go through more rounds in the loop to obtain a certain wavelength shift. While, the coherence decreases as the light goes through the fiber loop. Therefore, the bandwidth of generated frequency comb is reduced as the RF frequency decreases.

In our setup, 10:90 and 1:99 couplers were used to make a loop structure. It is found that other kind of couplers can also be utilized, as long as the losses in the loop are compensated by the gain of EDFA. Besides, in order to get a flat optical spectrum, the gain of EDFA should be optimized when the power of input CW changes.

### 3.4 Conclusions

The proposed scheme yields broadband multi-wavelength source using a single PM in an amplified loop. The loop length, gain and polarization state were tuned to obtain broad optical spectrum and more channels of light sources. Generation of 125-channel light source with more than 30 dB optical signal-to-noise ratio is demonstrated experimentally. Neither high optical power nor large drive voltage is employed in this method.

## Chapter 4

# CD-Insensitive PMD Monitoring Based on RF Power Measurement

The introduction of  $\geq 40$ -Gbit/s transmission links increases the deleterious impact on data channels due to fiber impairments, such as chromatic dispersion (CD), polarization mode dispersion (PMD) and nonlinearities. Polarization-mode dispersion is one of important impairments in high-speed optical transmission systems. As differential-group-delay (DGD), which is also known as first-order polarization-mode dispersion, is a stochastic process and it accumulates along fiber span [118, 119], dynamic PMD monitoring is required to enable a high-speed optical transmission system with high stability and flexibility.

Several techniques have been proposed on PMD monitoring in optical transmission systems. A technique was reported to monitor the PMD by measuring the phase difference between the two optical frequency components for the two orthogonal principal states of polarization (PSPs) [125]. However, polarization tracking is required to obtain the PSPs and the phase difference. By measuring the degree of polarization (DOP) of received signal, the degradation induced by PMD can be esti-



#### 4. CD-Insensitive PMD Monitoring Based on RF Power Measurement

---

mated [123, 124]. This method depends on the pulse width of the signal and the DGD monitoring range is small for short pulses. The RF tone power varies as a function of PMD and was proposed to monitor PMD values [120–122]. However, RF tone power is also affected by chromatic dispersion. Thus CD-insensitive PMD monitoring techniques are demanded. Eye diagram of optical signal reveals the affect of PMD and was used on PMD monitoring [126]. However, the measurement sensitivity is limited.

We propose a technique of CD-insensitive PMD monitoring base on RF power measurement utilizing fiber Bragg grating (FBG) filter. In high-speed ( $>10$  GSymbol/s) transmission systems, a narrow band FBG notch filter filters out the optical components 10-GHz off the carrier in one sideband. 10-GHz RF tone power is then generated by beating of the carrier with the other sideband, which varies with PMD but is insensitive to CD. As the 10-GHz RF tone is used as monitoring signal, compared to clock tone monitoring technique, the PMD measurement range is increased to 50 ps while the requirement of the bandwidth of photodetector (PD) is reduced to 10 GHz. The proposed method has following advantages: 1) transparent to modulation format; 2) wide measurement range (the DGD measurement range is 0~50 ps); 3) photoreceiver with low bandwidth (10 GHz) is used. Numerical simulation results of CD-insensitive PMD measurement for different modulation formats (DPSK, DQPSK and Duobinary) in 40-Gbit/s systems are shown. The effects of bandwidth of FBG notch filter on the dynamic range of DGD measurement results for different modulation formats are analyzed. The proposed PMD monitoring scheme is also demonstrated experimentally in 38-Gbit/s DQPSK and 57-Gbit/s D8PSK systems. It is experimentally shown that the PMD measurement results are not affected by CD and the measurement range is increased to 50 ps in systems with symbol rate of 19 GSymbole/s.

### 4.1 Principle of PMD Monitoring Based on RF Power Measurement

Signal propagating in optical transmission links is split into two orthogonal PSPs and each component travels along the fiber at different speeds due to the effect of DGD. At the end of fiber transmission, the two optical components can be out-of-phase and the corresponding RF power can be reduced through destructive interference. On the other hand, CD induces phase difference between the two sidebands and the RF power of the beating component is also affected by CD. The detected RF power of double sideband (DSB) signal is given by [121]

$$P_{DSB} = P_0[1 - 4\gamma(1 - \gamma)\sin^2(\pi f_{RF}\Delta\tau)]\cos^2(\pi D\lambda^2 f_{RF}^2/c), \quad (4.1)$$

where  $P_0$  is RF power without CD and PMD effects;  $\gamma$  is the power splitting ratio between the two PSPs;  $\Delta\tau$  is the DGD of the link;  $\lambda$  is the carrier wavelength;  $f_{RF}$  is the RF frequency;  $c$  is the speed of light;  $\gamma$  and  $\Delta\tau$  are PMD induced parameters, and  $D$  is the collective dispersion parameter of fiber link and optical components. From (4.1), it is observed that both CD and PMD change the RF tone power of DSB signal and it is difficult to distinguish CD and PMD through RF power measurement. If one of the sidebands is filtered out, the RF component power is insensitive to CD and only varies as a function of PMD [121]. The detected RF power of single sideband (SSB) signal is given by [121]

$$P_{SSB} = P_0[1 - 4\gamma(1 - \gamma)\sin^2(\pi f_{RF}\Delta\tau)]|H(f_{RF}^2)|^2/2, \quad (4.2)$$

where  $H$  is the electrical field transfer function of the optical filter. The division by 2 is due to the removal of one of sidebands. It can be seen that the detected RF power of SSB signal removes the affect of CD and varies as a function of DGD. It is also noted that the RF power of SSB signal changes periodically and the period is related to

#### 4.1 Principle of PMD Monitoring Based on RF Power Measurement

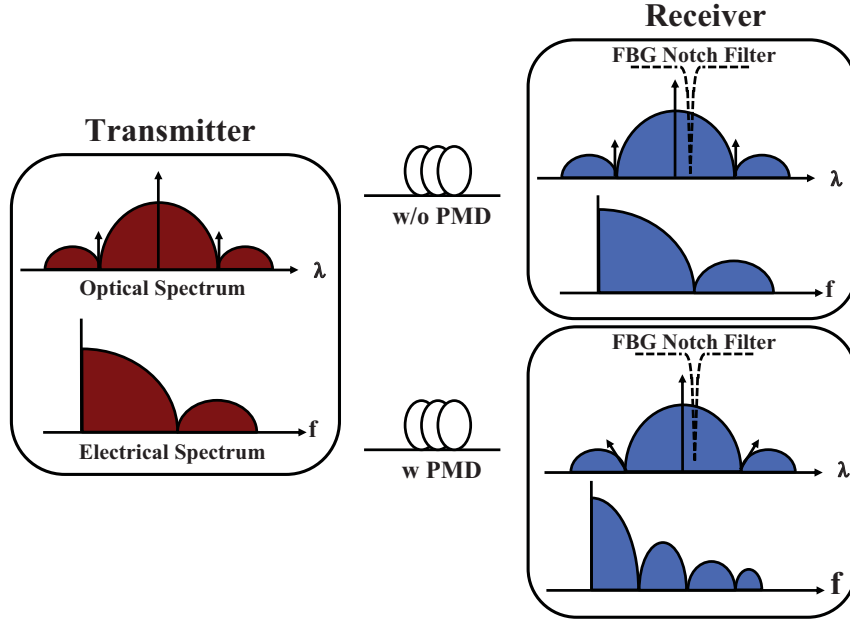


Figure 4.1: Principle of PMD monitoring for NRZ data.

the RF frequency. From (4.2), the DGD measurement range is inversely proportional to RF frequency. Thus, DGD measurement range can be increased by using a low frequency RF tone as monitoring signal.

We propose a technique for CD-insensitive PMD monitoring using a narrow band FBG notch filter placed 10 GHz off the optical carrier in high-speed transmission systems. The RF tone power at 10 GHz is used as a PMD monitoring signal, which is insensitive to the effects of CD. By placing the FBG at 10 GHz away from the optical carrier, the PMD monitoring range is increased to 0~50 ps and the bandwidth requirement of photodetector is reduced to 10 GHz.

Fig.4.1 shows the principle of the proposed method. At the transmitter, the optical carrier and the sidebands have the same polarization state. After propagating through a piece of fiber link, the optical components at two orthogonal PSPs have a phase difference and the RF power decreases with the PMD value in the system. As the

## 4.2 Simulation Results

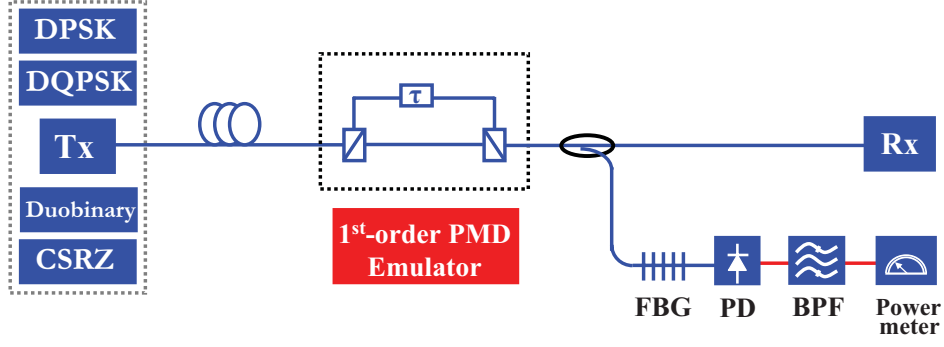


Figure 4.2: System setup of CD-insensitive PMD monitoring based on RF power measurement.

optical component at 10 GHz away in one of sidebands is filtered out, CD can only affect the phase of the 10 GHz RF tone but not the amplitude. Therefore, the 10 GHz RF tone power can be used as a PMD monitoring signal, which is insensitive to CD effects. If one of optical clock is filtered out in 40 GSymbol/s system and RF clock power is used as PMD monitoring signal, CD-insensitive PMD measurement can be achieved. However, the PMD measurement range is only 0~12.5 ps. By placing the FBG filter at 10 GHz away from the carrier, the PMD monitor range is broadened by four-times and the bandwidth requirement of photodetector is decreased four times. Besides, our proposed method is transparent to modulation format. This is because that the FBG filter not only eliminates the CD effect, but also create a RF tone by beating the carrier and the corresponding component at one sideband. Therefore, the clock tone of the signal is not required in the proposed method.

## 4.2 Simulation Results

Fig.4.2 shows the system setup of the proposed CD-insensitive PMD monitoring technique based on RF power measurement in a 40-Gbit/s transmission system. In the

## 4.2 Simulation Results

---

system, different modulation formats (DPSK, DQPSK, duobinary, and CSRZ OOK) were obtained by using various transmitters. CD is introduced by a piece of fiber link. First-order PMD is emulated using a piece of polarization maintaining fiber (PMF) and two polarization beam splitters (PBSs). An FBG notch filter (with a 3 dB bandwidth of 20 GHz and rejection of 30 dB) is placed at 10 GHz away from the optical carrier. The power of RF tone at 10 GHz varies as a function of PMD and is used as monitoring signal. The PMD measurement range of the proposed system is 0~50 ps, while it is only 0~12.5 ps if the FBG is placed at one of clocks in 40 GSymbol/s system. A photodetector with a bandwidth of 10 GHz is used to detect the power of beating components. 10-GHz RF tone is obtained by an electrical bandpass filter with a 3 dB bandwidth of 800 MHz. By measuring the power of 10-GHz RF tone, CD-insensitive PMD monitoring can be achieved and the measurement range is four times larger than that shown in [120]. Different modulation formats (CSRZ, DPSK, DQPSK and duobinary) are generated and the performances of proposed PMD monitoring method are analyzed.

### 4.2.1 Effect of PMD on RF power

The numerical simulation is calculated in the simulation tool VPItransmissionMaker 7.0. Fig.4.3(a) shows optical spectrum of 40-Gbit/s DQPSK signal. The 10 GHz RF power as a function of DGD under different CD values is shown in Fig.4.3(b). The RF power decreases with DGD in a range of 0~50 ps. However, chromatic dispersion also affect the RF power, which may induce errors on PMD measurement. It is observed that RF power is very small in the absence of CD. This is because the beat terms between the two sidebands and carrier are out of phase. As CD induces phase shift between the two sidebands, RF power is regenerated as CD increases. Therefore, 10 GHz RF power of DQPSK signal changes with both CD and PMD in the absence of

## 4.2 Simulation Results

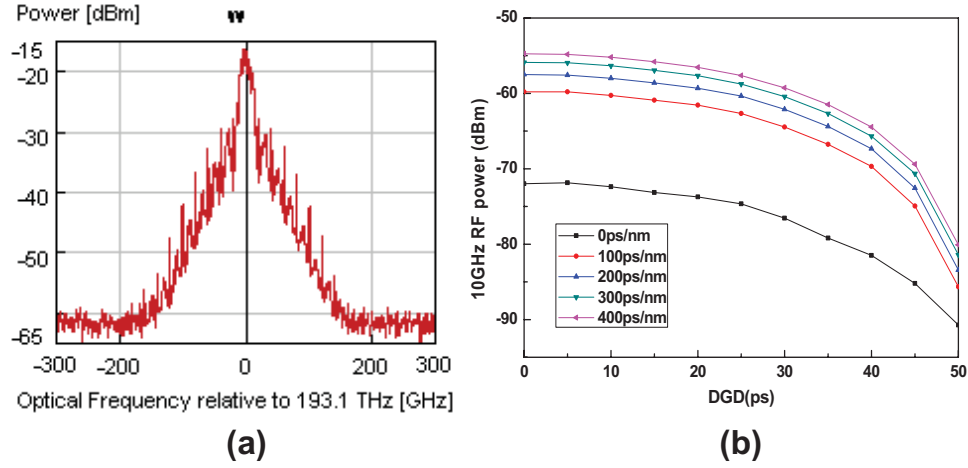


Figure 4.3: 40-Gbit/s DQPSK signal (a) optical spectrum; (b) Relative RF power as a function of DGD at different CD values.

FBG filter. Accurate PMD monitoring based on RF power can be achieved if CD effect is eliminated.

Fig.4.4(a) shows the optical spectrum of the 40-Gbit/s DPSK signal filtered by an FBG notch filter centered at 10 GHz away from the optical carrier. The rejection and 3-dB bandwidth of the FBG filter is 30 dB and 20 GHz, respectively. Fig.4.4(b)-(d) show the electrical spectra of filtered 40-Gbit/s DPSK signal received by a photodetector under different DGD values (0, 25 and 50 ps) in the absence of CD effect. It can be observed that the power of the beating component at 10 GHz is relatively high when both CD and DGD are zero. The received 10 GHz RF tone power decreases as the DGD value increases, which is due to the destructive interference induced by DGD. If the DGD value equals to half of the period time at certain frequency, the beating components destruct completely and has minimum power at that frequency. As the optical components at frequencies of  $(2N+1)/T$  reach the minimum power at the same DGD value ( $T/2$ ), the electrical spectrum has a comb like spectrum, shown as Fig.4.4(d).  $T$  is the period time and  $N$  is an integer. From Fig.4.4, it can be observed

## 4.2 Simulation Results

---

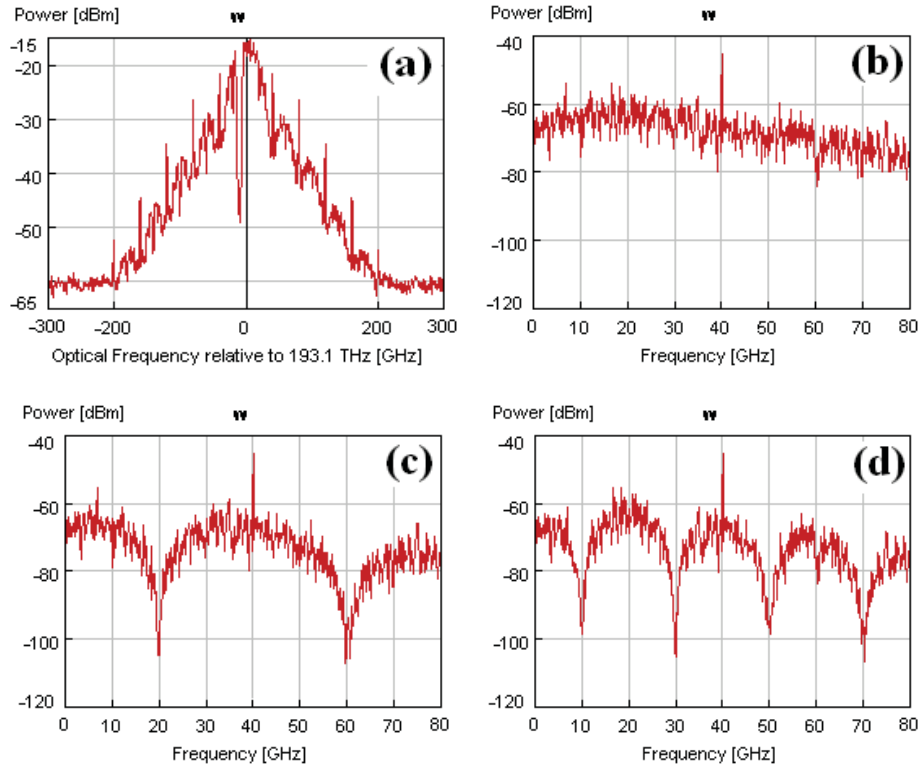


Figure 4.4: 40-Gbit/s DPSK signal (a) Optical spectrum of filtered signal; electrical spectra for (b) DGD=0ps, (c) DGD=25ps, and (d) DGD=50ps. CD=0ps/nm.

## 4.2 Simulation Results

---

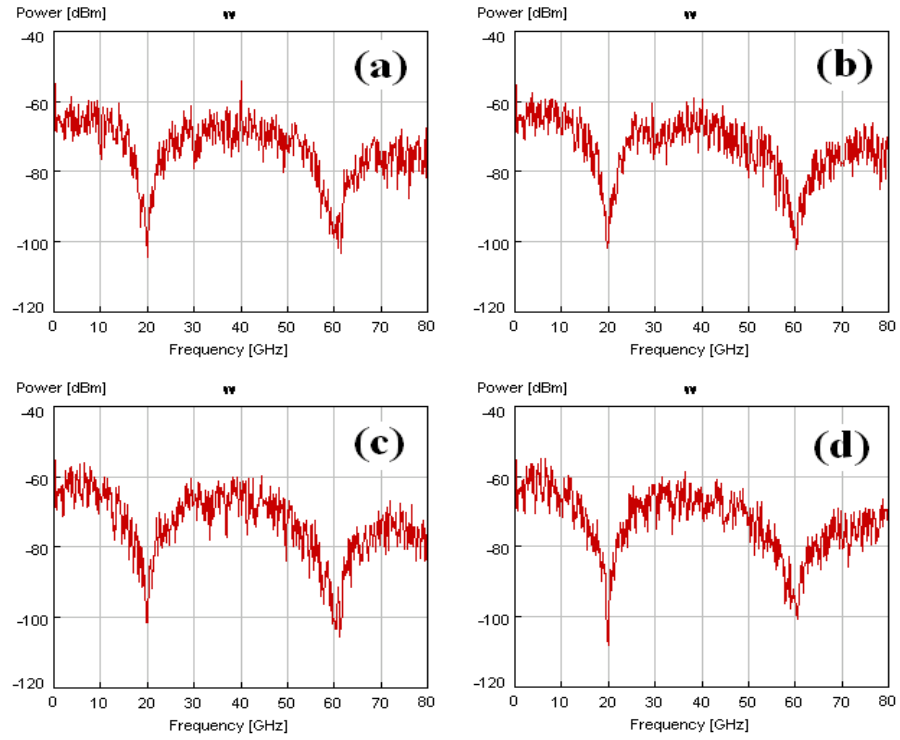


Figure 4.5: Electrical spectra of filtered 40-Gbit/s DPSK signal for (a)  $CD=100\text{ps/nm}$ , (b)  $CD=200\text{ps/nm}$ , (c)  $CD=300\text{ps/nm}$ , and (d)  $CD=400\text{ps/nm}$ .  $DGD=25\text{ps}$ .



## 4.2 Simulation Results

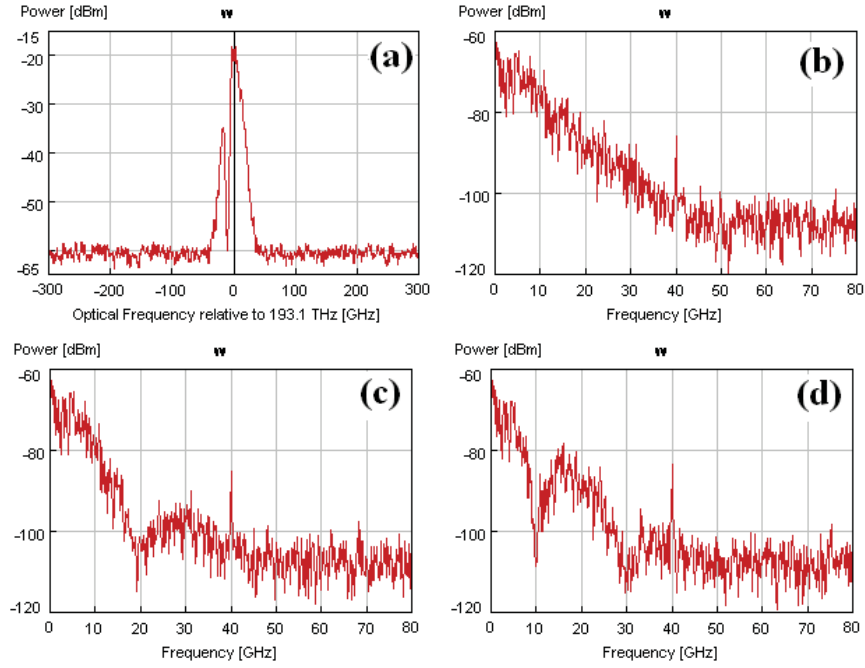


Figure 4.6: (a) Optical spectrum of filtered 40-Gbit/s duobinary signal and electrical spectra for (b) DGD=0ps, (c) DGD=25ps, and (d) DGD=50ps. CD=0ps/nm.

that the power of RF tone at 10 GHz varies as a function of PMD. Therefore, it can be used to monitoring the PMD value in 40-Gbit/s DPSK transmission system.

Fig.4.5 shows electrical spectra of the filtered 40-Gbit/s DPSK signal under different CD values (100, 200, 300 and 400 ps/nm) and the same DGD value (25 ps). It can be observed that the power of RF tone at 10 GHz has the same value and does not change with the CD effects. The proposed method is efficient on CD-insensitive PMD monitoring in 40-Gbit/s DPSK system.

One of the advantages of the proposed PMD monitoring method is that it is transparent to modulation format. Numerical simulation results for different modulation formats were analyzed. Fig.4.6(a) shows the optical spectrum of the 40-Gbit/s duobinary signal filtered by the FBG notch filter centered at 10-GHz away from the optical carrier. It can be seen that duobinary signal has much narrow optical spectrum com-

## 4.2 Simulation Results

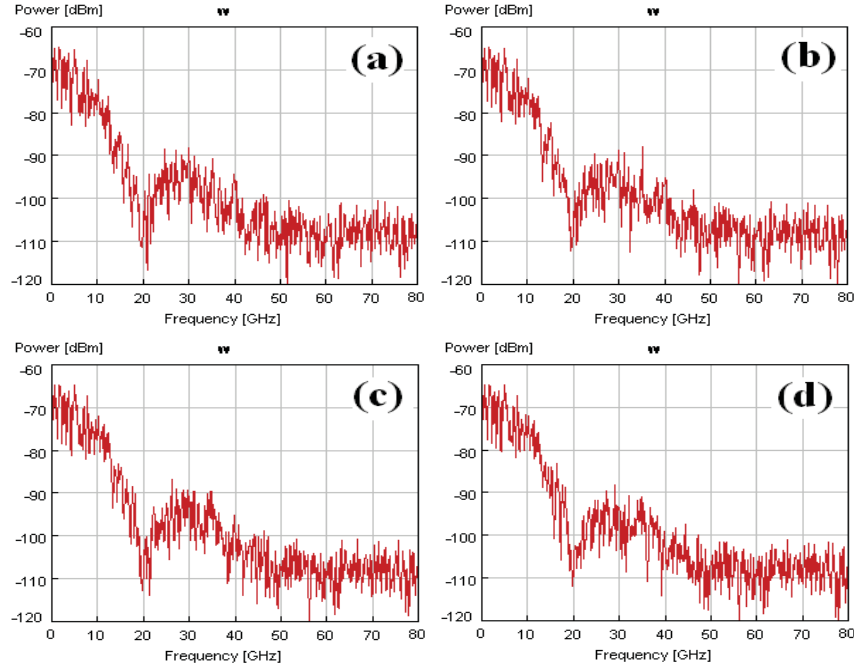


Figure 4.7: Electrical spectra of filtered 40-Gbit/s duobinary signal for (a)  $CD=100\text{ps/nm}$ , (b)  $CD=200\text{ps/nm}$ , (c)  $CD=300\text{ps/nm}$ , and (d)  $CD=400\text{ps/nm}$ .  $DGD=25\text{ps}$

pared with DPSK signal. In order to analyze the performance of the proposed method in the systems of different modulation formats “fairly”, the FBG notch filter with a 3-dB bandwidth of 20 GHz, which is the same as that used in DPSK system, is applied. Fig.4.6 (b)-(d) show the electrical spectra of the 40-Gbit/s duobinary signal filtered by an FBG notch filter under different DGD values (0, 25 and 50 ps) in absence of CD effects. It can be observed that although the spectra of duobinary signal is much different from that of the DPSK signal, the 10-GHz RF power decreases as a function of DGD. Therefore, the 10-GHz RF tone power varies with PMD in the transmission link and can be used on PMD monitoring in 40-Gbit/s duobinary system.

Fig.4.7(a)-(d) show the electrical spectra of the filtered 40-Gbit/s duobinary signal under different CD values (100 to 400 ps/nm) and the same DGD value (25 ps).

## 4.2 Simulation Results

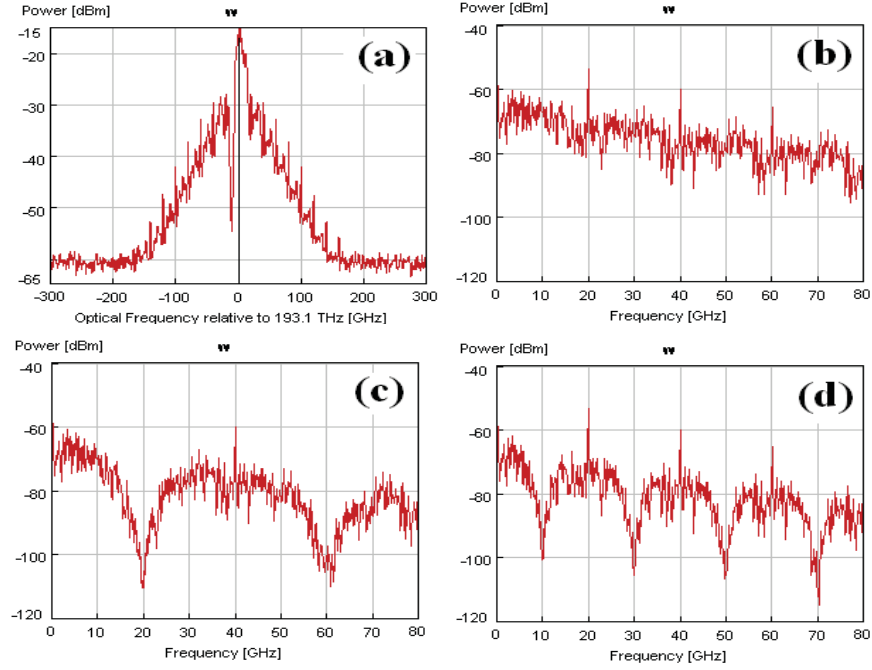


Figure 4.8: (a) Optical spectrum of filtered 40-Gbit/s DQPSK signal and electrical spectra for (b) DGD=0ps, (c) DGD=25ps, and (d) DGD=50ps. CD=0ps/nm.

From Fig.4.7, the beating components of the filtered duobinary signal are the same at different CD values. Thus, we can induce that the proposed method can be used to CD-insensitive PMD monitoring in duobinary system.

Fig.4.8(a)-(d) show the optical and electrical spectra of the 40-Gbit/s DQPSK signal filtered by the FBG notch filter centered at 10-GHz away from the optical carrier under different DGD values (0, 25 and 50 ps) in absence of CD effects. And Fig.4.9 shows the electrical spectra of the filtered 40-Gbit/s DQPSK signal under different CD values (100 to 400 ps/nm) and the same DGD value (25 ps). It can be observed that the proposed method is also efficient on CD-insensitive PMD monitoring in 40-Gbit/s DQPSK system.

For other modulation formats, such as NRZ, CSRZ, RZ DPSK, CSRZ DPSK and MSK etc., the optical spectra are different from each other. However, by using a

## 4.2 Simulation Results

---

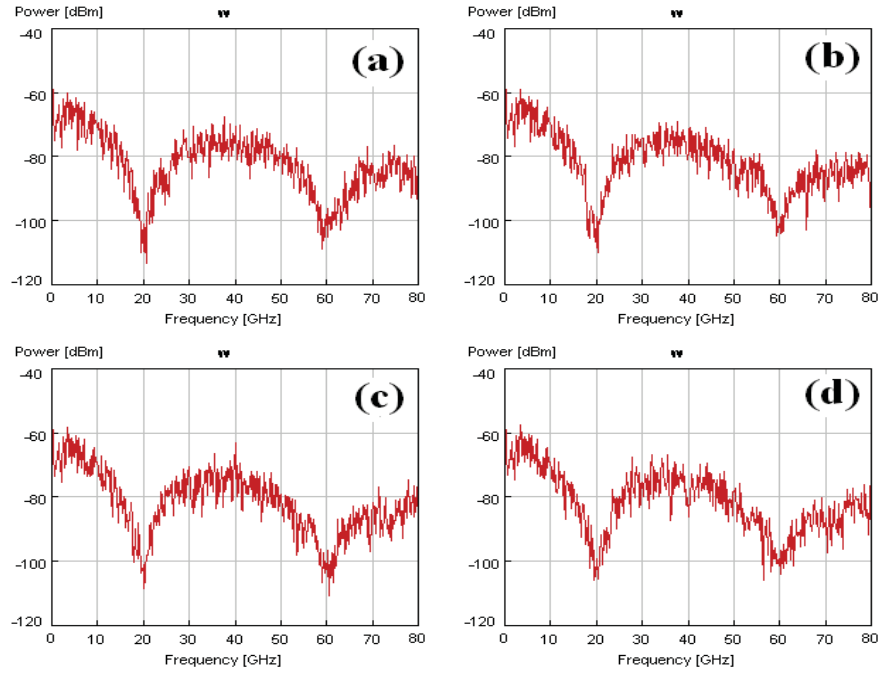


Figure 4.9: Electrical spectra of filtered 40-Gbit/s DQPSK signal for (a) CD=100ps/nm, (b) CD=200ps/nm, (c) CD=300ps/nm, and (d) CD=400ps/nm. DGD=25ps

## 4.2 Simulation Results

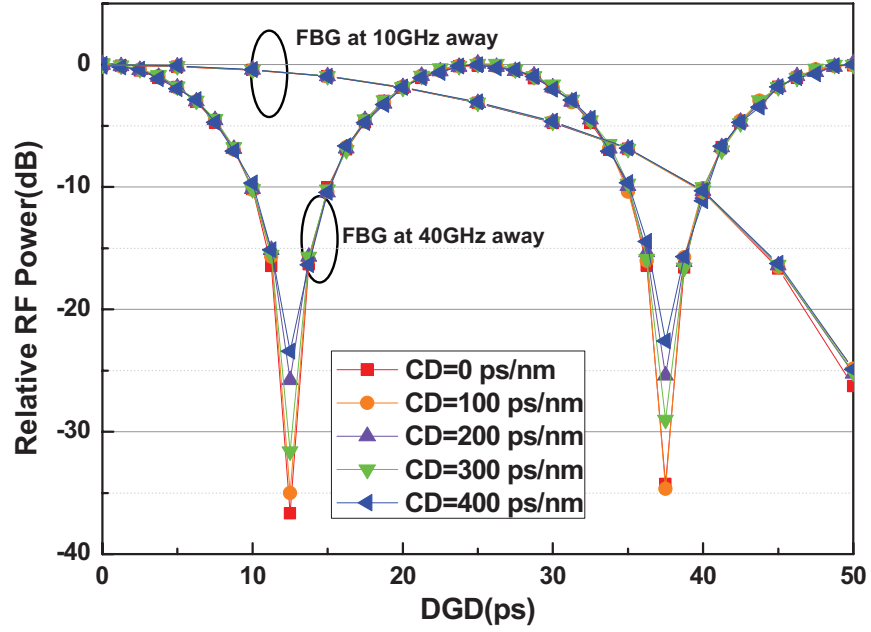


Figure 4.10: Relative RF power as a function of DGD at different CD for 40-Gbit/s DPSK signal when FBG filter is centered at 10-GHz and 40-GHz away from the carrier.

narrow band FBG notch filter centered at 10-GHz away the carrier, the corresponding RF tone power varies as a function of PMD and is insensitive to CD. As a result, the proposed PMD monitoring method is transparent to modulation format and can be used in different transmission systems.

### 4.2.2 CD-Insensitive PMD Monitoring Based on RF Power

Fig.4.10 shows the relative RF clock and 10-GHz power of 40-Gbit/s DPSK signal as a function of DGD. A FBG notch filter with a rejection of 30 dB and 3 dB bandwidth of 20 GHz was centered at optical clock and 10 GHz away from the carrier, respectively. Different CD values (100 ps/nm to 400 ps/nm) were applied in the system. It can be observed that the DGD measurement range is only 0~12.5 ps when the FBG filter is centered at one of optical clock and 40-GHz RF clock is used as a DGD monitoring

## 4.2 Simulation Results

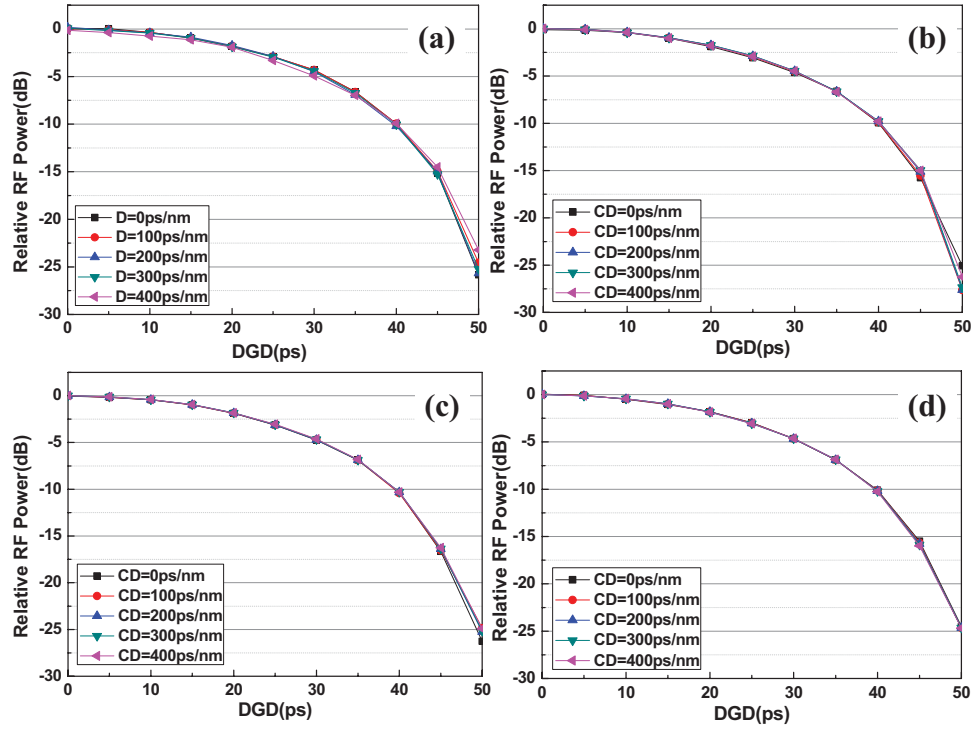


Figure 4.11: Relative RF power at 10 GHz as a function of DGD for different CD in 40-Gbit/s system: (a) CSRZ; (b) DPSK; (c) DQPSK; (d) Duobinary.

signal, while the DGD measurement range is increased to 0~50 ps by using a FBG filter centered at 10-GHz away from the carrier. From Fig.4.10, it is observed that the DGD measurement range is increased four times by using the proposed method. Besides, when the FBG filter is placed at 40-GHz away from the carrier, the dynamic range of RF clock power is wide ( $>35$  dB) in the absence of chromatic dispersion. However, it decreases to less than 25 dB when the CD increases to 400 ps/nm. By using our proposed method, the power of RF tone is insensitive to CD and the dynamic range is relative wide ( $>25$  dB).

The relative 10 GHz RF tone power as a function of DGD for different modulation formats are shown in Fig.4.11. The CD varies from 100 ps/nm to 400 ps/nm. The results for 40-Gbit/s CSRZ, DPSK, DQPSK and duobinary signals are analyzed. It can be observed that the power of 10-GHz RF tones varies as a function of DGD. The

## 4.2 Simulation Results

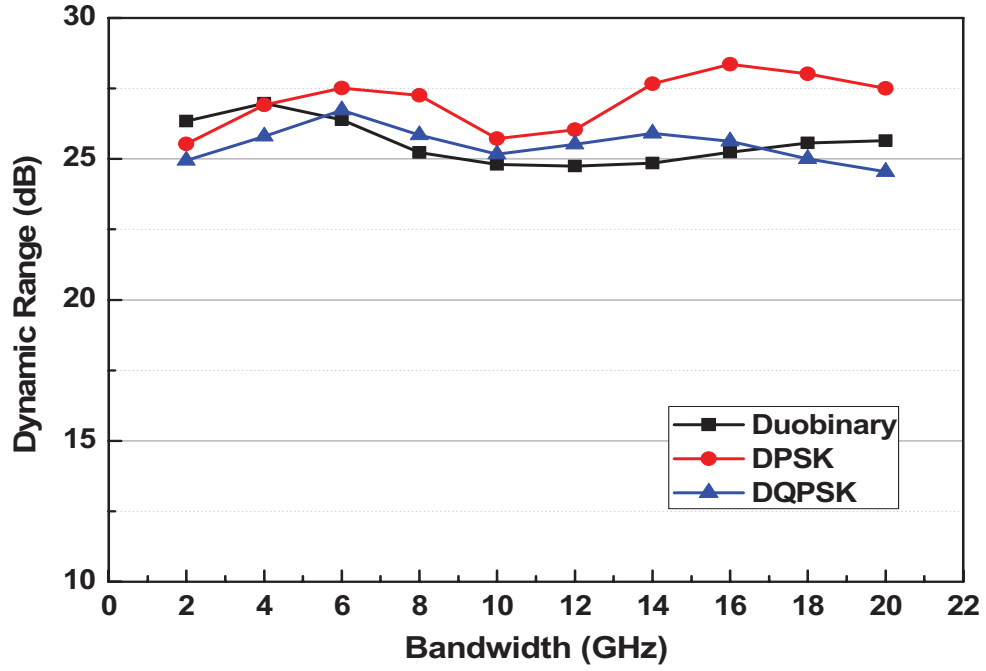


Figure 4.12: Dynamic range of RF tone power at 10 GHz as a function of FBG bandwidth in 40-Gbit/s system.

performance (DGD measurement range and dynamic range of RF power) is almost the same for different modulation formats. It can be induced that the proposed technique is efficient on CD-insensitive PMD measurement in the systems with different modulation formats.

### 4.2.3 Effects of FBG Filter Bandwidth and Frequency Detuning

Fig.4.12 shows effects of FBG filter bandwidth on the dynamic range of 10 GHz RF tone power in 40-Gbit/s DPSK, DQPSK and duobinary systems. An FBG filter is centered at 10 GHz away from the optical carrier. It is observed that 10-GHz RF power has almost the same dynamic range ( $\sim 26$  dB) under FBG filters with different bandwidths. This is due to the fact that the PMD induced RF fading can be obtained as long as the optical component at 10-GHz away is filtered out. If narrow band FBG

## 4.2 Simulation Results

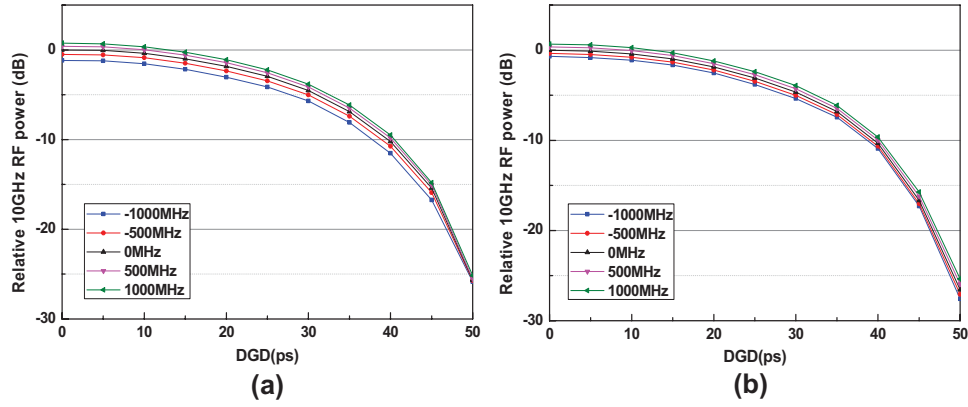


Figure 4.13: Relative 10GHz RF power as a function of DGD under FBG filter frequency detuning in 40-Gbit/s (a) DQPSK and (b) duobinary systems.

filter is used, only the RF tone at 10-GHz can be used as a PMD monitoring signal which is not affected by CD. If a wide band FBG filter is used, the 10-GHz RF tone still reveal the PMD effect. Thus, the PMD measurement results will not be affected much by the FBG bandwidth as long as the optical carrier and the other sideband is not filtered away. Besides, if the notched optical spectrum is wide, the RF tones other than 10-GHz can also be used to monitor the PMD value, and the result is not affected by CD. However, the PMD measurement range will be different for various RF tones.

The center wavelength of FBG notch filter may shift from the original value under various environment effects, which may introduce RF power fluctuation and PMD measurement errors. Fig.4.13 shows the effects of FBG frequency detuning on the 10 GHz RF power in 40-Gbit/s DQPSK and Duobinary systems. It is observed that the maximum 10 GHz RF power changing is less than 1.2 dB and 0.7 dB when the FBG frequency detuning is 1 GHz in DQPSK and duobinary system, respectively. However, the RF power is not linearly related to the PMD value. The FBG frequency detuning induced measurement error is different for various DGD values. The measurement error is larger in the small DGD range, where the slope of RF power is smaller. In



## 4.2 Simulation Results

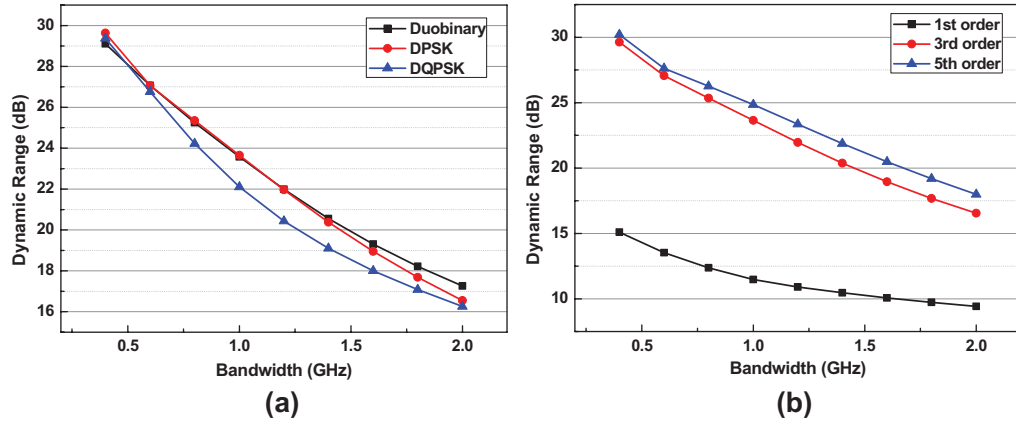


Figure 4.14: Dynamic range of 10 GHz RF power as a function of electrical filter bandwidth (a) in duobinary, DQPSK and DPSK systems; (b) for different filter orders.

other words, if the FBG frequency detuning induced RF power changing is the same in the whole PMD monitoring window, the measurement error is larger for small DGD values. Therefore, the frequency detuning effect on the small DGD values is larger.

Fig.4.14(a) shows the dynamic range of 10 GHz RF power as a function of electrical filter bandwidth in 40-Gbit/s duobinary, DQPSK and DPSK systems. A 3rd order Gaussian shape filter centered at 10 GHz is used to filter out the monitoring signal. For different modulation formats, the effects of filter bandwidth is the same. It is observed that the dynamic range decreases with the electrical filter bandwidth. This is because the RF tones around 10 GHz are also detected by the power meter when wide band electrical filter is applied. When the DGD is zero, the RF tones around 10 GHz has almost the same power as 10 GHz RF tone. Therefore, the detected RF power change is not affected much by the filter bandwidth. When the DGD is 50 ps, where the 10 GHz RF power decreases to minimum value, the RF tones around 10 GHz is much larger than that of 10 GHz RF tone. Thus the detected RF power increases dramatically if electrical filter with large bandwidth is used. The dynamic range of 10 GHz decreases with the electrical filter bandwidth.

### 4.3 Experimental Results

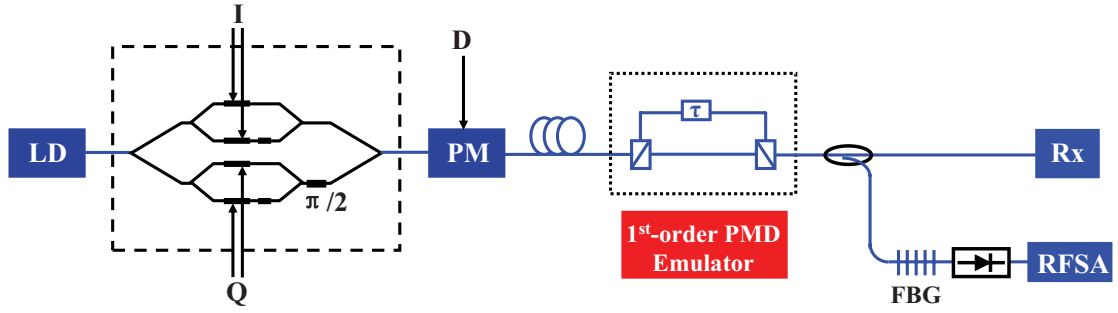


Figure 4.15: Experimental setup of PMD monitoring utilizing FBG notch filter in an 8-PSK system. LD: laser diode; PM: phase modulator.

Fig.4.14(b) shows the dynamic range of 10 GHz RF power as a function of electrical filter bandwidth for different filter orders (1st, 2nd and 3rd Gaussian) in 40-Gbit/s DPSK system. The RF power dynamic range is less than 15 dB if 1st order Gaussian filter is used. While, RF power dynamic range is 10 dB larger if 2nd or 3rd order Gaussian filter is applied. From Fig.4.14, it is obvious that in order to get large dynamic range, the electrical filter should be narrow enough to filter out the 10 GHz RF tone and eliminate components around 10 GHz.

### 4.3 Experimental Results

The experimental setup of CD-insensitive PMD monitoring in D8PSK system is shown in Fig.4.15. Continuous wave (CW) tunable laser at the wavelength of 1550.02 nm is launched into a transmission module. The modulators are driven by 19-Gbit/s pseudo-random bit sequence (PRBS) data with a length of  $2^7 - 1$ . 38-Gbit/s DQPSK signal is generated by an in-phase/quadrature (IQ) modulator and 57-Gb/s D8PSK signal can be generated by phase modulating the output signal of IQ modulator. The generated signal passes through several spans of dispersion compensation fiber (DCF), which provide CD from 0~330 ps/nm. Two polarization beam splitters (PBSs) and a tunable optical

### 4.3 Experimental Results

---

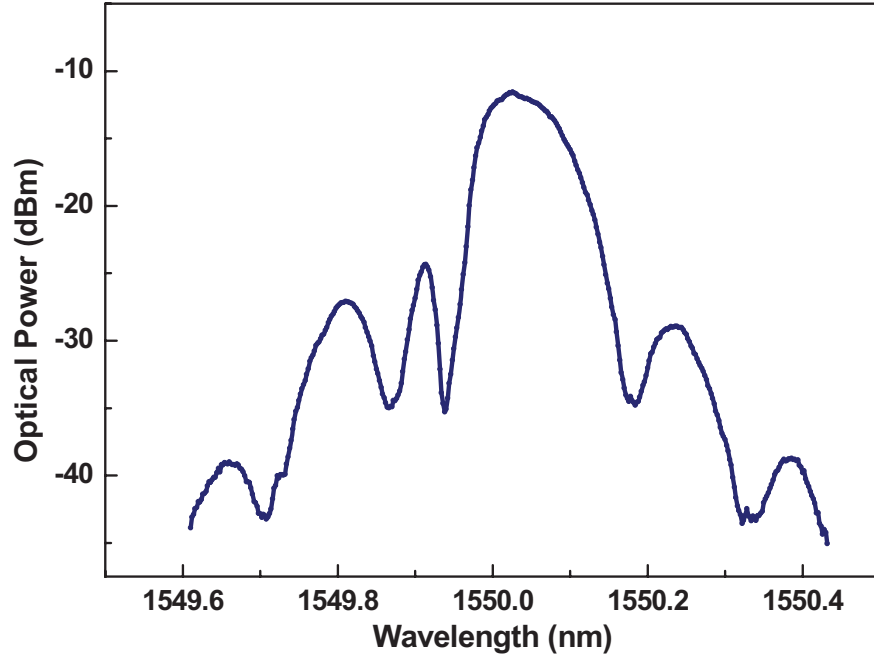


Figure 4.16: Optical spectrum of 38-Gbit/s DQPSK signal filtered by a narrow band FBG notch filter.

delay line are used as a first-order PMD emulator. At the monitoring branch, An FBG notch filter with bandwidth of 0.06 nm and reflection of 15 dB is placed at 10 GHz away from the carrier frequency such that the measured 10 GHz RF power is insensitive to CD. The filtered signal was received by a 10 GHz photodetector. A RF spectrum analyzer is used to monitoring the 10 GHz RF tone powers. Note that the narrowband FBG filter is only in the monitoring branch, and do not affect the received signal.

#### 4.3.1 PMD Monitoring in 38-Gbit/s DQPSK System

Fig.4.16 shows the optical spectrum (with resolution of 0.01nm) of 38-Gbit/s DQPSK signal filtered by an FBG notch filter. The optical component at 10 GHz away from the carrier was filtered out by an FBG (with bandwidth of 0.06 nm and reflection of 15 dB). Therefore, the 10 GHz RF power can be used as monitoring signal to obtain CD-

### 4.3 Experimental Results

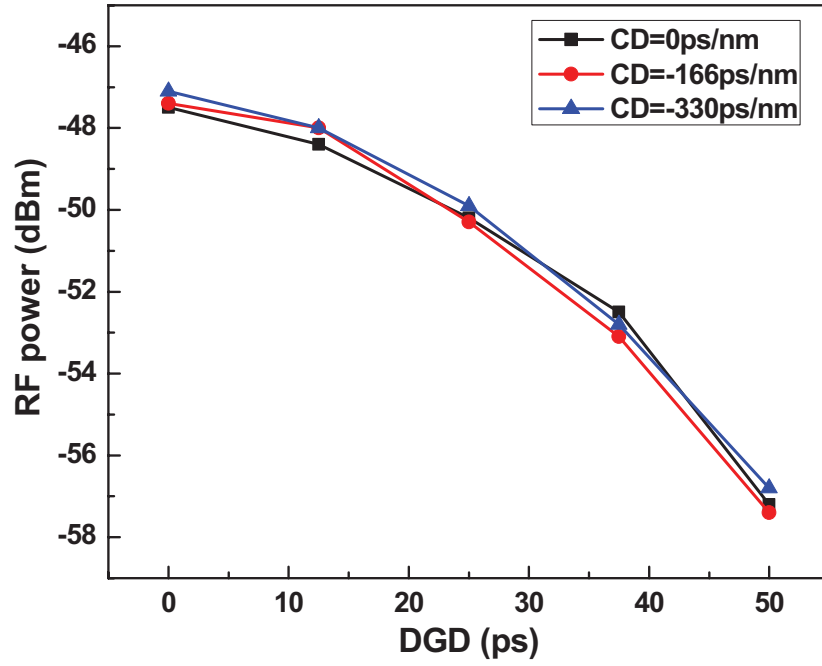


Figure 4.17: RF power at 10-GHz as a function of DGD for different CD values in 38-Gbit/s DQPSK system.

insensitive DGD. Fig.4.17 shows 10 GHz RF tone power as a function of DGD value in 38-Gbit/s DQPSK system. Different CD values were introduced by several pieces of DCF. The intensity of 10 GHz RF tone is quite small at a DGD of 50ps. This is due to the optical components at the two orthogonal polarization states have a phase shift of  $\pi$  and the beating component destruct completely at 10 GHz. The RF power varies as a function of DGD and the measurement range is 0~50 ps. As one of sideband is filtered out by the FBG notch filter, 10 GHz RF power is insensitive to CD. The dynamic range of RF power is around 10 dB, which is limited by the signal-to-noise ratio of the signal.

### 4.3 Experimental Results

---

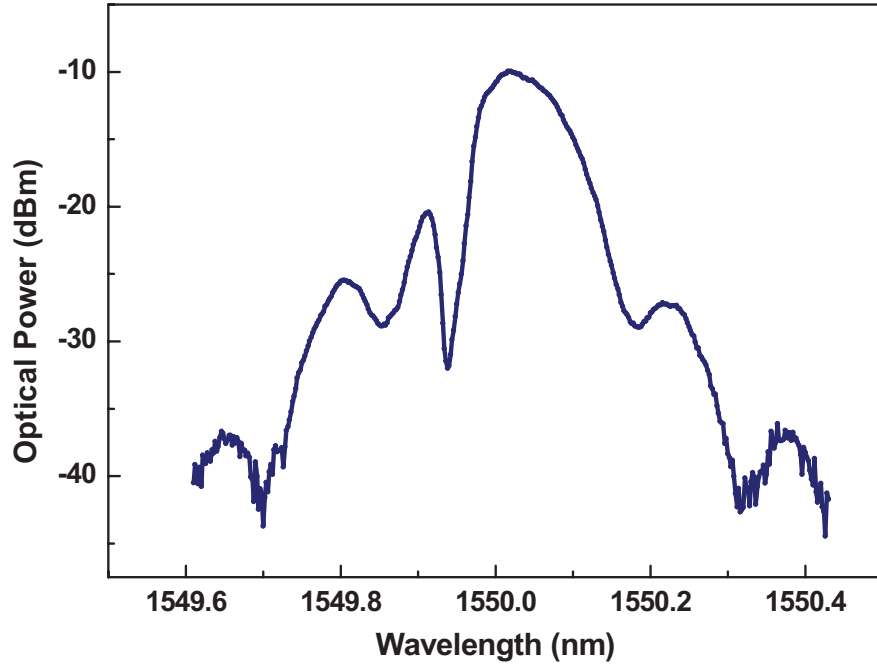


Figure 4.18: Optical spectrum of 57-Gbit/s D8PSK signal filtered by a narrow band FBG notch filter.

#### 4.3.2 PMD Monitoring in 57-Gbit/s D8PSK System

The proposed scheme is transparent to modulation format. It is experimentally demonstrated that the method is also efficient in DQPSK system. Fig.4.18 shows the optical spectrum of 57-Gbit/s D8PSK signal filtered by an FBG notch filter placed 10 GHz off the carrier. Fig.4.19 shows RF tone power at 10 GHz as a function of DGD value in 57-Gbit/s D8PSK system. It is observed that the proposed method is also efficient on CD-insensitive PMD monitoring in DQPSK system. The FBG notch filter can be placed closer to the carrier, and the DGD measurement range will be increased further. However, the bandwidth of the FBG should be very narrow to avoid the filtering of carrier.

Fig.4.20 shows measured RF spectra (with resolution of 1 MHz) when the 38 Gb/s DQPSK signal transmits through fiber links with different DGD values. In order

### 4.3 Experimental Results

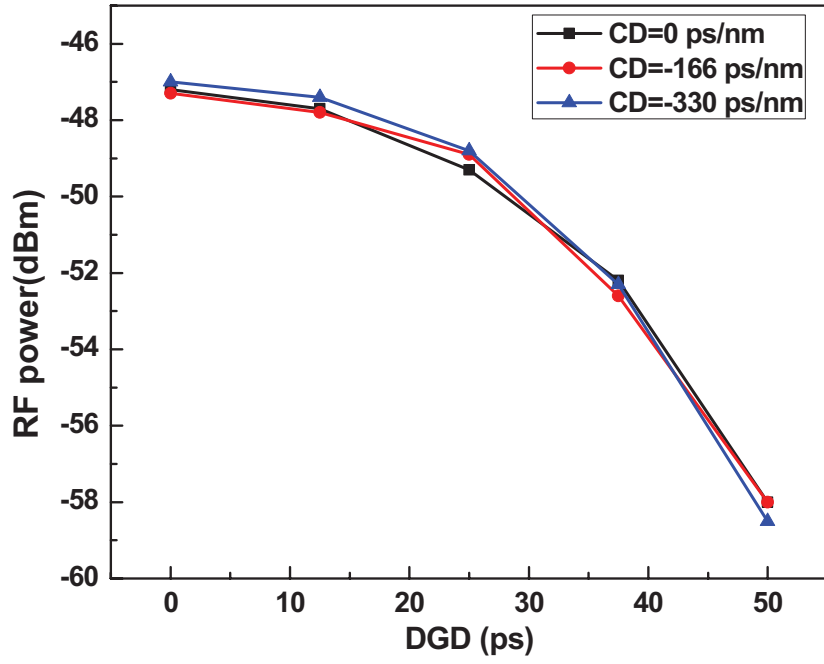


Figure 4.19: RF power at 10-GHz as a function of DGD for different CD values in 57-Gbit/s D8PSK system.

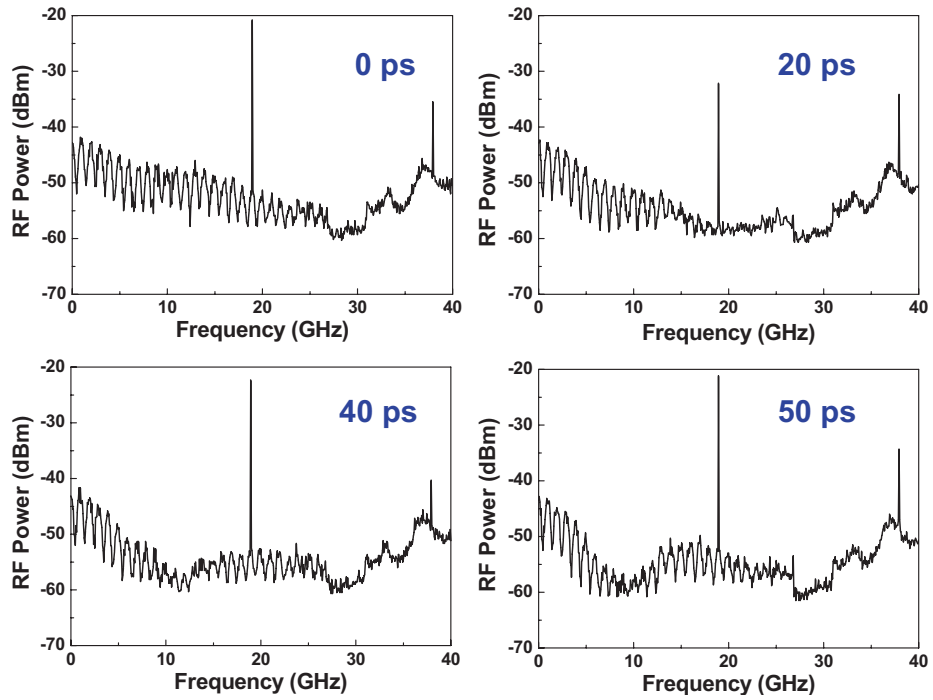


Figure 4.20: RF spectra of 38-Gb/s DQPSK signal for different DGD values.

## 4.4 Conclusions

---

to compare the RF power at 10 GHz and 19 GHz, PD with bandwidth of 40 GHz was utilized. It can be observed that the 10 GHz RF tone power monotonically decreases when the DGD increases from 0 to 50 ps, since the DGD measurement range is 50 ps if it is used as the monitoring signal. The DGD measurement range is only around 26.3 ps when 19 GHz RF tone power is used as the monitoring signal. In addition, we can see that the power of 19 GHz tone decreases when DGD increases from 0 to 20 ps, but increases again when DGD increases to 40 and 50 ps. This is due to the fact that the optical components at the two orthogonal polarization states have a phase shift of  $\pi$  and the beating component destruct completely when the DGD value equals to half of the symbol period at certain frequency. Therefore, the DGD measurement range is larger if a 10 GHz RF tone is used as the monitoring signal instead of a 19 GHz RF tone.

## 4.4 Conclusions

A CD-insensitive PMD monitoring method based on RF power measurement and optical filtering was proposed. By filtering out the optical component in one sideband, the CD effect on RF power can be eliminated. 10 GHz RF tone power was used as a monitoring signal in high-speed transmission systems to get larger PMD measurement range to 0~50 ps. Numerical simulation results of CD-insensitive PMD measurement for different modulation formats (CSRZ, DPSK, DQPSK and duobinary) in 40-Gbit/s systems are shown. The results show that the proposed method is insensitive to modulation format. The effects of FBG filter bandwidth on the PMD monitoring for different modulation formats are analyzed. It is shown that the dynamic range of the monitoring signal is not affected much by the bandwidth of the FBG filter. The effects of FBG frequency detuning is analyzed numerically. The maximum 10 GHz RF power

#### 4.4 Conclusions

---

changing is less than 1.2 dB and 0.7 dB when the FBG frequency detuning is 1 GHz in DQPSK and duobinary system, respectively. The dynamic range of the RF power can be improved if the bandwidth of the electrical filter is optimized.

The proposed method is also demonstrated experimentally. PMD monitoring technique using a narrow band FBG filter is presented in 38-Gb/s DQPSK and 57-Gb/s D8PSK systems. It is experimentally shown that the PMD measurement results are not affected by CD and the measurement range is increased to 0~50 ps in systems with symbol rate of 19-GSymbol/s. Besides, the technique uses low-bandwidth PD (10 GHz) and is therefore an efficient and cost effective PMD monitoring method.



## **Chapter 5**

# **CD Monitoring in High-speed Optical Transmission Systems**

Chromatic dispersion (CD) effect is one of major factors limiting the transmission distance in high-speed dense wavelength division multiplexing (DWDM) systems. It may change with network reconfigurations and many environmental conditions such as temperature. Hence, real-time CD monitoring has attracted a lot of interests and many techniques have been reported on CD monitoring and compensation.

The pilot tone method [127,128] was proposed to monitor CD value by measuring phase difference between the upper and lower sidebands of the subcarrier signal. However, the pilot tone could interfere with data and cause power penalty in the system. CD induced radio-frequency (RF) clock fading was proposed to monitor CD for return-to-zero (RZ) and non-return-to-zero (NRZ) signals [129,130]. However, the measurement results are affected by the received optical power and polarization mode dispersion (PMD) effect. A technique which can monitor CD and PMD simultaneous using an unbalanced Mach-Zehnder delay line interferometer (DLI) was reported [131]. However, additional interferometer, which is costly for real systems, is required. Another

## 5. CD Monitoring in High-speed Optical Transmission Systems

---

method based on power ratio of two RF tone powers was proposed. It requires modification of the transmitter, and the added RF tones may introduce degradation on data quality [132].

Eye diagrams have been considered as a useful tool for monitoring CD, PMD, signal-to-noise ratio (SNR) and other impairments in optical transmission systems [133]. However, clock synchronization is required so that the sampling can be synchronized to the signal. Many monitoring techniques have been proposed based on asynchronous sampling method [134–136], which can operate without clock extraction. However, it is still challenging to identify a particular impairment in the presence of other impairments. Recently, asynchronous delay-tap sampling was reported [137, 138]. This method uses a delay-tap line and a pair of data could be obtained in one sampling. Multiple impairment measurements as well as signal quality are extracted from the two dimensional histogram of signal. CD monitoring for DPSK signal by utilizing asynchronous delay-tap sampling was proposed [139]. However, addition phase shift of  $\pi/4$  should be added in one arm of conventional DPSK receiver, which may introduce power penalty to the received data. Asymmetry ratio of delay-tap sampling is proposed on residual CD monitoring for CSRZ DQPSK signal [140]. However, for the reported asynchronous delay-tap sampling methods, the measurement resolution is not high when the residual CD is small.

In this chapter, three CD monitoring methods are demonstrated. Two of the them are based on RF power measurement and narrow band fiber Bragg grating (FBG) filtering. For an NRZ signal, the RF clock power increases with CD and decreases with PMD. In method 1, an FBG filter is centered at the carrier wavelength, and the RF clock power decreases with both CD and PMD. Therefore, the RF clock power ratio of filtered and non-filtered signals can be used on PMD-insensitive CD monitoring. Both simulation and experimental results show that it is an efficient PMD-insensitive

## 5. CD Monitoring in High-speed Optical Transmission Systems

---

CD monitoring method. It is experimentally shown that the CD measurement range is 0~200 ps/nm in 38-Gbit/s DQPSK system. The measurement results are not affected by the optical power of received signal and good measurement sensitivity (0.14 dB/(ps/nm)) can be achieved.

In method 2, a narrow band FBG filter is placed at 10-GHz away from the carrier in one of the two sidebands. The 10-GHz RF tone power of the filtered signal decreases with PMD and insensitive to CD. Therefore, the 10-GHz RF tone power can be used as a CD-insensitive PMD monitoring signal. The PMD monitoring range is 0~50 ps in 38-Gbit/s DQPSK system. The 10-GHz RF tone power ratio of filtered and non-filtered signals varies with CD and insensitive to PMD. The CD monitoring range is increased to 0~500 ps/nm in 38-Gbit/s DQPSK system. However, the CD measurement sensitivity is smaller than that in method 1.

Another CD measurement method is based on amplitude ratio of asynchronous delay-tap sampling plot. The simulated results show that our method is efficient on residual CD measurement in 40-Gbit/s 50% RZ DQPSK, CSRZ DQPSK and 60-Gbit/s 50% RZ D8PSK systems in low CD region (0~75 ps/nm for 40-Gbit/s DQPSK systems). Since no modification on the transmitter or receiver is required, the proposed scheme is simple and cost effective.

Among the three CD monitoring methods, method 1 and method 2 are insensitive to PMD and have larger measurement range (0~200 and 0~500 ps/nm in 40-Gbit/s DQPSK system for method 1 and method 2, respectively). Compared with the first two methods, method 3 has limited measurement range (less than 100 ps/nm in 40-Gbit/s DQPSK system). Besides, the CD monitoring results may be affected by other impairment effects, such as PMD and OSNR. However, the measurement sensitivity of method 3 is better.

### 5.1 CD Monitoring Based on RF Tone Power Ratio Measurement

For NRZ signal, there is no RF clock tone after the detection of photodetector. This is due to the fact that the beat terms between the two sidebands and carrier are out of phase. Chromatic dispersion through the fiber link changes the phase difference between the sidebands, which induces RF regeneration for NRZ signals and RF fading for RZ signals [129]. However, PMD induced RF power fading may result in measurement error of CD monitoring based on RF power measurement. In this section, PMD-insensitive CD monitoring methods based on RF power ratio measurement utilizing FBG filter are demonstrated.

#### 5.1.1 Operation Principle

In the back-to-back case, the NRZ signal has no clock while the filtered NRZ signal has large clock power. After propagation through a piece of fiber link, the accumulated CD induces distortion on the signals. By using a narrow band FBG notch filter located at carrier wavelength, the RF clock power decreases with CD, which is opposite to that without filter. And the ratio of the two RF powers increases with CD and has large dynamic range, which results in better measurement sensitivity.

On the other hand, differential group delay (DGD) results in phase difference between the two orthogonal optical components and the corresponding RF power is reduced through destructive interference. PMD induces RF tone power fading through the transmission and the fading effect is the same regardless of whether the notch filter is present or not. Therefore, by taking the ratio of the RF power without filtering to that filtered by FBG, PMD effects on RF power can be eliminated.

We propose a technique for PMD-insensitive CD monitoring using a narrow band

## 5.1 CD Monitoring Based on RF Tone Power Ratio Measurement

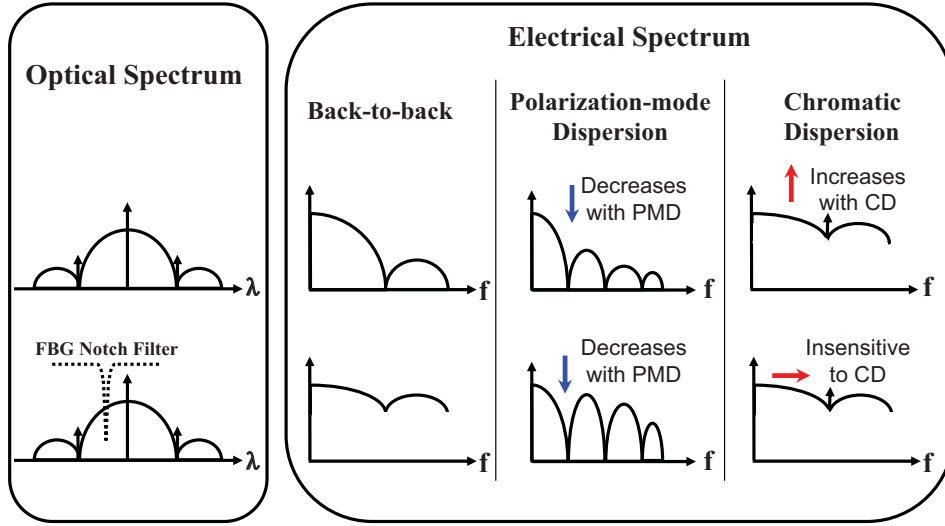


Figure 5.1: Principle of RF clock power changing under CD and PMD for NRZ and filtered NRZ signals.

FBG notch filter placed at carrier frequency in 38-Gb/s NRZ-DQPSK and 57-Gb/s NRZ-D8PSK transmission systems. The RF clock tone power ratio is used as a CD monitoring signal, which is insensitive to PMD effect. The monitoring range is 0~200-ps/nm for both systems as their symbol rate are the same, 19-Gsymbols/s.

Fig.5.1 shows the operating principle of our proposed CD monitoring method. Chromatic dispersion through the fiber link changes the phase of the sidebands compared to the carrier, which changes the RF tone powers after detected by a photodetector. The RF tone power can be used for CD monitoring [129]. However, the RF power is also affected by first-order PMD, which is also known as differential group delay (DGD). If DGD value equals to half period time of a certain frequency, the optical components at two orthogonal polarization states have a phase shift of  $\pi$  and there is no beating component at corresponding RF frequency. Therefore, PMD induced RF power fading may result in errors for CD measurement.

If a narrow band FBG notch filter is placed at 10-GHz away from the carrier in

## 5.1 CD Monitoring Based on RF Tone Power Ratio Measurement

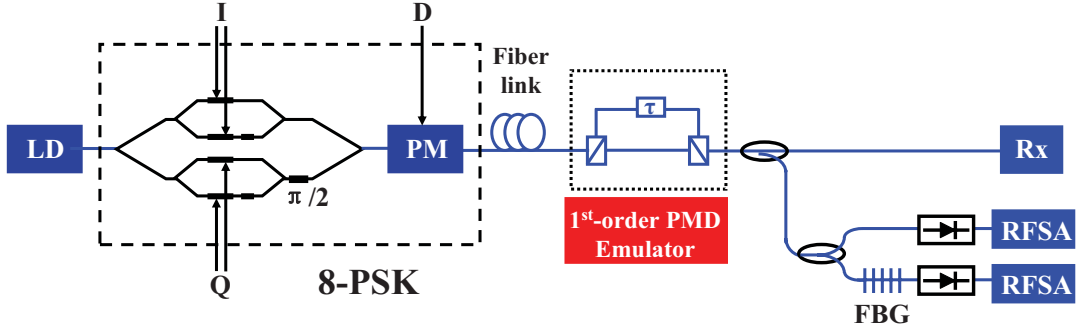


Figure 5.2: System setup of PMD-insensitive CD monitoring based on RF power measurement.

one of the sidebands (shown in Fig.5.1), 10-GHz RF tone power will be regenerated. The RF powers in other frequencies also increases due to the bandwidth limitation of FBG filter. As the optical component which is 10-GHz from the carrier in one sideband is filtered out, CD results in phase shift to the RF tone while the amplitude of 10-GHz RF tone is constant. PMD induces RF tone power fading through transmission and the fading effect is the same regardless of whether the notch filter is present or not. Therefore, by taking the ratio of the 10-GHz RF power without filtering to that filtered by FBG, PMD effects on RF power can be eliminated. Compared to the method using clock tone as the monitoring signal, the CD measurement range is increased while the required bandwidth of the photodetector in our technique is much lower.

### 5.1.2 System Setup

The experimental setup of PMD-insensitive CD monitoring in 57-Gbit/s NRZ-D8PSK system is shown in Fig.5.2. Continuous wave (CW) tunable laser is launched into a transmission module. The modulators are driven by 19-Gbit/s pseudorandom bit sequence (PRBS) data with a length of  $2^7 - 1$ . Variable optical delays are used to decorrelate the three channels. 38-Gb/s DQPSK signal is generated by an in-phase/quadrature (IQ) modulator and 57-Gbit/s D8PSK signal can be achieved at the output of phase

## 5.1 CD Monitoring Based on RF Tone Power Ratio Measurement

---

modulator (PM). The generated signal propagates through several spans of dispersion compensation fiber (DCF), which provide CD from 0~330 ps/nm. Polarization beam splitters (PBSs) and a tunable optical delay line are used as a first-order PMD emulator. The monitoring channel is split into two branches by a 50:50 coupler. In one of monitoring branches, an FBG notch filter with bandwidth of 0.06 nm and reflection of 15 dB is placed at the carrier wavelength, so that the RF clock power is decreases with both CD and PMD. If the FBG is placed at one of the clock wavelength, the RF clock power is insensitive to CD and decreases with PMD. If the FBG is placed at 10-GHz away from carrier, 10-GHz RF tone power is the CD-insensitive PMD monitoring signal. And the 10-GHz power ratio of filtered and non-filtered signal is a PMD-insensitive CD monitoring signal. The filtered signal is received by a photodetector. RF spectrum analyzer is used to monitoring the RF tone power. In the other monitoring branch, the signal is received directly by a photodetector and the 10-GHz RF tone power is affected by both CD and PMD effects. Note that the narrow band FBG filter is only in the monitoring branch, and does not affect the received signal.

### 5.1.3 FBG Filter Centered at Optical Carrier Wavelength

A narrow band FBG notch filter centered at the optical carrier wavelength, so that the RF clock power decreases with both CD and PMD. By using RF clock power ratio of filtered and non-filtered signals, PMD-insensitive CD monitoring can be achieved. Fig.5.3(a) shows the simulated optical spectrum of a 38-Gb/s NRZ-DQPSK signal filtered by an FBG notch filter. The optical component at the carrier was filtered out by an FBG (with bandwidth of 0.06 nm and reflection of 15 dB). The filtering induces distortion to the original signal. However, by choosing an FBG with optimal bandwidth and reflection, the RF clock tone can be regenerated in the back-to-back case and decreases with CD when transmitting through fiber link and components. Fig.5.3(b)

## 5.1 CD Monitoring Based on RF Tone Power Ratio Measurement

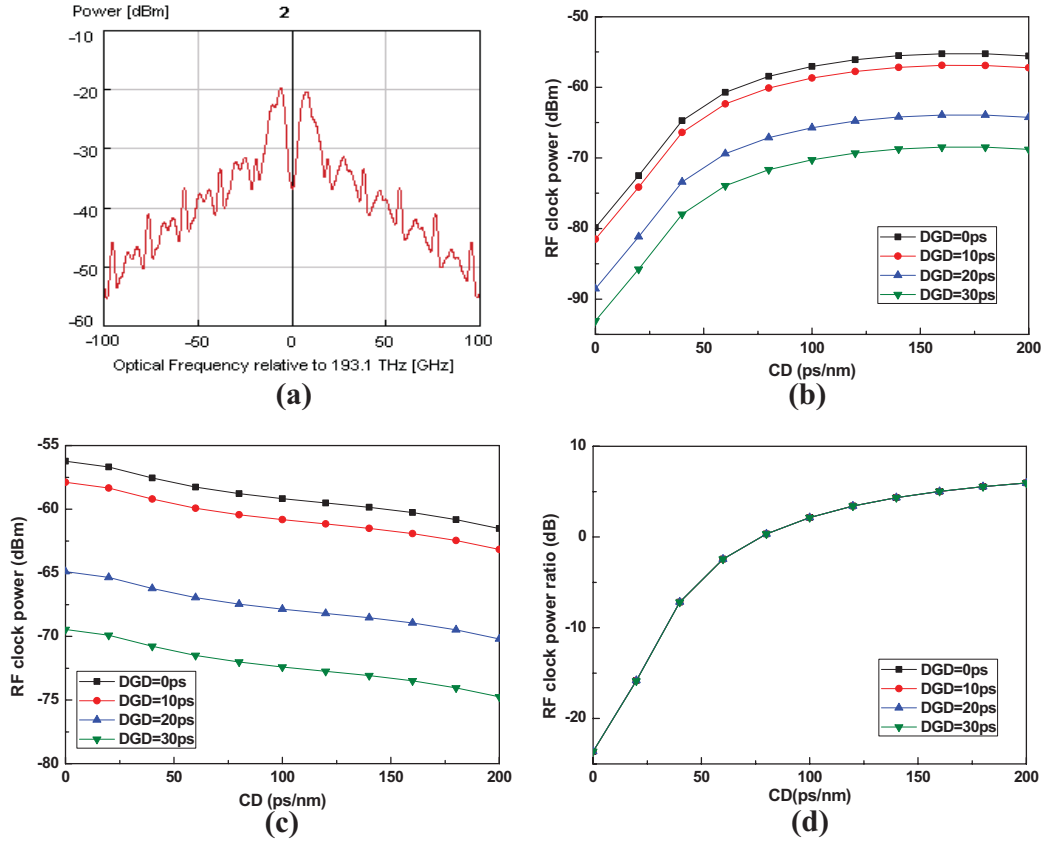


Figure 5.3: Simulation results of 38-Gbit/s NRZ-DQPSK (a) optical spectrum of signal filtered by FBG filter; (b) RF clock power versus CD of nonfiltered signal; (c) RF clock power versus CD of filtered signal; (d) RF clock power ratio versus CD.



## 5.1 CD Monitoring Based on RF Tone Power Ratio Measurement

---

and (c) show the relative RF clock tone power as a function of CD for non-filtered and filtered 38-Gbit/s NRZ-DQPSK signals, respectively. Different DGD values (0, 10 and 20 ps) were introduced by a first-order PMD emulator. It is observed that the RF clock power is affected by both CD and DGD. There will be measurement errors if the DGD effect is not eliminated. Fig.5.3(d) shows the RF clock tone power ratio of non-filtered and filtered NRZ-DQPSK signal as a function of CD under different DGD values. The clock power ratio increases with CD and is not affected by DGD effects. The CD measurement range is 0~200 ps/nm. Compared with that using RF clock tone as monitoring signal, the dynamic range of monitoring signal is increased by 20% and the average sensitivity of CD measurement is improved to 0.15 dB/(ps/nm). Moreover, as the power ratio is used as monitoring signal, the measurement results are independent on the optical power of received signal.

The proposed CD monitoring method is also applicable on other modulation formats such as NRZ-D8PSK. Fig.5.4(a) shows the simulated optical spectrum of a 57-Gb/s NRZ-D8PSK signal filtered by an FBG centered at optical carrier. Fig.5.4(b) and (c) show the relative RF clock tone power as a function of CD for non-filtered and filtered 57-Gbit/s NRZ-D8PSK signals, respectively. Different DGD values (0, 10 and 20 ps) were introduced by a first-order PMD emulator. In absence of FBG filter, DGD affects the clock tone power and may introduce error on CD measurement. Fig.5.4(d) shows the clock tone power ratio of non-filtered and filtered NRZ-D8PSK signal versus CD. It is observed that the clock ratio increases with CD and is not affected by DGD values. Simulation results show that the CD measurement range for 38-Gb/s NRZ-DQPSK is 0~200 ps/nm.

The center wavelength of FBG filter may shift from the original value under various environment effects, which may induce RF power ratio changing and errors on CD measurement. Fig.5.5(a) shows the simulated RF clock power ratio change as a

## 5.1 CD Monitoring Based on RF Tone Power Ratio Measurement

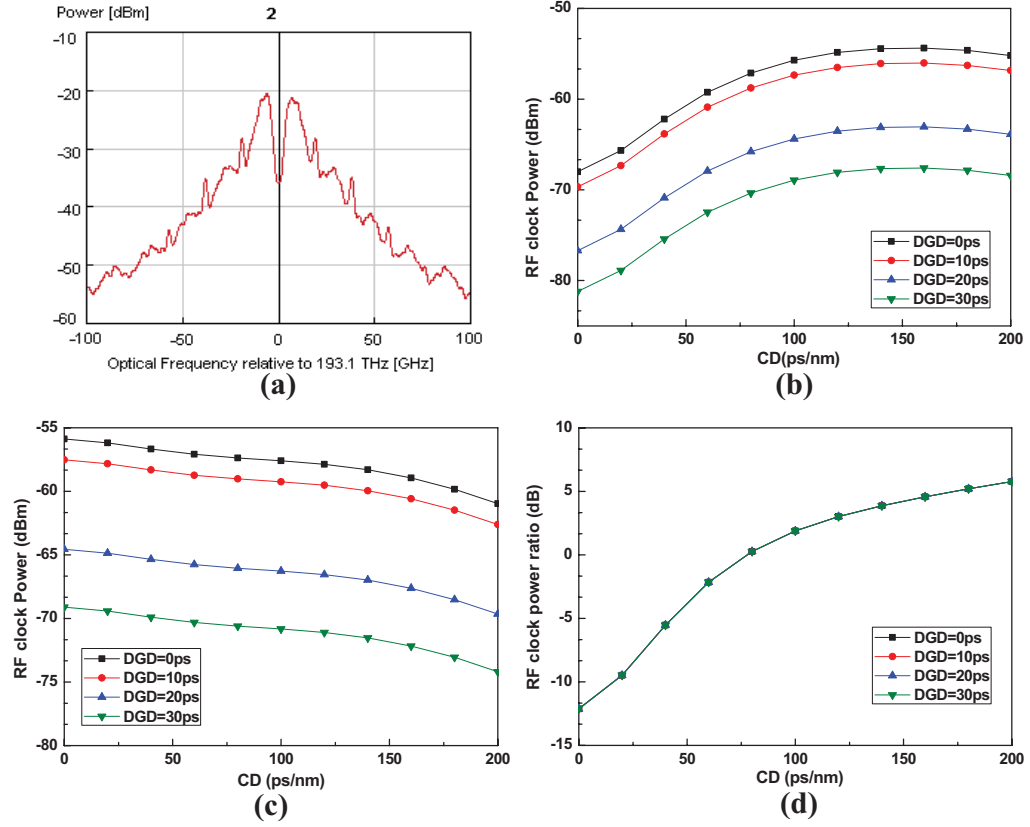


Figure 5.4: Simulation results of 57-Gbit/s NRZ-D8PSK (a) optical spectrum of signal filtered by FBG filter; (b) RF clock power versus CD of non-filtered signal; (c) RF clock power versus CD of filtered signal; (d) RF clock power ratio versus CD.

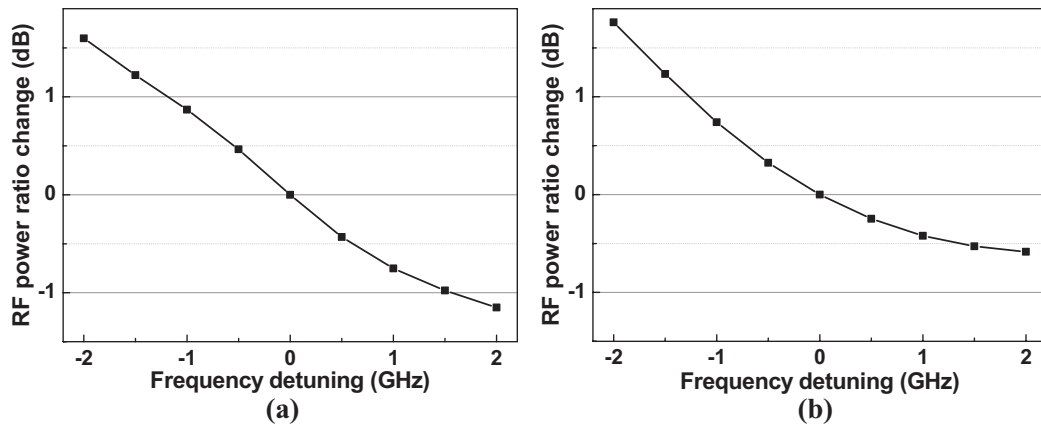


Figure 5.5: Simulated RF clock power ratio change as a function of FBG frequency detuning in (a) 38-Gbit/s NRZ-DQPSK and (b) 57-Gbit/s NRZ-D8PSK systems.

## 5.1 CD Monitoring Based on RF Tone Power Ratio Measurement

---

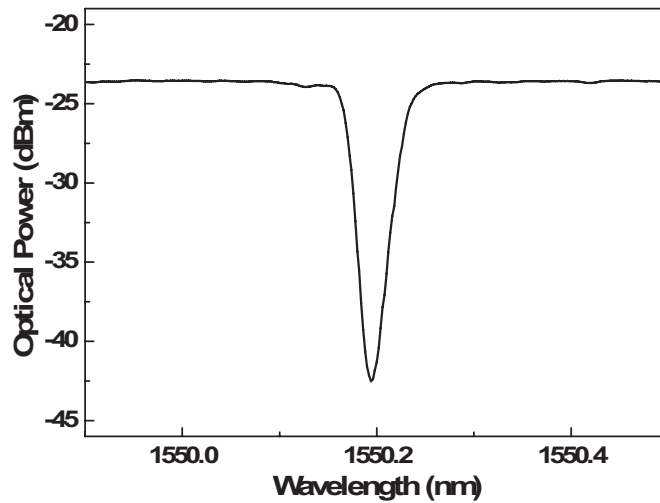


Figure 5.6: Transmission spectrum of fiber Bragg grating.

function of FBG frequency detuning in 38-Gbit/s NRZ-DQPSK. It is observed that the frequency detuning results in changes of RF clock power. RF clock power ratio change is less than 1.6 dB when the frequency detuning in the range of -2 GHz~2 GHz. If the frequency detuning is less than 1 GHz, the power ratio change is smaller than 0.9 dB. Fig.5.5(b) shows the effect of FBG frequency detuning on RF clock power ratio in 57-Gbit/s NRZ-D8PSK systems. The RF clock power ratio change is less than 1.8 dB when the frequency detuning in the range of -2 GHz~2 GHz.

Fig.5.6 shows the transmission spectrum of the FBG used in the CD monitoring scheme. The FBG filter centered at 1550.2 nm has a bandwidth of 0.06 nm and reflection of 15 dB. Fig.5.7(a) shows the measured optical spectrum (with resolution of 0.01 nm) of a 38-Gbit/s NRZ-DQPSK signal filtered by an FBG notch filter. The optical component at the carrier was filtered out by an FBG notch filter. The filtering induces distortion to the original signal. By choosing an FBG with optimal bandwidth and reflection, the RF clock tone can be regenerated in the back-to-back case and decreases with CD when transmitting through fiber links and optical components. Fig.5.7(b) shows experimental result of relative RF clock tone power as a function of CD in 38-

## 5.1 CD Monitoring Based on RF Tone Power Ratio Measurement

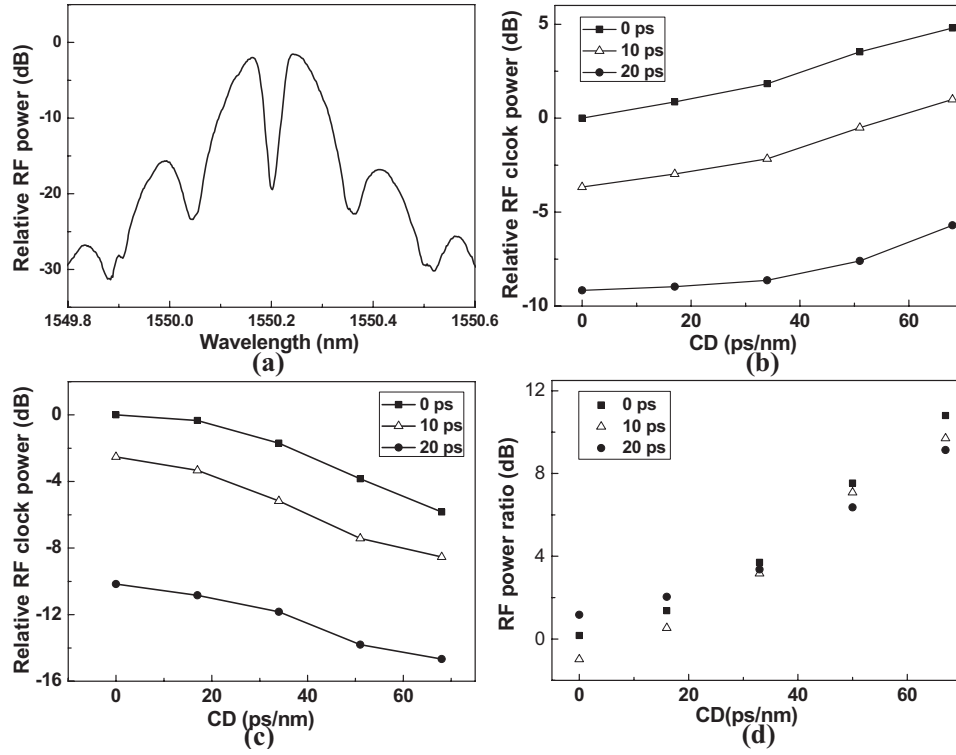


Figure 5.7: Experimental results of 38-Gbit/s NRZ-DQPSK (a) optical spectrum of signal filtered by FBG filter; (b) RF clock power versus CD of nonfiltered signal; (c) RF clock power versus CD of filtered signal; (d) RF clock power ratio versus CD.

## 5.1 CD Monitoring Based on RF Tone Power Ratio Measurement

---

Gbit/s NRZ-DQPSK system in the absence of FBG filter. Different DGD values (0, 10 and 20 ps) were introduced by a first-order PMD emulator. The RF clock power increases with CD, which is due to the chromatic dispersion induces phase difference between the sidebands and the beating term is regenerated. It is observed that DGD affects the clock tone power and may introduce errors on CD measurement. Fig.5.7(c) shows the measured relative RF clock power versus CD at different DGD values when the signal is filtered by an FBG notch filter placed at the carrier wavelength. The received clock power decreases with both CD and DGD values. It is noted that the PMD induced RF power fading for the filtered and non-filtered signals are the same. Therefore, by taking the ratio of the two RF clock powers, the PMD effects can be eliminated. Fig.5.7(d) shows the RF clock tone power ratio of non-filtered and filtered NRZ-DQPSK signal as a function of CD under different DGD values. It is observed that the clock power ratio increases with CD and is almost not affected by DGD effects. Compared with that using RF clock tone as monitoring signal, the dynamic range of monitoring signal is increased by 67% and the average sensitivity of CD measurement is improved to 0.14 dB/(ps/nm).

The measurement sensitivity improvement is larger than that in the simulation result. This is because in the absence of FBG filter, the “slope” of RF power changing is larger in the small CD range (0~10 ps/nm). However, it is difficult to achieve zero CD in the experiment. There is residual CD in the system although no SMF or DCF is added in the transmission link. Therefore, in the absence of FBG filter, the dynamic range of RF clock power in the experiment is not as large as that in the simulation. On the other hand, if the signal is filtered by FBG filter, the RF power change is not large in the small CD range (0~10 ps/nm). The dynamic range is not affected much by the residual CD. Therefore, the dynamic range of RF clock power ratio and CD measurement sensitivity improvement is larger in the experiment.

## 5.1 CD Monitoring Based on RF Tone Power Ratio Measurement

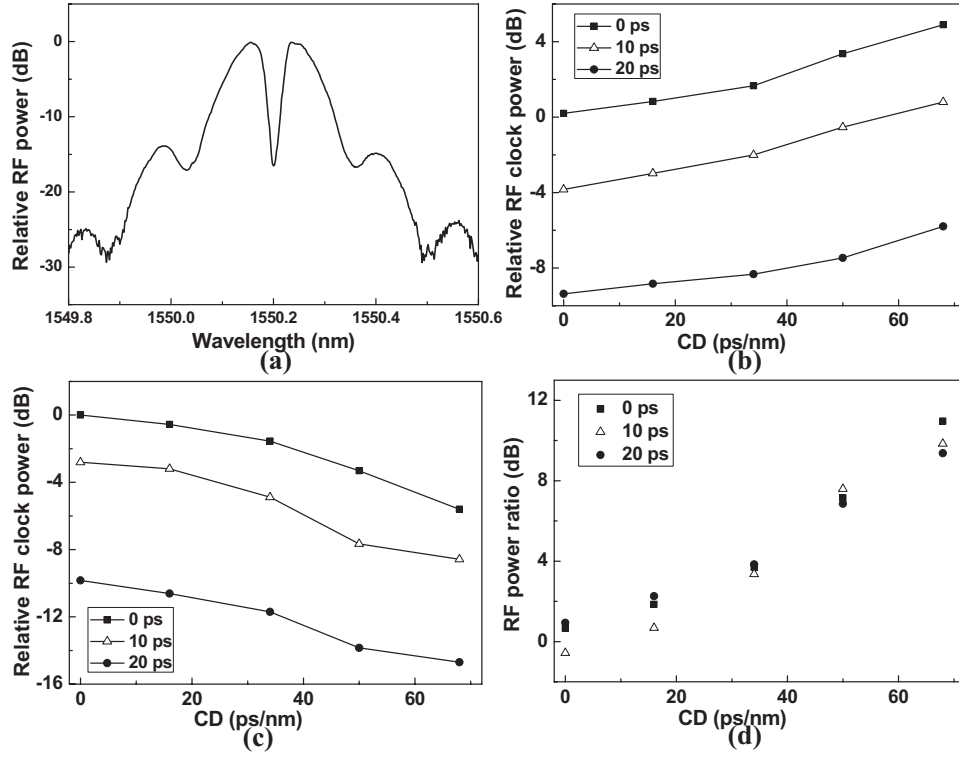


Figure 5.8: Experimental results of 57-Gbit/s NRZ-D8PSK (a) optical spectrum of signal filtered by FBG filter; (b) RF clock power versus CD of non-filtered signal; (c) RF clock power versus CD of filtered signal; (d) RF clock power ratio versus CD.

## 5.1 CD Monitoring Based on RF Tone Power Ratio Measurement

---

The proposed CD monitoring method is also applicable on other modulation formats such as NRZ-D8PSK. Fig.5.8(a) shows the measured optical spectrum of a 57-Gbit/s NRZ-D8PSK signal filtered by an FBG notch filter, the same as that used in the NRZ-DQPSK system. Fig.5.8(b) and (c) shows the relative RF clock power as function of CD for non-filtered and filtered NRZ-D8PSK signals, respectively. Fig.5.8(d) shows the RF clock power ratio as function of CD under different DGD values. For various DGD values (0, 10 and 20 ps), the amplitude of the monitoring signal is almost the same. Therefore, the proposed method is efficient for PMD-insensitive CD monitoring in D8PSK system.

### 5.1.4 FBG Filter Centered at 10-GHz Away From Carrier

We propose and demonstrate a technique on CD monitoring without the effects of PMD and received power. Both simulation and experimental results show that the proposed method is efficient for measuring CD in 57-Gb/s NRZ differential 8-level phase-shift keying (D8PSK) and 38-Gb/s NRZ differential quadrature phase-shift keying (DQPSK) transmission systems. As the 10-GHz RF power ratio is used as monitoring signal, the CD measurement range is increased to 0~500 ps/nm.

Fig.5.9(a) shows the optical spectrum (with resolution of 0.01 nm) of a 38-Gbit/s NRZ-DQPSK signal in one of monitoring branches. The signal is filtered by a narrow band FBG notch filter placed at 10-GHz away from carrier. Therefore, the received 10-GHz RF tone power decreases with DGD and is insensitive to CD. Fig.5.9(b) shows simulation and experimental results of 10-GHz RF tone power and power ratio versus CD in 38-Gb/s NRZ-DQPSK system. Several DGD values (0, 20 and 40 ps) were introduced by a first-order PMD emulator. It is observed that DGD affects the RF tone power much in absence of FBG filter, which may result in CD measurement errors. If one of the sidebands is filtered out, chromatic dispersion induces phase shift to the

## 5.1 CD Monitoring Based on RF Tone Power Ratio Measurement

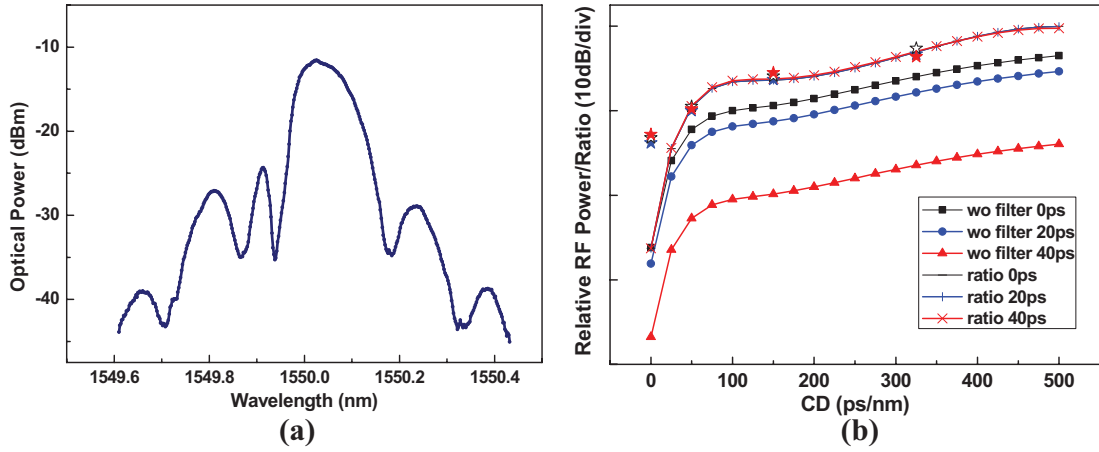


Figure 5.9: 38-Gbit/s DQPSK (a) optical spectrum of signal filtered by FBG; (b) Relative 10-GHz RF power versus CD. (lines for simulation; stars for experiment)

RF tone while the amplitude of RF tone is constant. Therefore, the RF tone power is insensitive to CD. As PMD induced RF power fading for the filtered and non-filtered signals are the same, by taking the ratio of the two RF tone powers, the measurement errors induced by PMD can be eliminated and accurate CD monitoring can be achieved. Fig.5.9(b) shows that the 10-GHz RF tone power ratios are not affected by PMD effects. The experimental results also show that PMD does not affect the CD measurement results by using 10-GHz RF tone power ratio as monitoring signal. CD measurement range for 38-Gbit/s NRZ-DQPSK is 0~500 ps/nm.

The proposed CD monitoring method is applicable on other modulation formats such as OOK and NRZ-DQPSK. Fig.5.10(a) shows measured optical spectrum of 57-Gbit/s NRZ-D8PSK signal which is filtered by a narrow band FBG filter located at 10-GHz away from the carrier. Fig.5.10(b) shows the simulation and experimental results of the 10-GHz RF tone power and power ratio versus CD in NRZ-DQPSK transmission system. It is observed that the RF power ratio increases with CD and is almost not affected by PMD effects.



## 5.2 CD Monitoring Based on Amplitude Ratio in Delay-tap Sampling Plot

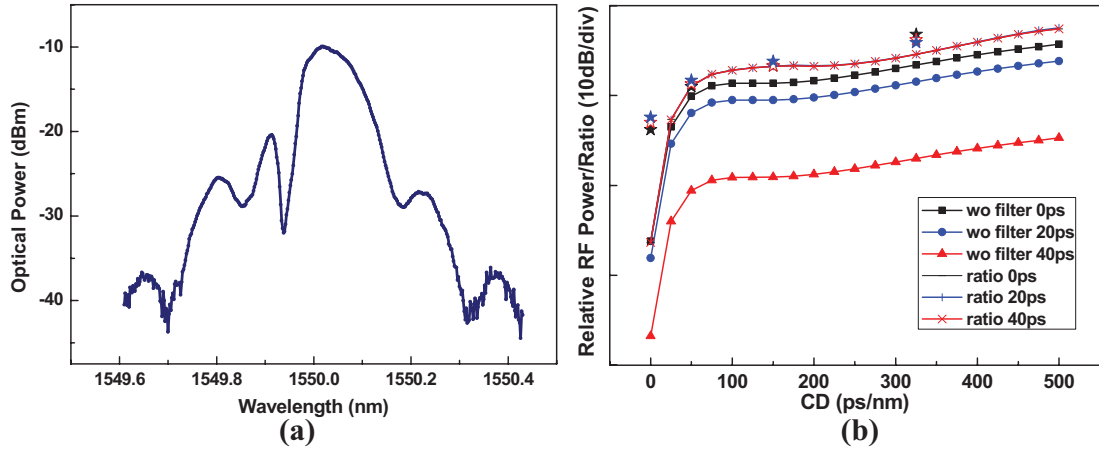


Figure 5.10: 57-Gbit/s D8PSK (a) optical spectrum of 57-Gb/s NRZ-D8PSK signal filtered by FBG; (b) Relative 10-GHz RF power versus CD. (lines for simulation; stars for experiment)

Compared with that using RF clock as monitoring signal, the CD measurement range is increased by 3.6 times and the required bandwidth of the photodetector is much lower. Moreover, as the power ratio is used as monitoring signal, the measurement results are independent on the optical power of received signal. It is noted that the monitoring branch which is filtered by FBG can be used to achieve CD-insensitive PMD monitoring. Therefore, CD and PMD can be measured simultaneously and independently using our proposed method.

## 5.2 CD Monitoring Based on Amplitude Ratio in Delay-tap Sampling Plot

Asynchronous delay-tap sampling was reported [137, 138]. This method uses a delay-tap line to get a pair of data in one sampling, one without delay and the other one with delay. Multiple impairment measurements as well as signal quality are extracted from

## 5.2 CD Monitoring Based on Amplitude Ratio in Delay-tap Sampling Plot

---

the two dimensional histogram of signal. Asymmetry ratio of delay-tap sampling is proposed on residual CD monitoring for CSRZ differential quadrature phase-shift keying (DQPSK) signal [140]. However, the reported asynchronous delay-tap sampling method is not sensitive in the small CD region.

We propose an amplitude ratio in delay-tap sampling plot, which can measure the residual CD in low CD region. The measurement range is 0~75 ps/nm for 40-Gbit/s DQPSK and 60-Gbit/s differential eight phase-shift keying (D8PSK) systems. The simulated results in VPItransmissionMaker 7.0 show that the amplitude ratio decreases from 1 to 0.58, from 0.7 to 0.45 and from 0.73 to 0.53 when residual CD change from 0 to 75 ps/nm in 40-Gbit/s 50% return-to-zero (RZ) DQPSK, 67% carrier-suppressed return-to-zero (CSRZ) DQPSK and 60-Gbit/s 50% RZ D8PSK systems, respectively. Our proposed CD measurement method is not affected by the received optical power. Besides, no modification on the transmitter or receiver is required. The proposed technique is a simple and cost effective scheme.

### 5.2.1 Principle of Delay-tap Sampling Plot

Asynchronous delay-tap sampling is a technique which provides the information of waveform. Compared with eye diagram, which also express the waveform information of signals, delay-tap sampling has two advantages, which are low sampling rate and no synchronization. Fig.5.11(a) shows the schematic graph for generating delay-tap sampling pairs in a demodulated RZ DQPSK signal. Each point in the delay-tap sampling plot comprises two parameters (x and y). The time delay between x and y is a constant,  $\Delta t$ . It is found that the sensitivities of impairments are different when time delay is changed. The sampling time,  $T_s$ , can be many orders of bit period. Therefore, the sampling rate can be decreased dramatically and the CD monitoring scheme will be simple and cost effective. Fig.5.11(b) shows the demodulated eye diagram of 50%

## 5.2 CD Monitoring Based on Amplitude Ratio in Delay-tap Sampling Plot

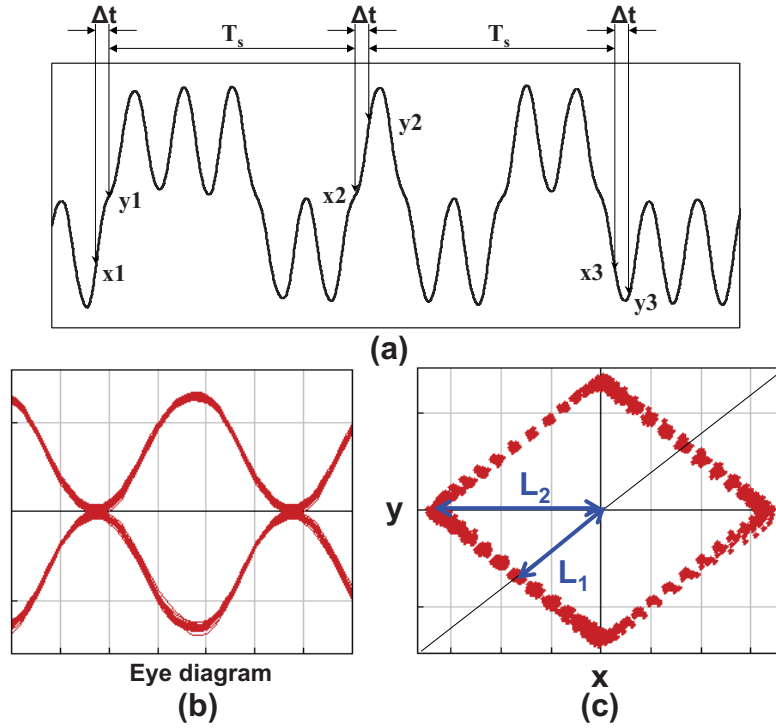


Figure 5.11: Principle of delay-tap asynchronous sampling for RZ DQPSK signal. (a) waveforms in time domain; (b) eye diagram; (c) delay-tap plot ( $\Delta t = \text{symbol period}/2$ ).

$T_s$ : sampling period;  $\Delta t$ : time offset.

## 5.2 CD Monitoring Based on Amplitude Ratio in Delay-tap Sampling Plot

---

RZ DQPSK signal. Fig.5.11(c) shows the asynchronous delay-tap sampling plot at a time delay of half symbol period ( $B/2$ ). Both graphs are in back-to-back case and no distortion is induced.

We note that by choosing half symbol period as the time delay, the plot distortion induced by chromatic dispersion is the largest. In all cases of our paper, the tap delay for CD monitoring is half symbol period. We can utilize the delay-tap sampling plot distortion induced by CD to monitor residual dispersion in the systems. In order to quantification the information in the delay-tap plot, we define an amplitude ratio  $\alpha$ :

$$\alpha = L_1/L_2, \quad (5.1)$$

where  $L_1$  is the distance between the center point and the cross point of diagonal line  $y=x$  and the delay-tap sampling plot in the third quadrant; and  $L_2$  is the distance between the center point and the cross point of horizon line  $y=0$  and the delay-tap sampling plot, shown in Fig.5.11(c). The simulated results show that amplitude ratio obtained from the delay-tap sampling plot decreases monotonously as the residual CD increases and can be used as a CD monitoring signal. This technique does not need clock or modification on transmitter/receiver. Therefore, it is a simple and cost effective monitoring method.

### 5.2.2 Results and Discussions

The system setup for dispersion monitoring based on asynchronous delay-tap sampling is shown in Fig.5.12. 40-Gbit/s 50% RZ DQPSK/67% CSRZ DQPSK signal is generated by a transmitter. CD is introduced by a piece of single mode fiber (SMF). After demodulation, the received electrical signal is split equally into two branches (X and Y) and one of the branches is delayed by half symbol period time ( $B/2$ ). The obtained sample pairs are delay-tap sampling signals which reflect the waveform distortion in-

## 5.2 CD Monitoring Based on Amplitude Ratio in Delay-tap Sampling Plot

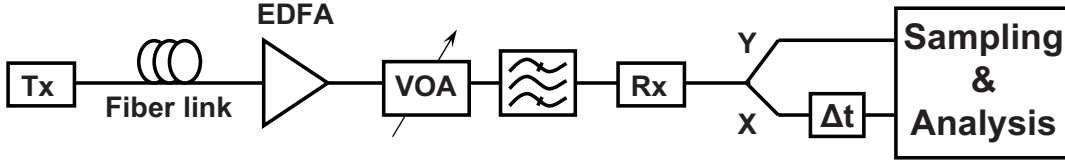


Figure 5.12: System setup for dispersion monitoring based on delay-tap sampling.  $T_X$ : transmitter; EDFA: Erbium doped fiber amplifier.

formation induced by various impairments along transmission. The amplitude ratio, which is obtained from the delay-tap sampling plot, decreases monotonously as CD increases and can be used as a CD monitoring signal. As amplitude ratio is the monitoring signal, the measurement result is not affected by received optical power. By tuning the bias of Mach-Zehnder modulator (MZM) in the transmitter, RZ DQPSK signal with different duty cycle can be generated. The effectiveness of our proposed method is demonstrated through simulation for 40-Gbit/s 50% RZ DQPSK, 67% CSRZ DQPSK and 60-Gbit/s D8PSK signals.

Fig.5.13(a) and (d) show the demodulated eye diagram and delay-tap sampling plot of 67% CSRZ DQPSK signal in the back-to-back case, respectively. It is observed that the demodulated eye diagram is very clear and the delay-tap sampling plot is symmetry in this case. The amplitude ratio of delay-tap sampling plot is relative large, which is due to the fact that the waveform of 67% CSRZ DQPSK signal is not distorted by the impairments. Fig. 5.13(c) and (f) show the demodulated eye diagram and delay-tap sampling plot when dispersion is 75 ps/nm. It is observed that the demodulated eye diagram is distorted by CD; however, it is difficult to quantify the residual CD value from the eye diagram. On the other hand, the amplitude ratio in the delay-tap sampling plot decreases from 1 to 0.58. Therefore, amplitude ratio is quite sensitive to dispersion and can be used to monitor residual CD in the systems with high bit rate.

## 5.2 CD Monitoring Based on Amplitude Ratio in Delay-tap Sampling Plot

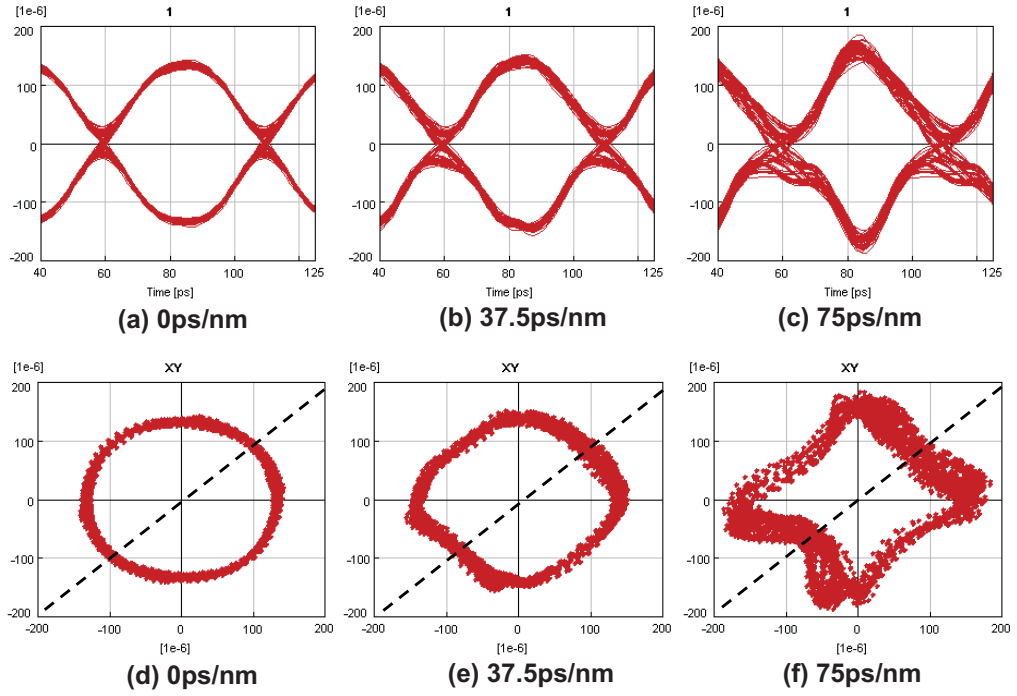


Figure 5.13: 40-Gbit/s 67% CSRZ DQPSK signal (a)-(c) eye diagrams and (d)-(f) delay-tap plots with different residual CD.

## 5.2 CD Monitoring Based on Amplitude Ratio in Delay-tap Sampling Plot

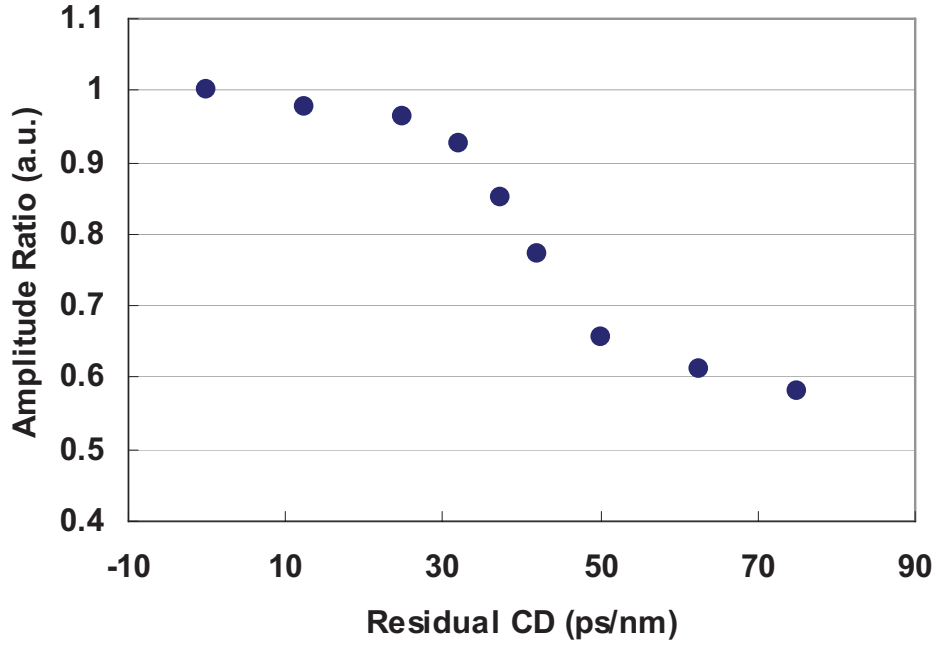


Figure 5.14: Simulated amplitude ratio in delay-tap sampling plot as a function of chromatic dispersion. 40-Gbit/s 67% CSRZ DQPSK signal.

Comparing Fig.5.13(a) with Fig.5.13(c), it is observed that the demodulated waveform of 67% CSRZ DQPSK signal is narrowed by dispersion. In the delay-tap plot, the cross point of diagonal line  $y=x$  and the delay-tap plot in the third quadrant is related to the sample time when both  $x$  and  $y$  are the middle points, which are between minimum and zero amplitude in the eye diagram. As the waveform is narrowed by dispersion, the amplitude of middle point is smaller than that in the back-to-back case, due to decreasing of  $L_1$ . The cross point of horizon line  $y=0$  and the delay-tap plot is related to the sampling time when  $x$  is minimum and  $y$  is zero in the eye diagram. From Fig.5.13(a) and (c), the minimum amplitude has almost no change, which corresponding to no change of  $L_2$ . Considering both  $L_1$  and  $L_2$ , CD induced distortion decreases the amplitude ratio. As the ratio of amplitude is used as a monitoring signal, the measurement result is not affected by received optical power.

## 5.2 CD Monitoring Based on Amplitude Ratio in Delay-tap Sampling Plot

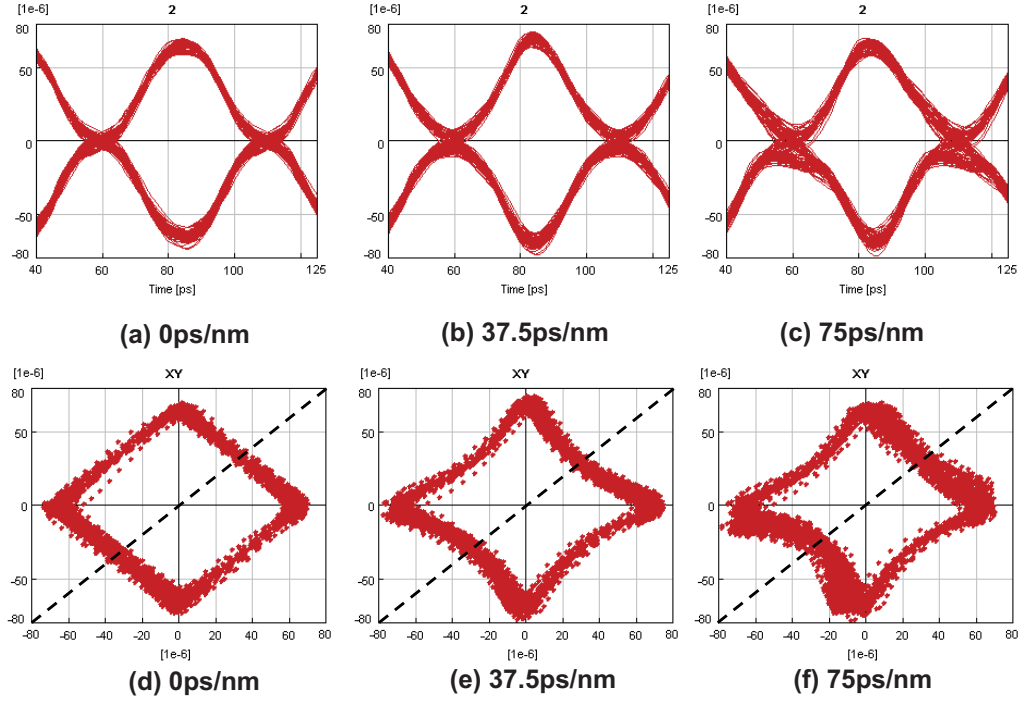


Figure 5.15: 40-Gbit/s 50% RZ DQPSK signal(a)-(c) eye diagrams and (d)-(f) delay-tap plots with different residual CD.

Amplitude ratio of delay-tap sampling plot as a function of chromatic dispersion for 40-Gbit/s CSRZ DQPSK signal is shown in Fig.5.14. The amplitude ratio varies from 1 to 0.58 as the residual CD changes from 0 to 75 ps/nm, which is larger than the technique proposed in [140]. It is observed that the amplitude ratio decreases monotonously with residual CD, which indicates that the proposed method is efficient on CD monitoring for CSRZ DQPSK signal.

Amplitude ratio of delay-tap sampling plot can also be applied to 50% RZ DQPSK system to monitor residual CD. By tuning the bias of MZ modulator in the transmitter, 50% RZ DQPSK can be generated. Fig.5.15 shows the delay-tap sampling plots of 40-Gbit/s 50% RZ DQPSK signal with various CD values. Fig. 5(a) shows the delay-tap plot in the back-to-back case. It is different from that of 67% CSRZ DQPSK as



## 5.2 CD Monitoring Based on Amplitude Ratio in Delay-tap Sampling Plot

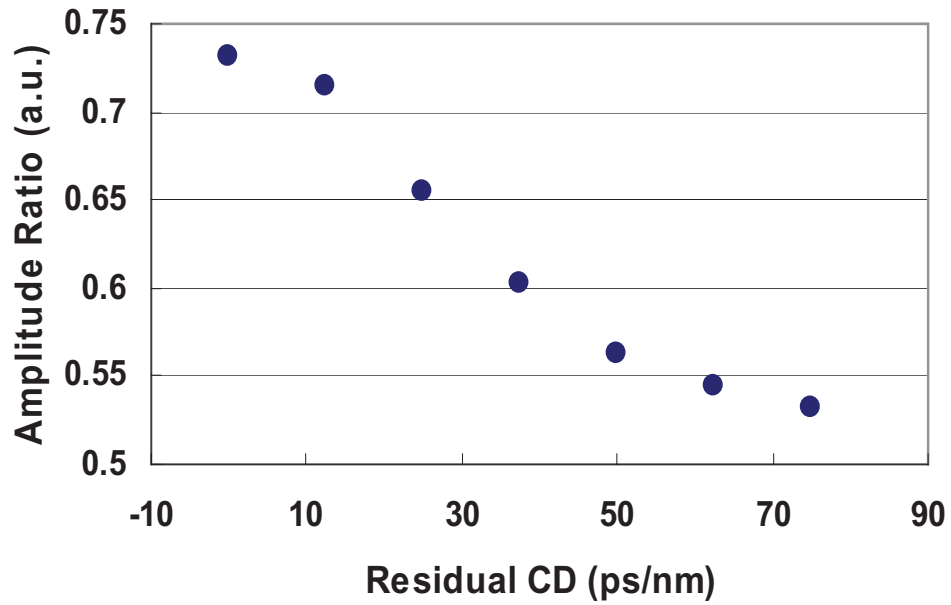


Figure 5.16: Simulated amplitude ratio in delay-tap sampling plot as a function of chromatic dispersion. 40-Gbit/s 50% RZ DQPSK signal.

the pulse width of 50% RZ DQPSK is narrower. Fig.5.15(d)-(f) show the delay-tap sampling plots with a CD of 0 ps/nm, 37.5 ps/nm and 75 ps/nm. It can be seen that the amplitude ratio decreases as CD increases. Therefore, amplitude ratio of asynchronous delay-tap sampling plot can be utilized to monitor residual CD in 50% RZ DQPSK system.

Fig.5.16 shows the amplitude ratio as a function of chromatic dispersion in 40-Gbit/s 50% RZ DQPSK system. As the pulse width of 50% RZ DQPSK is narrow, the maximum value of amplitude ratio is 0.7, which decreases to 0.45 when the residual CD increases to 75 ps/nm. It is observed that the amplitude ratio of asynchronous delay-tap sampling plot decreases monotonously with residual CD, which indicates that the proposed method is efficient on CD monitoring for 50% RZ DQPSK signal.

The simulation results show that the proposed amplitude ratio in delay-tap sampling plot is also efficient on residual CD monitoring in 50% RZ D8PSK system. By

## 5.2 CD Monitoring Based on Amplitude Ratio in Delay-tap Sampling Plot

---

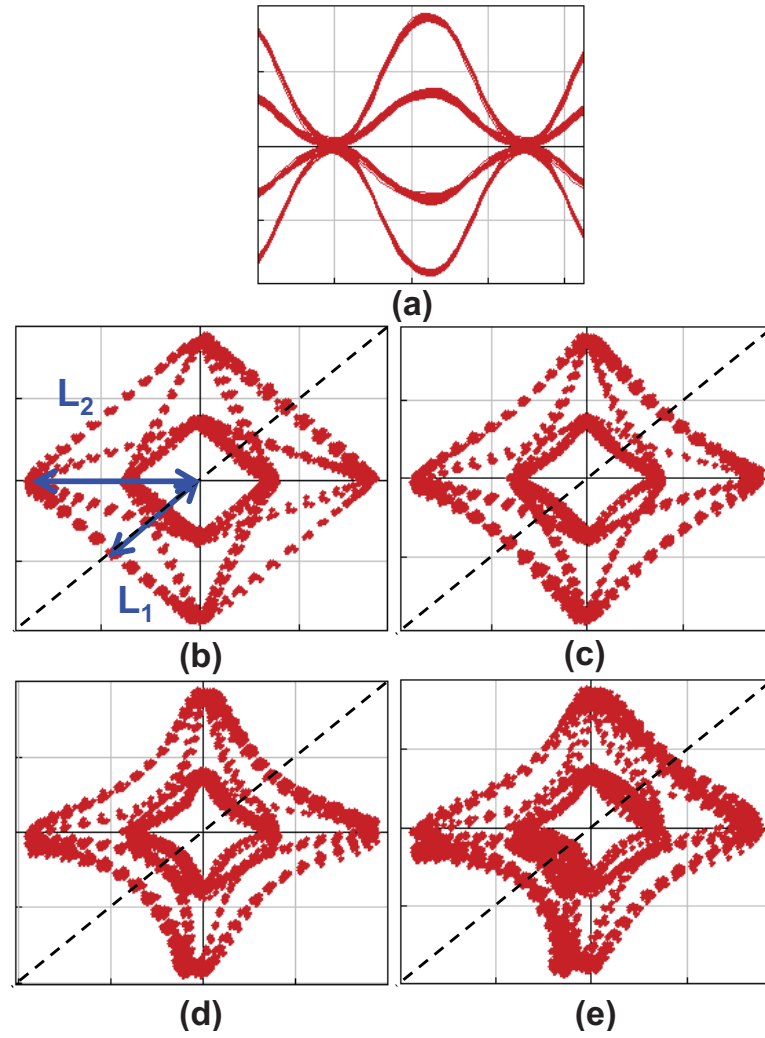


Figure 5.17: 60-Gbit/s 50% RZ D8PSK signal(a) eye diagrams and (b)-(e) delay-tap plots with different residual CD.

### 5.3 Conclusions

---

using an additional phase modulator which is driven by 20-Gbit/s PRBS data, 60-Gbit/s 50% RZ D8PSK signal can be obtained. Fig.5.17(a) show the eye diagram of 50% RZ D8PSK signal in absence of CD. It is observed that the eye diagram has two levels of amplitude. The delay-tap sampling plots with different residual CD are shown in Fig.5.17(b)-(e), which also show two levels of amplitude. Comparing with the delay-tap sampling plots of DQPSK signals, that of D8PSK signals is complicated. Whereas, the amplitude ratio of outer ring in the asynchronous delay-tap sampling plots, shown in Fig. 5.17(b), can be used to monitor the residual CD values. It is observed that  $L_1$  decreases monotonously as the residual CD increases; while  $L_2$  keeps constant. Therefore, the amplitude ratio ( $\alpha = L_1/L_2$ ) can be used as a CD monitoring signal in D8PSK system.

Fig.5.18 shows the amplitude ratio as a function of chromatic dispersion in 60-Gbit/s 50% RZ D8PSK system. The maximum value of amplitude ratio is 0.73, which is decreased to 0.53 when the residual CD increases to 75 ps/nm. It is observed that the amplitude ratio of asynchronous delay-tap sampling plot decreases monotonously with residual CD, which indicates that the proposed method is also efficient on residual CD monitoring for 50% RZ D8PSK signal.

### 5.3 Conclusions

Three CD monitoring methods are demonstrated in this chapter. Method 1 is based on RF power ratio measurement and optical filtering. By placing the FBG filter at the carrier wavelength, large measurement sensitivity can be achieved. However, the CD measurement range is only 0~200 ps/nm in 57-Gbit/s D8PSK system. In method 2, an FBG filter is centered at 10 GHz from the carrier, and the CD measurement range increases to 0~500 ps/nm in 57-Gbit/s D8PSK system. However, the measurement

### 5.3 Conclusions

---

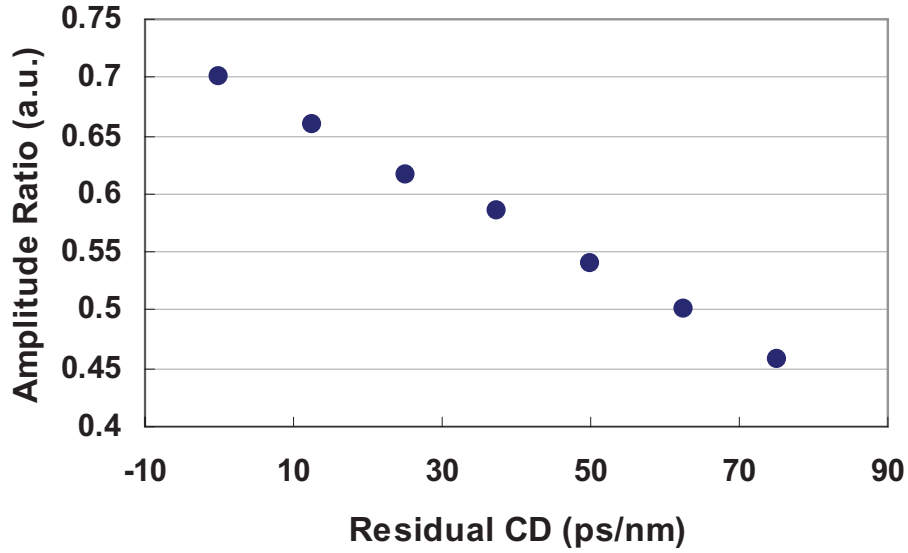


Figure 5.18: Simulated amplitude ratio in delay-tap sampling plot as a function of chromatic dispersion. 60-Gbit/s 55% RZ D8PSK signal.

sensitivity is not as good as method 1. Both simulation and experiments show that the proposed methods are efficient for eliminating PMD effects on RF power ratio.

Another CD monitoring method is proposed by using amplitude ratio of asynchronous delay-tap sampling plot. The simulated results show that the propose method is efficient on residual CD measurement in 40-Gbit/s CSRZ DQPSK, 50% RZ DQPSK and 60-Gbit/s 50% RZ D8PSK systems. The measurement results are not affected by received optical power. Besides, the proposed scheme dose not needs clock or modification on transmitter/receiver. Therefore, it is a simple and cost effective method.

Among the three methods, method 1 and method 2 are insensitive to PMD and have larger CD measurement range (0~200 and 0~500 ps/nm in 40-Gbit/s DQPSK system for method1 and method 2, respectively). Method 2 has larger measurement range than method 1 as lower frequency (10 GHz) RF tone power ratio is used as monitoring signal. Compared with the first two methods, method 3 has limited measurement range (less than 100 ps/nm in 40-Gbit/s DQPSK system). Besides, the CD monitoring

### 5.3 Conclusions

---

results may be affected by other impairment effects, such as PMD and OSNR. However, the measurement sensitivity of method 3 is better.

## **Chapter 6**

# **Suppression of Signal Fluctuation in BOTDA Sensing System**

Optical fiber sensors are widely used as they are flexible, immune to electromagnetic interference, and applicable in many environments. The stimulated Brillouin scattering (SBS) based fiber sensor is capable of sensing temperature and strain over relative long distances by monitoring the changes of Brillouin frequency shift. However, since the SBS is a polarization sensitive process, the polarization sensitivity remains a key problem for SBS based distributed fiber sensing system because it will induce the polarization noise and reduce the signal to noise ratio the of the sensor [91–94].

Several schemes have been proposed to overcome the polarization induced fluctuation. A computer-controlled polarization controller has been used to eliminate the polarization noises in a SBS-based sensor system [93]. The method has following disadvantages: 1) increasing measurement time significantly by finding the optimal polarization state, or averaging the performance over time; 2) requirement of an additional active component. A polarization switch (PSW) which can alternatively generate two orthogonal polarization states is proposed [95]. However, PSW is an active component

## 6.1 Distributed Sensing System Based on SBS

---

and it requires perfectly linear input polarization. A new configuration is reported to eliminate the noise by using passive polarization scrambler that consists of a highly unbalanced Mach-Zehnder interferometer [141]. However, this polarization scrambler cannot be operated in pulsed case.

In this chapter, we demonstrate a novel method to suppress the polarization sensitivity in BOTDA distributed sensing system. In our scheme, the polarization diversity is introduced on the pulsed pump wave. A PBS splits the pump wave into two beams with orthogonal polarization states and one of the beams is delayed by a time related to the pulse width. After recombining of the two waves, the DOP decreases from 95% to only 5% and the polarization induced strain fluctuation is suppressed to  $\pm 50 \mu\epsilon$  from  $\pm 300 \mu\epsilon$ . The strain measurement time in the proposed scheme is 3s which is the same as that in the system without polarization diversity scheme.

## 6.1 Distributed Sensing System Based on SBS

Stimulated Brillouin scattering (SBS) occurs at relatively low power compare with stimulated Raman scattering (SRS). If the spacing of two counter propagating channels are in the Brillouin gain spectrum and the power of the two channels are above the Brillouin threshold, SBS occurs and a power is transferred from high frequencies to low frequencies. The refractive index of optical fiber can be changed by the environment (temperature and strain), and the Brillouin shift  $\Omega_B$  of the fiber is also changed. Thus, SBS effect in the optical fiber can be used in distributed temperature or strain sensing system.

Brillouin scattering based distributed fiber sensor technology is a promising technique for distributed temperature and strain monitoring as it is flexible, immune to electromagnetic interference, and applicable in many environments. In the Brillouin

## 6.1 Distributed Sensing System Based on SBS

---

optical correlation domain analysis (BOCDA) sensing system, continuous wave (CW) pump and probe are used. The Brillouin gain spectrum (BGS) can be detected by the correlation between two counter propagating beams. In BOTDA sensing system, pulsed pump and CW probe are used. It is capable of fully distributed measurements along the fiber and the distributed temperature and/or strain can be obtained by monitoring the changes of Brillouin frequency shift  $\Omega_B$ . However, in both of the two kinds sensing system, the system performance is affected by the relative polarization state between the pump and probe waves.

In the BOTDA sensing system, the Brillouin gain and the Brillouin frequency shift  $\Omega_B$  change when the relative polarization state between pump and probe changes. The polarization mismatch induces the reduce of signal-to-noise ratio (SNR) the of the optical sensing system [91–94]. We proposed a polarization diversity scheme on the pulsed pump to suppress the signal fluctuation in the sensing system. This method contains only two PBS and a piece of SMF. The principle of Brillouin Optical Time Domain Analysis based sensing system and proposed polarization diversity scheme on the pump wave are shown in this section.

### 6.1.1 BOTDA Sensing System

Time domain analysis of Stimulated Brillouin Scattering (SBS) in a single-mode fiber involves the interaction between a pulsed pump beam and a counter propagating continuous wave (CW) probe beam at different wavelengths. At any section of the fiber, a power transfer between the pulsed pump and the probe wave occurs if their frequency offset is within the local Brillouin gain spectrum (BGS). The probe wave is modulated by a electro-optic modulator (EOM) which is biased at transmission null point at a frequency close to the Brillouin frequency shift ( $\sim 10.84$  GHz) of the FUT. Compared with the pulsed pump wave which has tens of nanometers width with a repetition rate



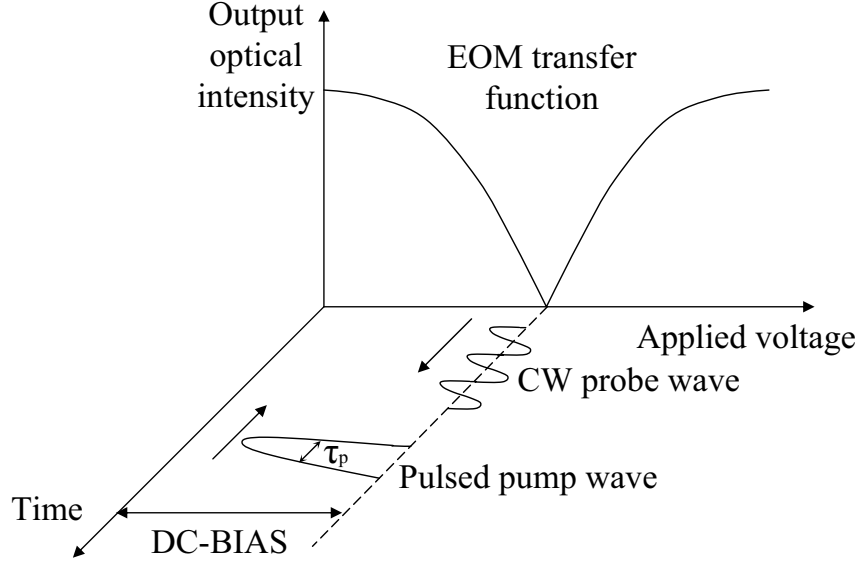


Figure 6.1: EOM transmitted optical intensity as a function of the applied voltage and a function of time.

of tens of microsecond, the probe wave can be assumed to be a continuous wave. In such a system, which has a pulsed pump wave, the spatial resolution highly depends on the pulse width of the pump ( $\tau_p$ ).

Fig.6.1 shows the transmitted intensity of the EOM as a function of the modulation voltage and the time. The EOM is biased at the transmission null point and two sidebands are generated. One of them is within the BGS and serves as a probe wave, the other one will be filtered out by an FBG filter. By scanning the modulation frequency of the probe beam in a frequencies range around the Brillouin shift of the FUT, the BGS can be obtained and the peak frequency ( $\Omega_B$ ) of the BGS signifies the temperature or strain at the location of FUT. In other words, the variation of temperature or strain induces the change of BGS and the location of the peak frequency. For

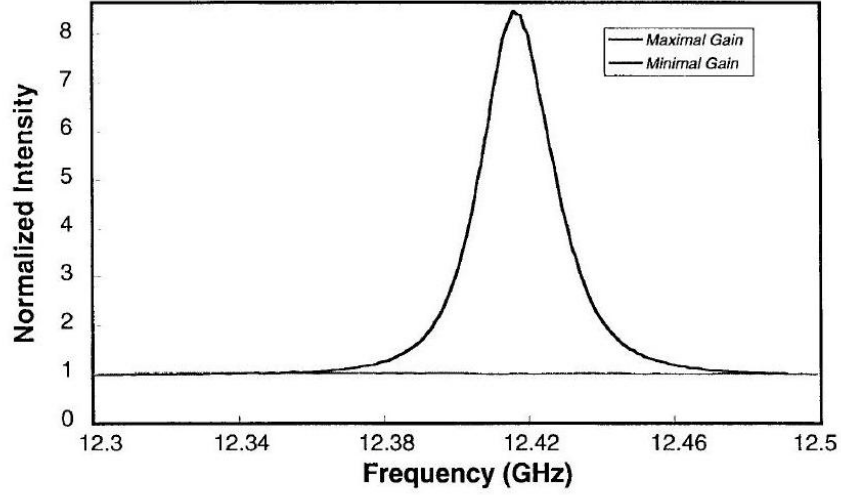


Figure 6.2: Maximum and minimum gain achievable in the measurement of the BGS of a highly birefringent dispersion shifted fiber [92].

temperature measurement, the temperature at any point along the fiber is determined by  $T = T_0 + \alpha(\Omega_B - \Omega_0)$ , where  $T_0$  is reference temperature and  $\alpha$  is temperature sensitivity, assuming the fiber is under normal strain. For strain measurement, the distributed strain is determined by  $\varepsilon = \varepsilon_0 + \beta(\Omega_B - \Omega_0)$ , where  $\varepsilon_0$  is the reference strain and  $\beta$  is the strain sensitivity, assuming the fiber is under constant temperature. The location of the temperature or strain along the FUT can be obtained by measuring the time-of-flight.

### 6.1.2 Polarization Induced Signal Fluctuation in BOTDA Sensing System

SBS is a polarization sensitive process, the relative polarization state between pump and probe wave affects the Brillouin gain. And polarization sensitivity is a key problem for SBS based distributed fiber sensing system. Fig.6.2 shows the measurements of

## 6.2 Polarization Diversity Scheme in Distributed Sensing System

---

Brillouin gain spectrum performed on 140 m of highly birefringent dispersion shifted fiber [92]. The polarizations of the launched waves are linear and parallel to one of the birefringence axis of the fiber. If the polarization states of the two waves are orthogonal, the probe has no gain. On the contrast, if the polarization states of the two waves are parallel, maximum Brillouin gain can be achieved.

The variation of polarization states of pump and probe waves along the fiber will induce changes of Brillouin gain. Moreover, the polarization induced gain fluctuation will introduce errors on detection of the Brillouin shift. Therefore, polarization noise in the fiber reduces the signal to noise ratio of the fiber sensor. In some cases, the polarization induced fluctuation results in errors of the distributed sensing systems. Several schemes have been proposed to overcome the polarization induced fluctuation in BOTDA sensing systems [91–94].

## 6.2 Polarization Diversity Scheme in Distributed Sensing System

In the system without polarization diversity scheme, Brillouin gain varies with the relative polarization state between the pulsed pump and CW probe waves. For the best polarization state (when the SOP of the probe wave is the same as that of pump wave), the probe has a maximal gain, as shown in Fig.6.3(a). And for the worst polarization state (when the SOP of the probe wave is orthogonal to that of pump wave), the probe beam has no gain, as shown in Fig.6.3(b).

In the proposed system, the pump pulse is divided into two orthogonal sub-pulses. Therefore, both orthogonal polarization components of the probe wave will be efficiently amplified by the sub-pulses of the pump. Thus the SBS gain will be polarization-insensitive and the Brillouin frequency shift  $\Omega_B$  can be detected accu-

## 6.2 Polarization Diversity Scheme in Distributed Sensing System

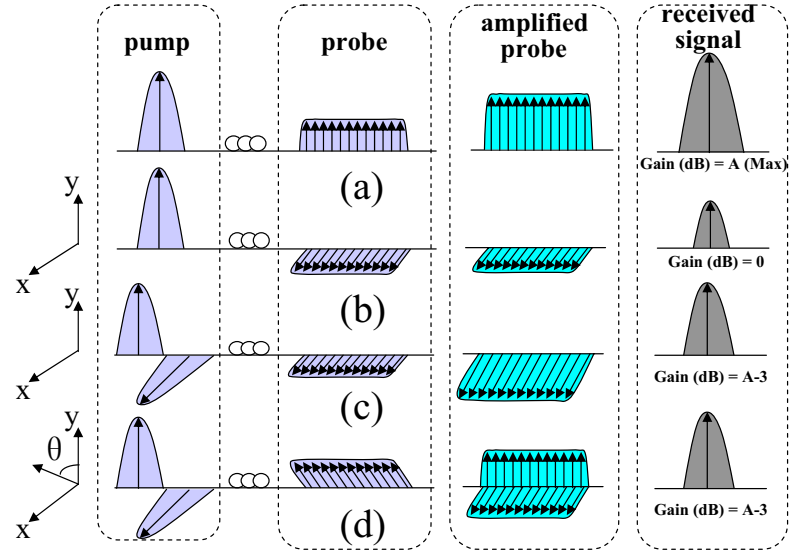


Figure 6.3: The fluctuations of Brillouin gain due to the relative polarization state between pump and probe waves. (a) The probe wave is parallel to the pump wave, without polarization diversity. (b) The probe wave is orthogonal to the pump wave, without polarization diversity. (c) The probe wave is orthogonal to the original pump wave, with polarization diversity. (d) The probe wave is aligned at  $\theta$  to the original pump wave, with polarization diversity.

## 6.2 Polarization Diversity Scheme in Distributed Sensing System

rately. Fig.6.3(c) and (d) show the concept of proposed polarization diversity when the polarization state of probe wave is orthogonal to one sub-pulse of the pump, and aligned at  $\theta$  to one sub-pulse of the pump, respectively. It is shown that the probe is amplified by the same value regardless of the relative polarization state between the pump and the probe waves. The Brillouin gain in the proposed scheme is 3dB smaller than that shown in Fig.6.3(a) as the intensity of the sub-pulses of pump is half of the original pump.

Assume the Jones vectors of the two orthogonal polarized sub-pulses are  $\vec{P}_1 = \begin{pmatrix} E_1 \cos \alpha \\ E_1 \sin \alpha \end{pmatrix}$  and  $\vec{P}_2 = \begin{pmatrix} -E_1 \sin \alpha \\ E_1 \cos \alpha \end{pmatrix}$ , and the Jones vector of the probe wave is  $\vec{P}_b = \begin{pmatrix} E_2 \cos \beta \\ E_2 \sin \beta \end{pmatrix}$ , where  $E_1$  and  $E_2$  are constant,  $\alpha$  and  $\beta$  are random phase. After go through a piece of fiber with linear birefringence, the two orthogonal polarized sub-pulses are  $\vec{P}'_1 = \begin{pmatrix} E_1 \cos \alpha \\ E_1 \sin \alpha \exp(-j\phi) \end{pmatrix}$ , and  $\vec{P}'_2 = \begin{pmatrix} -E_1 \sin \alpha \\ E_1 \cos \alpha \exp(-j\phi) \end{pmatrix}$ . As the transmission direction of the probe is different from that of pump, the Jones vector of the probe is  $\vec{P}'_b = \begin{pmatrix} E_2 \cos \beta \\ E_2 \sin \beta \exp(j\theta) \end{pmatrix}$ . At the beginning of the fiber, the mixing efficiency between the pump and probe waves is,

$$\begin{aligned} \eta &= \sqrt{(P_1 \cdot P_b)^2 + (P_2 \cdot P_b)^2} \\ &= \sqrt{(E_1 E_2 \cos \alpha \cos \beta)^2 + (E_1 E_2 \sin \alpha \sin \beta)^2 + (-E_1 E_2 \sin \alpha \cos \beta)^2 + (E_1 E_2 \cos \alpha \sin \beta)^2} \\ &= E_1 E_2 \end{aligned} \quad (6.1)$$

After go through a piece of linear birefringence fiber, the mixing efficiency between the pump and probe waves is,

$$\begin{aligned} \eta' &= \sqrt{|P'_1 \cdot P'_b|^2 + |P'_2 \cdot P'_b|^2} \\ &= E_1 E_2 \sqrt{|\cos \alpha \cos \beta + \sin \alpha \sin \beta \exp(j\theta - j\phi)|^2 + |-\sin \alpha \cos \beta + \cos \alpha \sin \beta \exp(j\theta - j\phi)|^2} \end{aligned}$$

### 6.3 Experimental Setup

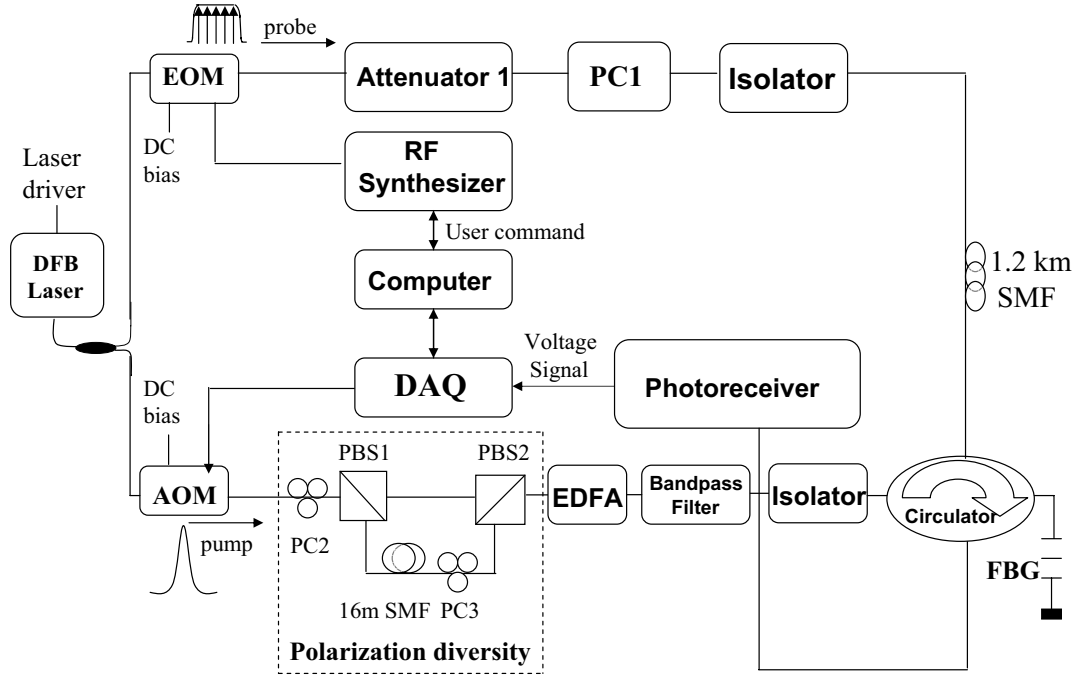


Figure 6.4: Experimental set-up of BOCDA fiber optic distributed sensing system with a polarization diversity scheme on the pulsed pump wave.

$$\begin{aligned}
 &= E_1 E_2 \sqrt{(\cos \alpha \cos \beta + \sin \alpha \sin \beta)^2 + (-\sin \alpha \cos \beta + \cos \alpha \sin \beta)^2} \\
 &= E_1 E_2
 \end{aligned} \tag{6.2}$$

From the equation above, it can be deduced that the mixing efficiency  $\eta$  between the pump and probe waves is depend only on the intensities of the pump and probe waves ( $E_1$  and  $E_2$ ). Thus, the SBS gain remains a constant regardless of the relative polarization state between pump and probe waves.

## 6.3 Experimental Setup

Fig.6.4 shows the experimental setup of the BOTDA sensing system with a polarization diversity applied on pump wave. The output of the distributed feedback (DFB) laser is split into two channels by a polarization maintaining coupler (30:70). One of the output ports of the coupler is modulated by an electro-optic modulator (EOM) and serves as a probe wave. The EOM is biased at transmission null point and generates two sidebands. One of the two sidebands is in the BGS and the other one is filter out by a FBG filter. The modulation frequency of the EOM can be tuned by the computer through the RF synthesizer so as to get the BGS. The other output of the coupler is modulated by an acousto-optic modulator (AOM) and serves as a pulsed pump wave. The pulse width and the interval time of the pump beams are controlled by the computer via data acquisition (DAQ).

The AOM is followed by a polarization diversity scheme which is efficient on suppressing the fluctuation induced by polarization mismatch. The pulsed pump wave is split into two beams with orthogonal polarization states by PBS1. One of the two states is delayed by  $80ns$  (the pulse width of the pump wave) using a  $16m$  SMF and then combined with the other state by PBS2. If the shorter pulse is used as pump wave, the length of SMF decreases proportionally. In our system, the further reduction of the pump pulse width is limited by the rising time of the AOM. PC3 aligns the polarization states of the pulse wave at the end of SMF to the principle states of polarization (PSPs) of PBS2. PC2 is used to align the pump wave at 45 degree respect to the PSPs of the fiber. (Note that the PCs can be eliminated by using PM fiber and 45 degree splicing PM PBSs.) Since the pump pulse contains two orthogonal polarization states, the Brillouin gain will be remain constant regardless of the polarization state of the probe wave and the Brillouin frequency shift  $\Omega_B$  will not change when the relative

## 6.4 Experimental Results

---

polarization state between pump and probe waves changes.

The polarization diversity scheme is followed by an erbium doped fiber amplifier (EDFA) and bandpass filter which are used to amplify the pump pulse to reach the Brillouin threshold. The CW probe and pulsed pump counter-propagate in the 1.2 km SMF, and the amplified probe is detected by a photoreceiver via a four ports circulator. An athermal fiber Bragg grating (FBG) module is used as a notch filter to filter out the unwanted sideband of the probe wave outside BGS.

The modulation frequency of EOM, pulse width of the pump wave and the interval time of two pulsed pumps are controlled by a computer through a RF synthesizer. Besides, the range of frequency sweep of EOM and the step of the sweep are also controlled by the computer. Thus, it is easy to change these parameters to achieve a stable measurement.

## 6.4 Experimental Results

The Brillouin gain spectrum (BGS) is obtained by sweeping the modulation frequency of EOM around the Brillouin shift of the FUT ( $\sim 10.84$  GHz). The step of the frequency sweeping is 10 MHz. The Brillouin frequency shift  $\Omega_B$  at every position along the FUT can be obtained after the sweeping and is set as a frequency reference. Then, the modulation frequency is scanned continuously to get the instantaneous Brillouin frequency shift. For every position along the FUT, if  $\Omega_B$  has no change compare with the frequency reference, the temperature at the location is the same as room temperature (or the strain at the location is the same as normal strain); otherwise, the temperature is different from the room temperature (or the strain is different from normal strain) and can be calculated through the change of Brillouin frequency shift.

In the experiment, the polarization state of the probe can be tuned by PC1 which



## 6.4 Experimental Results

---

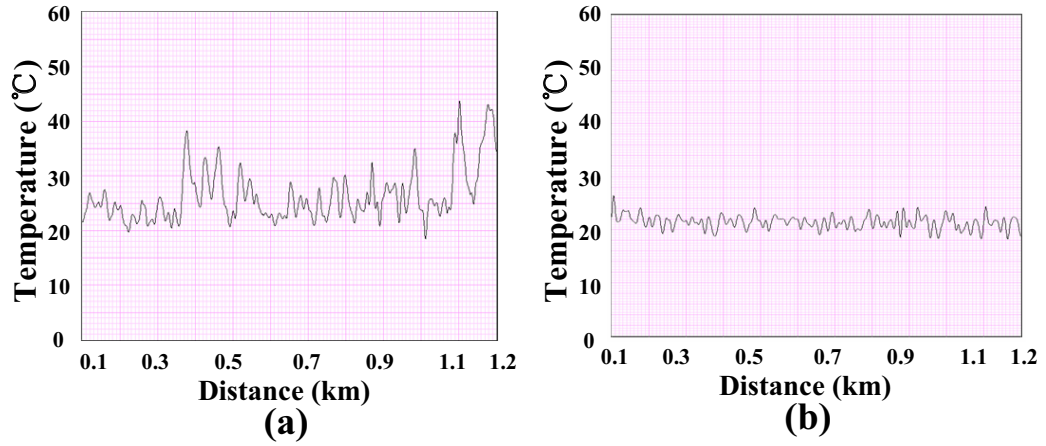


Figure 6.5: Measured temperature distribution along 1.2 km SMF in the environment of room temperature (a) without polarization diversity and (b) with polarization diversity by the proposed scheme.

adjusts the polarization state automatically and supplies all possible states of polarization. The distributed temperature and strain measurements along a 1.2 km SMF are shown in this section. The results demonstrate that the proposed polarization diversity scheme suppresses the polarization induced signal fluctuation effectively. And the measurement time is only 3s, which is the same as that without polarization diversity scheme.

### 6.4.1 Distributed Temperature Measurement

For the temperature measurement, the 1.2 km SMF is under normal strain. When the fiber under test is under room temperature, the measured distributed temperature has a large fluctuation (more than 20°C) when the polarization state of the probe wave changes at the absent of polarization diversity scheme, shown in Fig. 6.5(a). On the

## 6.4 Experimental Results

---

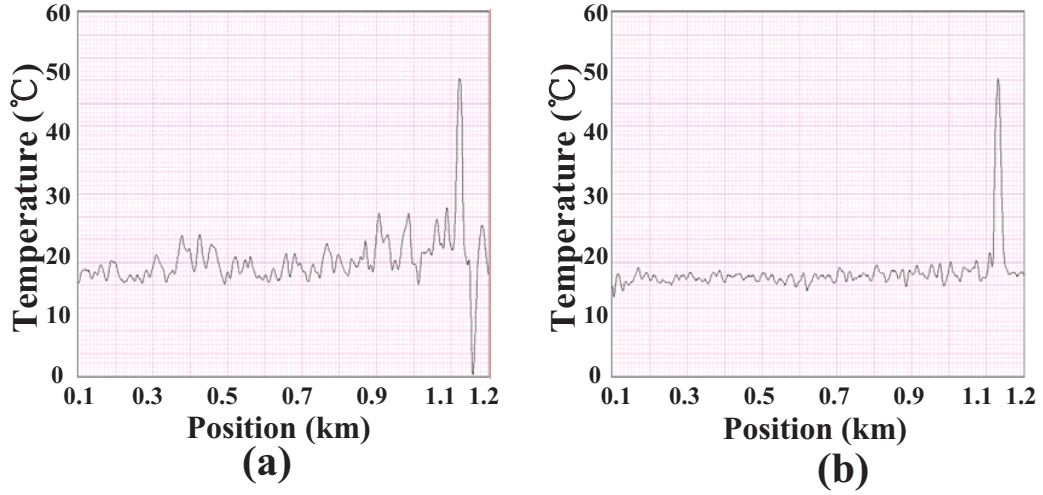


Figure 6.6: Measured temperature distribution along 1.2 km SMF when putting a section of fiber at the location of 1.1 km into hot water (a) without polarization diversity and (b) with polarization diversity by the proposed scheme.

other hand, the DOP of the pump pulse decreases to only 5% after the proposed polarization diversity scheme and the temperature fluctuation under room temperature is only  $\pm 3^\circ\text{C}$  when the SOP of the probe wave changes, shown in Fig. 6.5(b). Although there are small fluctuations, the average temperature ( $22^\circ\text{C}$ ) shown in Fig. 6.5(b) meet the room temperature very well. As the proposed polarization scheme needs no control system or active components, the measurement time is only 3s.

Fig.6.6 shows the distributed temperature measurement result along 1.2 km SMF. A piece of fiber, located at 1.1 km, is put into hot water. The location of temperature change shown in Fig.6.6 is 1.13 km and the small difference is caused by pigtails of the components in the set up. Fig.6.6(a) shows that in the system without proposed scheme, the fluctuation is large especially near the location of temperature change and it is difficult to find the change position. In the system with polarization diver-

## 6.4 Experimental Results

---

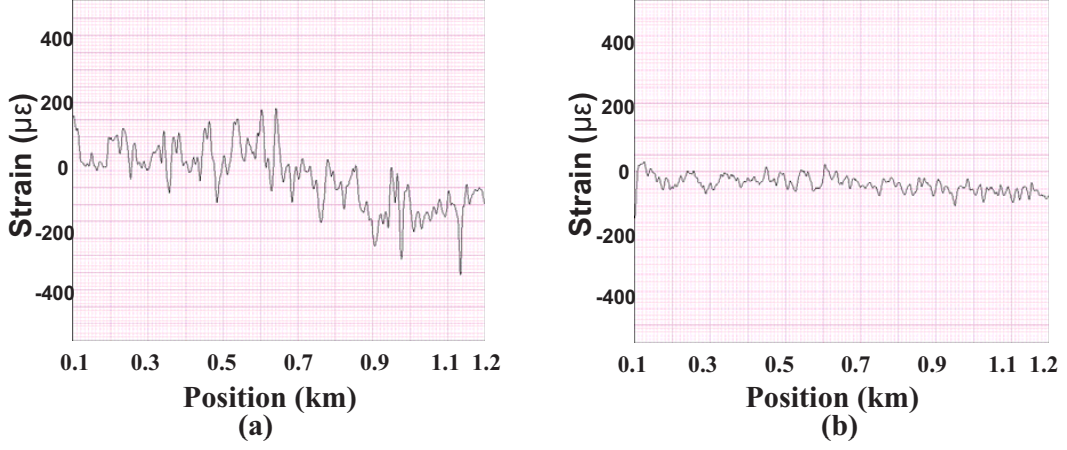


Figure 6.7: Measured distributed strain along 1.2 km SMF under normal (a) without polarization diversity and (b) with polarization diversity by the proposed scheme.

sity scheme, the fluctuation is much smaller and the signal is stable near the position of temperature change although the relative polarization state between the pump and probe wave has been changed, depicted in Fig.6.6(b). It is experimentally shown that the proposed system is capable of measuring precise temperature and accurate location in the distributed sensing system. And the polarization induced signal fluctuation has been suppressed successfully.

### 6.4.2 Distributed Strain Measurement

The Brillouin frequency shift  $\Omega_B$  changes with temperature as well as strain. In our system, only one of them can be measured in one time. For the strain measurement, the SMF is under room temperature (21.8 °C). The polarization state of the probe wave can be tuned by PC1, which adjusts the polarization state automatically and supplies all possible states of polarization. When the FUT is under normal strain, as the change of polarization state of the probe beam, the measured distributed strain has a large

## 6.4 Experimental Results

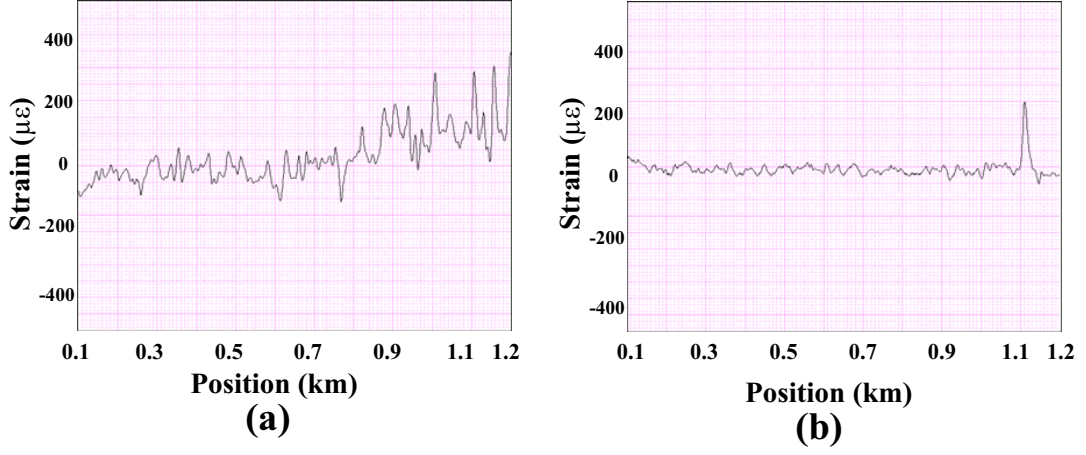


Figure 6.8: Measured distributed strain along 1.2 km SMF with a strain-applied section at the location of 1.1 km (a) without polarization diversity and (b) with polarization diversity by the proposed scheme.

fluctuation (more than  $\pm 300 \mu\epsilon$ ) in the system with absent of polarization diversity scheme, shown in Fig. 6.7(a). On the other hand, in the system with polarization diversity scheme, the DOP of the pump pulse decreases from 95% to only 5% and the strain fluctuation in the system is about  $\pm 50 \mu\epsilon$ , shown in Fig. 6.7(b). Although the measured strain has small fluctuation, the system is more stable when the polarization state of the probe wave changes.

In the experiment, a section of the FUT, located at about 1.1 km, was super glued on two cylinders with 2.5 rounds. The distance between the cylinders was 213 cm which can be tuned with a resolution of  $5 \mu m$ . Thus the length of the strain applied fiber is about 10.5m. The reference strain was obtained when the fiber stretching unit under normal strain. By increasing the distance between the two cylinders, strain is applied on the fiber. Fig. 6.8 (a) shows that in the system without polarization diversity

## 6.5 Conclusions

---

scheme, the strain fluctuation induced by polarization mismatch is large (about  $\pm 300 \mu\epsilon$ ) especially near the location of strain-applied fiber and it is failed to detect the location of strain change. In the system with proposed scheme, the fluctuation induced by polarization mismatch is much smaller (about  $\pm 50 \mu\epsilon$ ) and the signal is stable near the position of strain change, depicted in Fig. 6.8 (b). The location of strain-applied fiber shown in Fig. 6.8 (b) is 1.13 km and the small difference is caused by pigtails of the components in the set up.

It is experimentally shown that the proposed distributed sensing system is capable of measuring precise strain and accurate location along the 1.2-km SMF. The polarization sensitivity in the optical sensing system has been suppressed efficiently by the proposed scheme. Besides, the measurement time is relative short, only 3 seconds, which is the same as the system without the proposed polarization diversity scheme. In the proposed scheme, normal PBSs are used, and it needs two PCs to align the SOP of the pump wave to 45 degree to the PBSs. If the polarization maintaining PBSs and PM fiber are used, the PCs can be eliminated and the scheme is easier to achieve in real systems.

## 6.5 Conclusions

The proposed polarization diversity scheme in the BOTDA distributed sensing system has successfully reduced the DOP of the pump pulse from 93.5% to 5% and achieves a stable distributed temperature and strain measurement. The polarization induced temperature fluctuation is suppressed to only  $\pm 3^\circ\text{C}$  from  $\pm 20^\circ\text{C}$ , and the strain fluctuation is reduce to  $\pm 50 \mu\epsilon$  from  $\pm 300 \mu\epsilon$ . Beside the stable temperature and strain measurements, accurate location information can also be obtained by the time-of-flight in the system. The proposed scheme does not need any feedback control system and

## 6.5 Conclusions

---

the measurement time is only 3s. It is also cost effective as only two PBSs and a piece of fiber is used. Both theoretical analysis and experiment results show that the proposed scheme is efficient on eliminating polarization induced fluctuation in BOTDA fiber optic distributed sensing system.

# **Chapter 7**

## **Conclusions and Future Work**

The physical effects are intrinsic properties of optical fibers, which always affect the performance of optical systems. The study and management of fiber physical effects make it possible to achieve higher performance in various optical systems. In this thesis, several fiber physical effects (chromatic dispersion, polarization mode dispersion, parametric process and stimulated Brillouin scattering) have been studied in optical communication and sensor systems. This chapter will conclude the main contribution of this thesis and point out several topics in the future works.

### **7.1 Conclusions**

In this thesis several works on management of fiber physical effects have been done. Firstly, high-speed multi-channel optical pulse train generation based on parametric process has been demonstrated experimentally. The generated 80 GHz pulses with high ER can be used as optical sources in the WDM transmission systems. The characteristic of the parametric amplifier using HNLF has been studied. The wavelength of pump pulse is optimized to obtain large gain and wide gain bandwidth. The qualities of

## 7.1 Conclusions

---

the generated pulse trains are analyzed numerically using VPItransmissionMaker 7.0. The power penalties of the generated pulse trains are less than 0.5 dB in back-to-back case.

In the second part, a broadband multi-wavelength source using a single phase modulator is generated in an amplified loop. The loop length, gain and polarization state were tuned to obtain broad optical spectrum and more light source channels. Generation of 125-channel light source with more than 30 dB optical signal-to-noise ratio is demonstrated experimentally. Neither high optical power nor large drive voltage is employed in this method.

In the third part, chromatic dispersion and polarization mode dispersion monitoring methods based on RF power measurement and optical filtering are proposed. Both simulation and experimental results show the efficiency of the methods. By using a narrow band FBG filter in one of sidebands, the chromatic dispersion effects on RF power can be eliminated and CD insensitive PMD monitoring can be achieved. Besides, by monitoring the low frequency RF power, the photodetector with low bandwidth is used in the monitoring branch. Therefore, the monitoring range is increased and the cost of the system is decreased. On the other hand, PMD insensitive CD monitoring utilizing RF power ratio has been demonstrated. As the RF power decreases with PMD in both filtered and non-filtered signals, the PMD effects on RF power can be eliminated by using the RF power ratio of the two signals.

Lastly, a polarization diversity scheme is proposed to suppress the polarization induced signal fluctuation in BOTDA distributed sensing system. The polarization diversity scheme is applied on the pump pulse, whose degree of polarization is decreased from 93.5% to 5% by the proposed scheme. The polarization induced temperature fluctuation is suppressed to only  $\pm 3$  °C from  $\pm 20$  °C, and the strain fluctuation is reduced to  $\pm 50$   $\mu\epsilon$  from  $\pm 300$   $\mu\epsilon$ . Beside the stable temperature and strain measurements,



## 7.2 Future Work

---

accurate location information can also be obtained by the time-of-flight in the system. The proposed scheme does not need any feedback control system and the measurement time is only 3s.

## 7.2 Future Work

The application and management of physical effects of optical fiber are studied in this thesis. However, there are still many challenges to be overcome. Based on the works have been done, following topics are valuable for further studies.

1. Chromatic dispersion and polarization mode dispersion measurement method based on RF power were demonstrated in this thesis. The measurement result is affected by the center wavelength of FBG filter. However, the reflection wavelength of a FBG depends on the environment parameters, such as temperature and strain. Therefore, the fixing of FBG center wavelength is a key issue in monitoring system. Besides, the application of proposed method in WDM system is also a promising topic. Narrow band notch filters with equal spacing, which is not affected by environment parameters, are good candidates for such applications.

2. Chromatic dispersion monitoring utilizing amplitude ratio in delay-tap sampling plot was proposed. However, the eye-diagram and delay-tap sampling plot are affected by other degrading effects, such as polarization mode dispersion, and optical signal-to-noise ratio [137]. Therefore, distinguishing various degrading effects based on the amplitude ratio of delay-tap sampling plot is a big challenge.

# Bibliography

- [1] Govind P. Agrawal, *Nonlinear fiber optics*, third edition, Academic press, New York, 2001.
- [2] R. Jopson, L. Nelson, G. J. Pendock, and A. H. Gnauck, "Polarization-mode dispersion impairment in return-to-zero and nonreturn-to-zero systems," *Conference on Optical Fiber Communication (OFC)*'99, Paper WE3, San Diego, CA, Mar 1999.
- [3] H. Sunnerud, M. Karlsson, and P. A. Andrekson, "A comparison between NRZ and RZ data formats with respect to PMD-induced system degradation," *Conference on Optical Fiber Communication (OFC)*'01, Paper WT3, Anaheim, CA, Mar 2001.
- [4] F. Shimizu, "Frequency Broadening in Liquids by a Short Light Pulse," *Physical Review Letters*, vol. 19, pp. 1097-1100, 1967.
- [5] R. H. Stolen and C. Lin, "Self-phase modulation in silica optical fibers," *Physical Review A*, vol. 17, pp. 1448-1453, 1978.
- [6] R. A. Fisher and W. K. Bischel, "Numerical studies of the interplay between self-phase modulation and dispersion for intense plane-wave laser pulses," *Journal of Applied Physics*, vol. 46, pp. 4921-4934, 1975.

## BIBLIOGRAPHY

---

- [7] J. I. Gersten, R. R. Alfano, and M. Belic, "Combined stimulated Raman scattering and continuum self-phase modulations," *Physical Review A*, vol. 21, pp. 1222-1224, 1980.
- [8] E. J. Woodbury and W. K. Ng, "Ruby laser operation in the near IR," *Proc. IRE* 50, pp. 2347, 1962.
- [9] M. Ikeda, "Stimulated Raman amplification characteristics in long span single-mode silica fibers," *Optics Communications*, vol. 39, pp. 148-152, 1981.
- [10] E. Desurvire, M. Papuchon, J. P. Pocholle, J. Raffy, and D. B. Ostrowsky, "High-gain optical amplification of laser diode signal by Raman scattering in single-mode fibres," *Electronics Letters*, vol. 19, pp. 751-753, 1983.
- [11] M. J. O'Mahony, "Semiconductor laser optical amplifiers for use in future fiber systems," *Journal of Lightwave Technology*, vol. 6, pp. 531-544, 1988.
- [12] R. H. Stolen, E. P. Ippen, and A. R. Tynes, "Raman oscillation in glass optical waveguide," *Applied Physics Letters*, vol. 20, pp. 62-64, 1972.
- [13] K. O. Hill, B. S. Kawasaki, and D. C. Johnson, "Low-threshold CW Raman laser," *Applied Physics Letters*, vol. 28, pp. 181-183, 1976.
- [14] C. Lin and W. G. French, "A near-infrared fiber raman oscillator tunable from 1.07 to 1.32  $\mu\text{m}$ ," *Applied Physics Letters*, vol. 34, pp. 666-668, 1979.
- [15] I. K. Ilev, H. Kumagai, and H. Toyoda, "Ultraviolet and blue discretely tunable double-pass fiber Raman laser," *Applied Physics Letters*, vol. 70, pp. 3200-3202, 1997.

## BIBLIOGRAPHY

---

- [16] R. Y. Chiao, C. H. Townes, and B. P. Stoicheff, "Stimulated Brillouin scattering and coherent generation of intense hypersonic waves," *Physical Review Letters*, vol. 12, pp. 592-595, 1964.
- [17] E. Garmire and C. H. Townes, "Stimulated Brillouin scattering in liquids," *Applied Physics Letters*, vol. 5, pp. 84-86, 1964.
- [18] N. A. Olsson and J. P. van der Ziel, "Characteristics of a semiconductor laser pumped Brillouin amplifier with electronically controlled bandwidth," *Journal of Lightwave Technology*, vol. LT-5, pp. 147-153, 1987.
- [19] R. G. Waarts, A. A. Friesem, and Y. Hefetz, "Frequency-modulated to amplitude-modulated signal conversion by a Brillouin-induced phase change in single-mode fibers," *Optics Letters*, vol. 13, pp. 152-154, 1988.
- [20] K. O. Hill, B. S. Kawasaki, and D. C. Johnson, "CW Brillouin laser," *Applied Physics Letters*, vol. 28, pp. 608-609, 1976.
- [21] S. P. Smith, F. Zarinetchi, and S. Ezekiel, "Narrow-linewidth stimulated Brillouin fiber laser and applications," *Optics Letters*, vol. 16, pp. 393-395, 1991.
- [22] S. Huang, L. Thevenaz, K. Toyama, B. Y. Kim, and H. J. Shaw, "Optical Kerr-effect in fiber-optic Brillouin ring laser gyroscopes," *IEEE Photonics Technology Letters*, vol. 5, pp. 365-369, 1993.
- [23] J. Botineau, E. Picholle, and D. Bahloul, "Effective stimulated Brillouin gain in single mode optical fibres," *Electronics Letters*, vol. 31, pp. 2032-2034, 1995.
- [24] K. Shiraki, M. Ohashi, and M. Tateda, "SBS threshold of a fiber with a Brillouin frequency shift distribution," *Journal of Lightwave Technology*, vol. 14, pp. 50-57, 1996.

## BIBLIOGRAPHY

---

- [25] J. A. Armstrong, N. Bloembergen, J. Ducuing, and P. S. Pershan, "Interaction between light waves in a nonlinear dielectric," *Physical Review*, vol. 127, pp. 1918-1939, 1962.
- [26] Y. R. Shen, *The Principles of Nonlinear Optics*, Wiley, New York, 1984.
- [27] Govind P. Agrawal, *Fiber-Optic Communication Systems*, third edition, Wiley, 2002.
- [28] K. Morito, R. Sahara, K. Sato, and Y. Kotaki, "Penalty-free 10 Gb/s NRZ transmission over 100 km of standard fiber at 1.55  $\mu\text{m}$  with a blue-chirp modulator integrated DFB laser," *IEEE Photonics Technology Letters*, vol. 8, pp. 431-433, 1996.
- [29] R. M. Jopson, "Dispersion control in long high-dispersion fibre links," *European Conference on Optical Communications(ECOC)*, Oslo, Norway, vol. 2, pp. 675-680, 1994.
- [30] K. Yonenaga and N. Takachio, "Fiber chromatic dispersion compensation technique with an optical SSB transmission in optical homodyne detection systems," *IEEE Photonics Technology Letters*, vol. 5, pp. 949-951, 1993.
- [31] E. Ip and J. M. Kahn, "Digital equalization of chromatic dispersion and polarization mode dispersion," *Journal of Lightwave Technology*, vol. 25, pp. 2033-2043, 2007.
- [32] C. Lin, H. Kogelnik, and L. G. Cohen, "Optical-pulse equalization of low-dispersion transmission in single-mode fibers in the 1.3-1.7- $\mu\text{m}$  spectral region," *Optics Letters*, vol. 5, pp. 476-478, 1980.

## BIBLIOGRAPHY

---

- [33] C. Weinstein, "Fiber design improves long-haul performance ," *Laser Focus World*, vol. 33, pp. 215-216, 1997.
- [34] M. E. Marhic, F. S. Yang, and L. G. Kazovsky, "Cancellation of stimulated-Raman-scattering cross talk in wavelength-division-multiplexed optical communication systems by series or parallel techniques ," *Journal of the Optical Society of America B*, vol. 15, pp. 957-963, 1998.
- [35] C. M. McIntosh, A. G. Grandpierre, D. N. Christodoulides, J. Toulouse, and J. M. P. Delvaux, "Eliminating SRS channel depletion in massive WDM systems via optical filtering techniques," *IEEE Photonics Technology Letters*, vol. 13, pp. 302-304, 2001.
- [36] D. A. Fishman and J. A. Nagel, "Degradations due to stimulated Brillouin scattering in multigigabit intensity-modulated fiber-optic systems," *Journal of Lightwave Technology*, vol. 11, pp. 1721-1728, 1993.
- [37] M. O. van Deventer and A. J. Boot, "Polarization properties of stimulated Brillouin scattering in single-mode fibers," *Journal of Lightwave Technology*, vol. 12, pp. 585-590, 1994.
- [38] N. Yoshizawa and T. Imai, "Stimulated Brillouin scattering suppression by means of applying strain distribution to fiber with cabling," *Journal of Lightwave Technology*, vol. 11, pp. 1518-1522, 1993.
- [39] Y. Horiuchi, S. Yamamoto, and s. Akiba, "Stimulated Brillouin scattering suppression effects induced by cross-phase modulation in high power WDM repeaterless transmission," *Electronics Letters*, vol. 34, pp. 390-391, 1998.

## BIBLIOGRAPHY

---

- [40] S. S. Lee, H. J. Lee, W. Seo, and S. G. Lee, "Stimulated brillouin scattering suppression using cross-phase modulation induced by an optical supervisory channel in WDM links," *IEEE Photonics Technology Letters*, vol. 13, pp. 741-743, 2001.
- [41] F. Forghieri, R. W. Tkach, and A. R. Chraplyvy, *Optical Fiber Telecommunications III*, Academic Press, San Diego, CA, 1997.
- [42] I. Neokosmidis, T. Kamalakis, A. Chipouras,; T. Sphicopoulos, "New techniques for the suppression of the four-wave mixing-induced distortion in nonzero dispersion fiber WDM systems ," *Journal of Lightwave Technology*, vol. 23, pp. 1137-1144, 2005.
- [43] H. Suzuki, S. Ohteru, and N. Takachio, "22×10 Gb/s WDM transmission based on extended method of unequally spaced channel allocation around the zero-dispersion wavelength region," *IEEE Photonics Technology Letters*, vol. 11, pp. 1677-1679, 1999.
- [44] K. Nakajima, M. Ohashi, and Y. Miyajima, "Four-wave-mixing suppression effect of dispersion varying fiber," *IEEE Photonics Technology Letters*, vol. 10, pp. 537-539, 1998.
- [45] M. Nakazawa, H. Kubota, K. Suzuki, E. Yamada, and A. Sahara, "Ultrahigh-speed long-distance TDM and WDM soliton transmission technologies," *IEEE Journal on Selected Topics in Quantum Electronics*, vol. 6, pp. 363-396, 2000.
- [46] A. Hasegawa and F. Tappert, "Transmission of stationary nonlinear optical pulses in dispersive dielectric fibers. I. Anomalous dispersion," *Applied Physics Letters*, vol. 23, pp. 142-144, 1973.
- [47] A Hasegawa and Y. Kodama, "Amplification and reshaping of optical solitons in a glass fiber. I," *Optics Letters*, vol. 7, pp. 285-287, 1982.

## BIBLIOGRAPHY

---

- [48] L. F. Mollenauer and K. Smith, "Demonstration of soliton transmission over >1000 km in fiber with loss compensated by Raman gain," *Optics Letters*, vol. 13, pp. 675, 1988.
- [49] P. Andrekson, "Soliton tests show promise for dense WDM systems," *Laser Focus World*, vol. 35, pp. 137, 1999.
- [50] N. Edagawa, K. Mochizuki, and Y. Iwamoto, "Simultaneous amplification of wavelength-division-multiplexed signals by a highly efficient fibre Raman amplifier pumped by high-power semiconductor lasers," *Electronics Letters*, vol. 23, pp. 196-197, 1987.
- [51] H. Masuda and S. Kawai, "Wide-band and gain-flattened hybrid fiber amplifier consisting of an EDFA and a multiwavelength pumped Raman amplifier," *IEEE Photonics Technology Letters*, vol. 11, pp. 647-649, 1999.
- [52] K. Thyagarajan and C. Kakkar, "Fiber design for broad-band gain-flattened Raman fiber amplifier," *IEEE Photonics Technology Letters*, vol. 15, pp. 1701-1703, 2003.
- [53] A. Mori, H. Masuda, K. Shikano, and M. Shimizu, "Ultra-wide-band tellurite-based fiber Raman amplifier," *Journal of Lightwave Technology*, vol. 21, pp. 1300-1306, 2003.
- [54] T. Torounidis, P. A. Andrekson, B.-E. Olsson, "Fiber-optical parametric amplifier with 70-dB gain," *IEEE Photonics Technology Letters*, vol. 18, pp. 1194-1196, 2006.
- [55] M.-C. Ho, K. Uesaka, M. Marhic, Y. Akasaka, and L.G. Kazovsky, "200-nm-bandwidth fiber optical amplifier combining parametric and Raman gain," *Journal of Lightwave Technology*, vol. 19, pp. 977-981, 2001.



## BIBLIOGRAPHY

---

- [56] M. E. Marhic, N. Kagi, T. K. Chiang, and L. G. Kazovsky, "Broadband fiber optical parametric amplifiers," *Optics Letters*, vol. 21, pp. 573, 1996.
- [57] J.M.C. Boggio, J.D. Marconi, and H.L. Fragnito, "Double-pumped fiber optical parametric amplifier with flat gain over 47-nm bandwidth using a conventional dispersion-shifted fiber," *IEEE Photonics Technology Letters*, vol. 17, pp. 1842-1844, 2005.
- [58] S. Wabnitz, "Broadband parametric amplification in photonic crystal fibers with two zero-dispersion wavelengths," *Journal of Lightwave Technology*, vol. 24, pp. 1732-1736, 2006.
- [59] S. Watanabe and T. Chikama, "Highly efficient conversion and parametric gain of nondegenerate forward four-wave mixing in a singlemode fibre," *Electronics Letters*, vol. 30, pp. 163-164, 1994.
- [60] K. Inoue, "Arrangement of fiber pieces for a wide wavelength conversion range by fiber four-wave mixing," *Optics Letters*, vol. 19, pp. 1189-1191, 1994.
- [61] E. Ciaramella and S. Trillo, "All-optical signal reshaping via four-wave mixing in optical fibers," *IEEE Photonics Technology Letters*, vol. 12, pp. 849-851, 2000.
- [62] M. Hirano, T. Nakanishi, and T. Sasaki, "Highly nonlinear fiber with reduced dispersion slope and efficient wavelength conversion with sub-ps walk-off," *Conference on Optical Fiber Communication (OFC)'08*, paper OMP5, Anaheim, CA, Mar 2008.
- [63] G. Lu, K. S. Abedin, and T. Miyazaki, "DPSK multicast using multiple-pump FWM in Bismuths highly nonlinear fiber with high multicast efficiency," *Optics Express*, vol. 12, pp. 21964-21970, 2008.

## BIBLIOGRAPHY

---

- [64] Y. Dong, Z. Li, C. Yu, Y.J. Wen, Y. Wang, C. Lu, W. Hu, and T.H. Cheng, "Generation of multi-channel short-pulse sources using nonlinear optical loop mirror based on photonic crystal fiber," *Conference on Optical Fiber Communication (OFC)'07*, paper JWA9, Anaheim, CA, Mar 2007.
- [65] K. K. Chow, C. Shu, C. Lin, and A. Bjarklev, "Polarization-insensitive widely tunable wavelength converter based on four-wave mixing in a dispersion-flattened nonlinear photonic Crystal fiber," *IEEE Photonics Technology Letters*, vol. 17, pp. 624-626, 2005.
- [66] Y. Wang, C. Yu, T. Luo, L. Yan, Z. Pan and A. E. Willner, "Tunable all-optical wavelength conversion and wavelength multicasting using orthogonally polarized fiber FWM," *Journal of Lightwave Technology*, vol. 23, pp. 3331-3338, 2005.
- [67] C.-S. Bres, N. Alic, E. Myslivets and S. Radic, "1-to-40 multicasting and amplification of 40Gbps channels in wideband parametric amplifier," *Conference on Optical Fiber Communication (OFC)'08*, paper PDP16, Anaheim, CA, Mar 2008.
- [68] P. O. Hedekvist, M. Karlsson, and P. A. Andrekson, "Fiber four-wave mixing demultiplexing with inherent parametric amplification," *Journal of Lightwave Technology*, vol. 15, pp. 2051-2058, 1997.
- [69] M. P. Fok and C. Shu, "Tunable optical delay using four-wave mixing in a 35-cm highly nonlinear Bismuth-Oxide fiber and group velocity dispersion," *Journal of Lightwave Technology*, vol. 26, pp. 499-504, 2008.
- [70] A. D. Kersey, M. A. Davis, H. J. Patrick, M. LeBlanc, K. P. Koo, C. G. Askins, M. A. Putnam, and E. J. Friebele, "Fiber grating sensors," *IEEE Photonics Technology Letters*, vol. 15, pp. 1442-1463, 1997.

## BIBLIOGRAPHY

---

- [71] Y. Yu, H. Tam, W. Chung, and M. S. Demokan, "Fiber Bragg grating sensor for simultaneous measurement of displacement and temperature," *Optics Letters*, vol. 25, pp. 1141-1143, 2000.
- [72] W. Zhang, G. Kai, X. Dong, S. Yuan, and Q. Zhao, "Temperature-independent FBG-type torsion sensor based on combinatorial torsion beam," *IEEE Photonics Technology Letters*, vol. 14, pp. 1154-1156, 2002.
- [73] J. H. Ng, X. Zhou, X. Yang, and J. Hao, "A simple temperature-insensitive fiber Bragg grating displacement sensor," *Optics Communications*, vol. 273, pp. 398-401, 2007.
- [74] T. F. Capell, J. Palaniappan, S. L. Ogin, A. D. Crocombe, G. T. Reed, A. M. Thorne, L. Mohanty, and S. C. Tjin, "The use of an embedded chirped fibre Bragg grating sensor to monitor disbond initiation and growth in adhesively bonded composite/metal single lap joints," *Journal of Optics A: Pure and Applied Optics*, vol. 9, pp. S40-S44, 2007.
- [75] J. Palaniappan, H. Wang, S. L. Ogin, A. Thorne, G. T. Reed, S. C. Tjin, and L. N. McCartney, "Prediction of the reflected spectra from chirped fibre Bragg gratings embedded within cracked crossply laminates," *Measurement Science & Technology*, vol. 17, pp. 1609-1614, 2006.
- [76] S. Takeda, Y. Okabe, N. Takeda, "Application of chirped FBG sensors for detection of local delamination in composite laminates," *Proceedings of the SPIE - The International Society for Optical Engineering*, vol. 5050, pp. 171-178, 2003.
- [77] C. Chen and J. Albert, "Strain-optic coefficients of the individual cladding modes of a single mode fiber: theory and experiment," *Electronics Letters*, vol. 43, pp. 21-22, 2006.

## BIBLIOGRAPHY

---

- [78] C. Caucheteur, P. Mgret, and A. Cusano, "Tilted Bragg grating multipoint sensor based on wavelength-gated cladding-modes coupling," *Applied Optics*, vol. 48, pp. 3915-3920, 2009.
- [79] S. Baek, Y. Jeong, and B. Lee, "Characteristics of short-period fiber Bragg gratings for use as macro-bending sensors," *Applied Optics*, vol. 41, pp. 631-636, 2002.
- [80] A. M. Vengsarkar, P. J. Lemaire, J. B. Judkins, V. Bhatia, T. Erdogan, and J. E. Sipe, "Long-period fiber gratings as band-rejection filters," *Journal of Lightwave Technology*, vol. 14, pp. 58-65, 1996.
- [81] K. O. Hill and G. Meltz, "Fiber Bragg grating technology fundamentals and overview," *Journal of Lightwave Technology*, vol. 15, pp. 1163-1176, 1997.
- [82] V. Bhatia, "Applications of long-period gratings to single and multi-parameter sensing," *Optics Express*, vol. 4, pp. 457-466, 1999.
- [83] S. W. James and R. P. Tatam, "Optical fibre long-period grating sensors: Characteristics and application," *Measurement Science & Technology*, vol. 14, pp. R49-R61, 2003.
- [84] T. Kurashima, T. Horiguchi, and M. Tateda, "Distributed-temperature sensing using stimulated Brillouin scattering in optical silica fibers," *Optics Letters*, vol. 15, pp. 1038-1040, 1990.
- [85] X. Bao, D. J. Webb, and D. A. Jackson, "22-km distributed temperature sensor using Brillouin gain in an optical fiber," *Optics Letters*, vol. 18, pp. 552-554, 1994.

## BIBLIOGRAPHY

---

- [86] M. Nikles, L. Thevenaz, and P. A. Robert, "Simple distributed fiber sensor based on Brillouin gain spectrum analysis," *Optics Letters*, vol. 21, pp. 758-760, 1996.
- [87] X. Bao, D. J. Webb, and D. A. Jackson, "Combined distributed temperature and strain sensor based on Brillouin loss in an optical fiber," *Optics Letters*, vol. 19, pp. 141-143, 1994.
- [88] L. Thevenaz, M. Nikles, A. Fellay, N. Facchini, and P. Robert, "Applications of distributed Brillouin fibre sensing," *Proceedings of SPIE - The International Society for Optical Engineering*, vol. 3407, pp. 374-381, 1998.
- [89] Y. Dong, X. Bao, and W. Li, "Differential Brillouin gain for improving the temperature accuracy and spatial resolution in a long-distance distributed fiber sensor," *Applied Optics*, vol. 48, pp. 4297-4301, 2009.
- [90] H. Naruse and M. Tateda, "Trade-off between the spatial and the frequency resolutions in measuring the power spectrum of the Brillouin backscattered light in an optical fiber," *Applied Optics*, vol. 38, pp. 6516C6521, 1999.
- [91] X. Bao, J. Dhliwayo, N. heron, D. J. Webb and D. A. Jackson, "Experimental and theoretical studies on a distributed temperature sensor based on Brillouin scattering," *IEEE Journal of Lightwave Technology*, vol.13, pp. 1340-1348, 1995.
- [92] M. Nikles, L. Thevenaz and P. Robert, "Brillouin gain spectrum characterization in single-mode optical fibers," *IEEE Journal of Lightwave Technology*, vol.15, pp. 1842-1851, 1997.
- [93] X. Bao, M. DeMerchant, A. Brown, and T. Bremaner, "Tensile and compressive strain measurement in the lab and field with the distributed Brillouin scattering sensor," *IEEE Journal of Lightwave Technology*, vol.19, pp. 1698-1704, 2001.

## BIBLIOGRAPHY

---

- [94] D. Liu, M. Song, and X. Zhang, "Polarization insensitive coherent detection for Brillouin scattering spectrum in BOTDR," *Optical Communications*, 254, pp. 168-172, 2005
- [95] K. Hotate, K. Abe and K. Y. Song, "Suppression of signal fluctuation in Brillouin optical correlation domain analysis system using polarization diversity scheme," *IEEE Photonics Technology Letters*, vol. 18, pp. 2653-2655, 2006.
- [96] K. Hotate and T. Hasegawa, "Measurement of Brillouin gain spectrum distribution along an optical fiber using a correlation-based technique Proposal, experiment and simulation," *IEICE Transactions on Electronics*, vol. E83-C, pp. 405-412, 2000.
- [97] K. Hotate and M. Tanaka, "Distributed fiber Brillouin strain sensing with 1-cm spatial resolution by correlation-based continuous-wave technique," *IEEE Photonics Technology Letters*, vol. 14, pp. 179-181, 2002.
- [98] K. Y. Song, Z. He, and K. Hotate, "Distributed strain measurement with millimeter-order spatial resolution based on Brillouin optical correlation domain analysis," *Optics Letters*, vol. 31, pp. 2526-2528, 2006.
- [99] T. Yari, K. Nagai, M. Ishioka, K. Hotate, and Y. Koshioka, "Aircraft structural health monitoring using on-board BOCDA system," *Proceedings of SPIE - The International Society for Optical Engineering*, vol. 6933, 2008.
- [100] T. Torounidis, H. Sunnerud, P. O. Hedekvist, and P. A. Andrekson, "Amplification of WDM signals in fiber-based optical parametric amplifiers," *IEEE Photonics Technology Letters*, vol. 15, pp. 1061-1063, 2003.

## BIBLIOGRAPHY

---

- [101] T. Torounidis, P.A. Andrekson, and B.-E Olsson, "Gain and bandwidth characterization in fiber optical parametric amplifiers," *IEEE Photonics Technology Letters*, vol. 18, pp. 2578-2580, 2006.
- [102] Jianjun Yu, Xueyan Zheng, C. Peucheret, A. T. Clausen H. N. Poulsen and P. Jdppesen, "40-Gb/s all-optical wavelength conversion based on a nonlinear optical loop mirror," *Journal of Lightwave Technology*, vol. 18, pp. 1001-1007, 2000.
- [103] Jonas Hansryd and Peter A. Andrekson, "Broad-band continuous-wave-pumped fiber optical parametric amplifier with 49-dB gain and wavelength-conversion efficiency," *IEEE Photonics Technology Letters*, vol. 13, pp. 194-196, 2001.
- [104] D. Dahan, E. Shumakher, and G. Eisenstein, "A multiwavelength short pulse source based on saturated optical fiber parametric amplification," *IEEE Photonics Technology Letters*, vol. 18, pp. 592-594, 2006.
- [105] A. T. Clausen, L. Oxenlwe, C. Peucheret, H. N. Poulsen, P. Jeppesen, S. N. Knudsen, and L. Grner-Nielsen, "10-GHz return-to-zero pulse source tunable in wavelength with a single- or multiwavelength output based on four-wave mixing in a newly developed highly nonlinear fiber," *IEEE Photonics Technology Letters*, vol. 13, pp. 70-72, 2001.
- [106] T. Torounidis, M. Westlund, H. Sunnerud, B.-E Olsson, and P.A. Andrekson, "Fiber-optic parametric amplifier in a loop mirror configuration," *IEEE Photonics Technology Letters*, vol. 17, pp. 321-323, 2005.
- [107] D. B. Mortimore, "Fiber Loop Reflectors," *IEEE Journal of Lightwave Technology*, vol. 6, pp. 1217-1224, 1988.

## BIBLIOGRAPHY

---

- [108] W. Shieh, Q. Yang, Y. Ma, “107 Gb/s coherent optical OFDM transmission over 1000-km SSMF fiber using orthogonal band multiplexing,” *Optics Express*, vol. 16, pp. 6378-6386, 2008.
- [109] M. Fujiwara, J. Kani, H. Suzuki, K. Araya, and M. Teshima, “Flattened optical multicarrier generation of 12.5 GHz spaced 256 channels based on sinusoidal amplitude and phase hybrid modulation,” *Electronics Letters*, vol. 37, pp. 967-968, 2001.
- [110] F. C. G. Gunning and A. D. Ellis, “Generation of a widely spaced optical frequency comb using an amplitude modulator pair,” *The International Society for Optical Engineering*, vol. 5825, pp. 469-473, 2005.
- [111] T. Hoshi, T. Shioda, Y. Tanaka and T. Kurodawa, “10-Gbps DWDM transmission using multi-frequency light source with 50-GHz channel spacing,” *Conference on Optical Fiber Communication (OFC)’07*, paper, pp. 319-321, Anaheim, CA, Mar.2007.
- [112] M. Weiming, P. A. Andrekson, and J. Toulouse, “Investigation of a spectrally flat multi-wavelength DWDM source based on optical phase- and intensity-modulation,” *Conference on Optical Fiber Communication (OFC)’04*, pp. 235-237, New Orleans, LA, Mar. 2004.
- [113] T. Sakamoto, T. Kawanishi, and M. Izutsu, “Asymptotic formalism for ultra-flat optical frequency comb generation using a Mach-Zehnder modulator,” *Optics Letters*, vol. 32, pp. 1515-1517, 2007.
- [114] Y. Wang, Z. Pan, C. Yu, T. Luo, A. Sahin, and A. Willner, “A multi-wavelength optical source based on supercontinuum generation using phase and intensity



## BIBLIOGRAPHY

---

- modulation at the line-spacing rate,” European Conference on Optical Communications(ECOC), Paper Th3.2.4, pp.1-2, Rimini, Italy, September 2003.
- [115] H. J. Song, N. Shimizu, T. Furuta, K. Suizu, H. Ito, and T. Nagatsuma, “Broadband-frequency-tunable sub-terahertz wave generation using an optical comb, AWGs, optical switches, and a uni-traveling carrier photodiode for spectroscopic applications, *Journal of Lightwave Technology*, vol. 26, pp. 2521-2530, 2008.
- [116] I. Tomita, H. Sanjoh, E. Yamada, and Y. Yoshikuni, “Novel method for generating multiple wavelengths by pulsed serrodyne modulation,” *IEEE Photonics Technology Letters*, vol. 15, pp. 1204-1206, 2003.
- [117] A. Lowery, “Performance predictions and topology improvements for optical serrodyne comb generators,” *Journal of Lightwave Technology*, vol. 23, pp. 2371-2379, 2005.
- [118] F. Curti, B. Daino, G. d Marchis, and F. Matera, “Statistical treatment of the evolution of the principal states of polarization in single-mode fibers,” *Journal of Lightwave Technology*, vol. 8, pp. 1162-1166, 1990.
- [119] M. Karlsson, J. Brentel, and P. A. Andrekson, “Long-term measurement of PMD and polarization drift in installed fibers,” *Journal of Lightwave Technology*, vol. 18, pp. 941-951, 2000
- [120] G. Ishikawa and H. Ooi, “Polarization-mode dispersion sensitivity and monitoring in 40-Gbit/s OTDM and 10-Gbit/s NRZ transmission experiments,” *Conference on Optical Fiber Communication (OFC)*’98, pp. 117-119, San Diego, CA, Mar 1998.

## BIBLIOGRAPHY

---

- [121] S.M.R.M. Nezam, Yong-Won song, Changyuan Yu, J.E. McGeehan, A.B. Sahin, and A.E. Willner, "First-order PMD monitoring for NRZ data using RF clock regeneration techniques," *Journal of Lightwave Technology*, vol. 22, pp. 1086-1093, 2004.
- [122] C. Yu, Y. Wang, T. Luo, Z. Pan, S.M.R. Motaghian Nezam, A. B. Sahin, and A. E. Willner, "Chromatic-Dispersion-Insensitive PMD Monitoring for NRZ Data Based on Clock Power Measurement Using a Narrowband FBG Notch Filter," European Conference on Optical Communications Proceedings (ECOC), Paper Tu4.2.3, pp.1-2, Rimini, Italy, September 2003.
- [123] F. Roy, C. Francia, F. Bruyere, and D. Penninckx, "A simple dynamic polarization mode dispersion compensator," *Conference on Optical Fiber Communication (OFC)'99*, pp. 275-278, San Diego, CA, Mar 1999.
- [124] N. Kikuchi, "Analysis of signal degree of polarization degradation used as control signal for optical polarization mode dispersion compensation," *Journal of Lightwave Technology*, vol. 19, pp. 480-486, 2001.
- [125] B. W. Hakki, "Polarization mode dispersion compensation by phase diversity detection," *IEEE Photonics Technology Letters*, vol. 9, pp. 121-123, 1997.
- [126] F. Buchali, W. Baumert, H. Bulow, J. Poirrier, "A 40 Gb/s eye monitor and its application to adaptive PMD compensation," *Conference on Optical Fiber Communication (OFC)'02*, pp. 202-203, Anaheim, CA, Mar 2002.
- [127] T. E. Dimmick, G. Rossi and D. J. Blumenthal, "Optical dispersion monitoring technique using double sideband subcarriers," *IEEE Photonics Technology Letters*, vol. 12, 900-902, 2000.

## BIBLIOGRAPHY

---

- [128] M. N. Petersen, Z. Pan, S. Lee, S. A. Havstad and A. E. Willner, "Online chromatic dispersion monitoring and compensation using a single inband subcarrier tone," *IEEE Photonics Technology Letters*, vol. 14, 570-572, 2002.
- [129] Z. Pan, Q. Yu, Y. Xie, S. A. Havstad, A. E. Willner, D. S. Starodubov, and J. Feinberg, "Chromatic dispersion monitoring and automated compensation for NRZ and RZ data using clock regeneration and fading without adding signaling," *Conference on Optical Fiber Communication (OFC)'01*, WH5-1, Anaheim, CA, Mar 2001.
- [130] K.-T. Tsai and W. I. Way, "Chromatic-dispersion monitoring using an optical delay-and-add filter," *Journal of Lightwave Technology*, vol. 23, 3737-47, 2005.
- [131] Y. K. Lize, L. Christen, J. -Y. Yang, P. Saghari, S. Nuccio, A. E. Willner, and R. Kashyap, "Independent and simultaneous monitoring of chromatic and polarization-mode dispersion in OOK and DPSK transmission," *IEEE Photonics Technology Letters*, vol. 19, 3-5, 2007.
- [132] N. Liu, W. D. Zhong, Y. J. Wen, C. Lu, L. Cheng, and Y. Wang, "PMD and chirp effects suppression in RF tone-based chromatic dispersion monitoring," *IEEE Photonics Technology Letters*, vol. 18, 673-675, 2006.
- [133] R. A. Skoog, T. C. Banwell, J. W. Gannett, S. F. Habiby, M. Pang, M. E. Rauch, and P. Toliver, "Automatic identification of impairments using support vector machine pattern classification on eye diagrams," *IEEE Photonics Technology Letters*, vol. 18, 2398-2400, 2006.
- [134] N. Hanik, A. Gladisch, C. Caspar, and B. strebel, "Application of amplitude histograms to monitor performance of optical channels," *Electronics Letters*, vol. 35, pp. 403-404, 1999.

## BIBLIOGRAPHY

---

- [135] N. Kikuchi, S. Hayase, K. Sekine, and S. Sasaki, "Performance of chromatic dispersion monitoring using statistical moments of asynchronously sampled waveform histograms," *IEEE Photonics Technology Letters*, vol. 17, 1103-1105, 2005.
- [136] Z. Li and G. Li, "In-line performance monitoring for RZ-DPSK signals using asynchronous amplitude histogram evaluation," *IEEE Photonics Technology Letters*, vol. 18, 472-474, 2006.
- [137] S. D. Dods and T. B. Anderson, "Optical performance monitoring technique using delay tap asynchronous waveform sampling," *Conference on Optical Fiber Communication (OFC)'06*, OThP5, Anaheim, CA, 2006.
- [138] T. B. Anderson, A. Kowalczyk, K. Clarke, S. D. Dods, D. Hewitt, and J. C. Li, "Multi impairment monitoring for optical networks," *Journal of Lightwave Technology*, vol. 27, 3729-3736, 2009.
- [139] J. Zhao, Z. Li, D. Liu, L. Cheng, C. Lu, and H. Y. Tam, "NRZ-DPSK and RZ-DPSK signals signed chromatic dispersion monitoring using asynchronous delay-tap sampling," *Journal of Lightwave Technology*, vol. 27, 5295-5301, 2009.
- [140] Z. Li, J. Zhao, L. Cheng, Y. Yang, C. Lu, A. P. T. Lau, C. Yu, H. Y. Tam and P. K. A. Wai, "Signed chromatic dispersion monitoring of 100Gbit/s CS-RZ DQPSK signal by evaluating the asymmetry ratio of delay tap sampling," *Optics Express*, vol. 18, 3149-3157, 2010.
- [141] S. Diaz, S. Foaleng Mafang, M. Lopez-Amo, L. Thevenaz, "High performance Brillouin distributed fiber sensor," *Third European workshop on Optical fibre sensors*, SPIE vol. 6619, pp. 661938-1-4, 2007.

# List of Publications

1. Jing Yang and Changyuan Yu, “Optical Frequency Comb Generation Utilizing a Single Phase Modulator in an amplified Loop,” submitted to Photonics Technology Letter.
2. Jing Yang, Changyuan Yu, Yanfu Yang, Linghao Cheng, Zhaohui Li, Chao Lu, Alan Pak Tao Lau, Hwa-yaw Tam, and P. K. A. Wai, “PMD Insensitive CD Monitoring in High-speed Transmission System Based on RF Power Measurement,” submitted to Photonics Technology Letter.
3. Jing Yang, Changyuan Yu, Linghao Cheng, Zhaohui Li, Chao Lu, Alan Pak Tao Lau, Hwa-yaw Tam, and P. K. A. Wai, “CD Insensitive PMD Monitoring with Large Measurement Range in 57-Gbit/s D8PSK and 38-Gbit/s DQPSK Systems,” *Optics Express*, vol. 19, Iss 2, pp. 1354-1359, 2011
4. Jing Yang, Junhao Hu, Changyuan Yu, Yong Kee Yeo, and Yixin Wang, “Multi-Channel 80-GHz RZ Pulse Train Generation Based on Parametric Process in Highly Nonlinear Fiber,” *Optics Communications*, vol. 283, pp. 939-945, March 15, 2010.
5. Jing Yang, Changyuan Yu, Zhihao Chen, Junhong Ng, and Xiufeng Yang, “Suppression of Polarization Induced Signal Fluctuation in Optic Distributed Sensing System Based on SBS,” *Electronics Letters*, vol. 45, pp. 154-156, January 2009.

## BIBLIOGRAPHY

---

6. Changyuan Yu and Jing Yang, "CD and PMD Monitoring Based on RF Spectrum Analysis with Optical Filtering," Asia Communications and Photonics Conference and Exhibition (ACP) 2010, Shanghai, China, December 2010 (Invited).
7. Changyuan Yu, Jing Yang, and Junhao Hu, "Nonlinear Fiber Based Processing for High Speed Optical Communication and Sensor Systems," Summer Topicals 2010, Playa del Carmen, Riviera Maya, Mexico, July 2010 (Invited).
8. Jing Yang, Changyuan Yu, Linghao Cheng, Zhaohui Li, and Chao Lu, "PMD Insensitive CD Monitoring Based on RF Power Ratio in D8PSK and DQPSK Systems," 9th International Conference on Optical Internet (COIN)'10, Paper TuC3-3, The Shilla Jeju, Korea, July 2010.
9. Jing Yang, Changyuan Yu, Linghao Cheng, Zhaohui Li, Chao Lu, Alan Pak Tao Lau, Hwa-yaw Tam, and P. K. A. Wai, "CD insensitive PMD monitoring by using FBG notch filter in 57-Gbit/s D8PSK and 38-Gbit/s DQPSK systems," Conference on Lasers and Electro-Optics (CLEO) '10, Paper CFC1, San Jose, CA, USA, May 2010.
10. Jing Yang and Changyuan Yu, "Broadband Multi-Wavelength Light Source Generation Using a Single Phase Modulator in a Loop," Conference on Lasers and Electro-Optics (CLEO)'10, Paper JThE56, San Jose, CA, USA, May 2010.
11. Jing Yang, Kang Wei Leroy Chee, and Changyuan Yu, "CD Insensitive PMD Monitoring for Different Modulation Formats Based on RF Tone Power Measurement Using an FBG Notch Filter," 7th International Conference on Information, Communications and Signal Processing (ICICS)'09, Paper P0727, pp. 1-5, Macau, December 2009.

## BIBLIOGRAPHY

---

12. Jing Yang, Junhao Hu, Changyuan Yu, Yong Kee Yeo, and Yixin Wang, "Multi-channel 80-GHz RZ Pulse Train Generation Based on Four-Wave Mixing in a Highly Nonlinear Fiber," OptoElectronics and Communications Conference (OECC) '09, Paper TuA5, pp. 1-2, Hong Kong, July 2009.
13. Jing Yang, Changyuan Yu, Zhihao Chen, Junhong Ng, and Xiufeng Yang, "Polarization Insensitivity Optical Distributed Sensing System Based on Stimulated Brillouin Scattering," 5th International Conference on Materials for Advanced Technologies (ICMAT)'09, P-S10.12, pp. 1-3, Singapore, July 2009.
14. Jing Yang, Junhao Hu, Changyuan Yu, Yong Kee Yeo, and Yixin Wang, "Multi-channel 80-GHz RZ Pulse Train Generation Based on XPM and FWM in a Nonlinear Optical Loop Mirror," 5th International Conference on Materials for Advanced Technologies (ICMAT)'09, Paper P-S5.03, pp. 1-3, Singapore, July 2009.
15. Jing Yang, Changyuan Yu, Zhihao Chen, Junhong Ng, and Xiufeng Yang, "Suppression of Polarization Sensitivity in BOTDA Fiber Distributed Sensing System," International Conference on Optical Fibre Sensors (OFS)'08, Proceedings of SPIE, vol. 7004, Paper 700421, pp. 1-4, Perth, Australia, April 2008.
16. Changyuan Yu, Jing Yang, Zhaohui Li, and Yixin Wang, "Multi-Channel 160-GHz Pulse Generator Using a 40-GHz Phase Modulator and Two Stages of PM Fiber," 6th International Conference on Information, Communications and Signal Processing (ICICS)'07, Paper P0848, pp. 1-4, Singapore, December 2007.
17. Changyuan Yu, Zhaohui Li, Jing Yang, and Yixin Wang, "Multi-Channel High-Speed Optical Pulse Train Generation Based on Phase Modulation at Half Frequency," Conference on Lasers and Electro-Optics (CLEO)'07, Paper CMJJ7,

## **BIBLIOGRAPHY**

---

pp. 1-2, Baltimore, MD, USA, May 2007.